Aalto University
School of Chemical
Technology

Rana Anwar Ul Haq

Thermodynamics and Precipitation Kinetics of Lithium Carbonate (Li_2CO_3)

Master´s Programme in Chemical, Biochemical and Materials Engineering

Major in Chemical and Process Engineering

Master's thesis for the degree of Master of Science in Technology submitted for inspection, Espoo, 27 July, 2019.

Supervisor	Professor Marjatta Louhi-Kultanen
Instructor	Bing Han

Aalto University
School of Chemical
Engineering

Aalto University, P.O. BOX 1000,00076
AALTO
www.aalto.fi

Abstract of master's thesis

Author Rana Anwar ul Haq

Title of thesis Thermodynamics and Precipitation Kinetics of Lithium Carbonate

Degree Programme Masters programme in Chemical, Biochemical and materials Engineering

Major Chemical and Process Engineering

Thesis supervisor Professor Marjatta Louhi-Kultanen

Thesis advisor(s) / Thesis examiner(s) Bing Han

Date 29.08.2019 **Number of pages** 115 **Language** English

Abstract

The objective of this thesis was to study thermodynamics and precipitation kinetics of lithium carbonate in liquid-liquid and gas-liquid system in a jacketed stirred tank reactor and study the influence of impeller speed, pump flow rate, residence time and ageing for precipitation of lithium carbonate in homogeneous system and gas flow rate, impeller speed, temperature, residence time and ageing for precipitation of lithium carbonate in heterogeneous system as operation variables. Filterability was studied to investigate efficient solid-liquid separation. The result obtained from homogeneous and heterogeneous reactive crystallization were investigated and compared.

Solubility study of Li_2CO_3 in Li_2CO_3-Li_2SO_4-H_2O ternary system modeled with Pitzer thermodynamic model indicated the effects of other electrolytes on the Li_2CO_3 solubility behavior. Mixing conditions such as flow patterns and internal stirring speed were theoretically studied to have efficient mixing and avoid flooding of gas.

The crystals produced from crystallization in heterogeneous system and homogeneous system were characterized with scanning electron microscope (SEM), energy dispersion x-ray spectroscopy (EDS), and X-ray diffraction, particle size distribution. The crystals are mainly Li_2CO_3 that was identified by using HighScore software. Particles have flower-shape pellets and the size is in the range of 50-100 µm.

Overall, the study clearly shows that crystallization using CO_2 gas in gas-liquid system and using Na_2CO_3 in liquid-liquid system can be used as a feasible way to recover lithium carbonate from lithium sulfate solution. It was noted that the high pH was necessary for the absorption of CO_2 gas and to get the maximum crystals in heterogeneous reactive crystallization. In addition, the pH was dependent to the temperature which results difficulty in controlling the pH of the solution, product yield percentage, purity and uniform crystal shape. To predict the precipitation kinetics of Li_2CO_3, homogeneous reactive crystallization was easier because no pH adjustment required, rapid precipitation and more crystals obtained in less time as compared to the heterogeneous reactive crystallization.

Keywords Precipitation kinetics, reactive crystallization, dissolution, Pitzer model, lithium carbonate precipitation, mixing, stirred tank

ACKNOWLEDGEMENTS

The experimental part of this thesis was carried out at of School of Chemical Enginering at Aalto University from the beginning of October 2018 until the end of April 2019.

I would like to thank Professor Marjatta Louhi-Kultanen for her help, advice, and for providing me this opportunity to make this interesting topic as my thesis.
In addition to this, I would also like to thank my advisor Bing Han, for helpful guidance and helping me troubleshooting during the experiments.

Finally, I would like to express my deepest gratidute towards my parents Rana Ajaz Ul Haq and Anjum Ajaz and my brothers Imtiaz and Inzimam for endless support which they have given me throughout these years.

July 2019, Espoo
Rana Anwar Ul Haq

Table of Contents

List of symbols

A	Filtration area	m^2
dp	Diameter of particle	m
p	Pressure	bar
n	Compressibility index	-
Δp	Pressure difference	-
q	Superficial velocity of filtrate	m^3/s
Q	Flow rate of filtrate	L/min
V	Volume of filtrate	L
α	Specific cake resistance	m/s
ε	Porosity	-
μ	Dynamic viscosity of liquid	pa. s
I	Ionic strength	mol/m^3
Re	Reynolds number	-
N	Stirrer speed	revolutions per minute
D	Impeller diameter	m
ρ	Density	kg/m^3
F_{gs}	Volumetric gas flow rate	m^3/s
g	Gravitational acceleration	9.8 m/s^2
D_{A2}	Diameter of agitator of scale up vessel	m
D_{A1}	Diameter of agitator of scale up vessel	m

1. Introduction

1.1 Background

Lithium is available in the brines and lithium ores, which are the main sources of the production of lithium. Commercially and industrially, the most important lithium ores are lepidolite, spodumene, petalite and amblygonite. The price of lithium is constantly increasing due to increasing in demand of lithium-ion batteries, ceramics and special glass production, manufacturing of aluminum temperature tolerant lubricant greases, air conditioning and catalyst in manufacturing of rubber, nuclear industry, pharmaceutical industry, synthesis of vitamins, formation of organic compounds and silver solders and underwater buoyancy devices (Mohr et al., 2012). Lithium-ion batteries (LIB) is seen as the most efficient electro-chemical energy storage technology (Bi et al., 2016;Swain, 2017).

Lithium carbonate is seen as one of the most important lithium chemical compound representing about 39% of total lithium demand. The main application of lithium carbonate are batteries (60%) and ceramics and glass (27%) in merchant market 2017. Lithium carbonate is forecast to increase significantly and it is estimated that demand of lithium for industry related to batteries will reach 12,000 tons by 2020 and 22,000 tons by 2025 (Swain, 2017).

The main driver for the growth is the increasing use of lithium in larger batteries about 290,000 tons are expected to be demand for batteries in 2035 (Conservative Scenario). CORFO estimated that the world market for lithium batteries by 2022 is expected to continue its accelerated growth to double the actual market, reaching USD 40~46 Billion (CORFO, 2017). The Figure 1 and Figure 2 Market research Lithium 101 by Deutsche bank published in 2016 shows the global growth forecast of the lithium demand by applications and Figure 3 shows the lithium demand by end applications (2015-25). The lithium batteries production have raised globally to 30% of the overall production in 2025 (Deutsche Bank, 2016). Production of lithium between 127 and 405 kt lithium per year will be required in the year 2050 (Mohr et al., 2012).

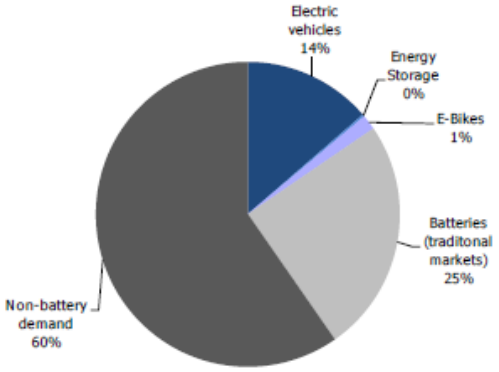

Figure 1: 2015 Lithium demand by applications (Deutsche Bank, 2016)

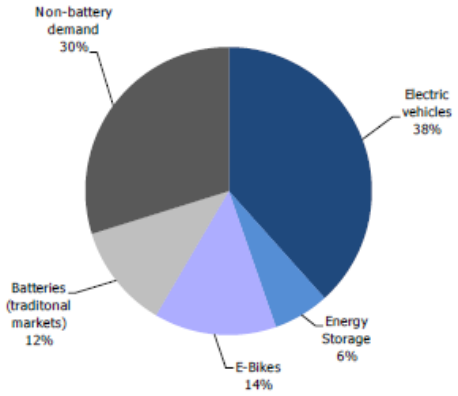

Figure 2: 2025 Lithium demand by applications (Deutsche Bank, 2016)

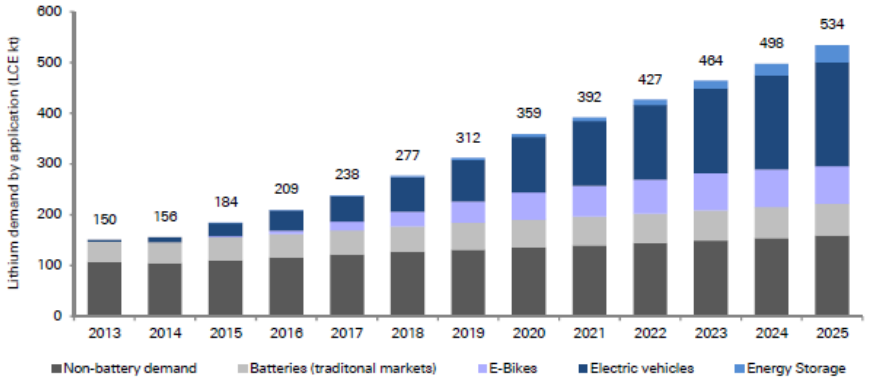

Figure 3: Lithium demand by end applications (2015-25) (Deutsche Bank, 2016)

The largest manufacturers of battery are the Asian companies. Europe and Finland seeks this as a business opportunity to become world leaders in circular economy in batteries and aims to accelerate to acquire a lead in Battery technology in Europe so that they can reduce the imports of lithium and lithium products. The Keliber oy, which is a mining company, is going to start mining operations and lithium chemicals production during the year 2021. In addition to lithium mining, Keliber is also developing a chemical plant in Kokkola. The objective is to produce 11,000 tons of high-quality lithium carbonate per year driven by the fast growing market for lithium battery worldwide (Poe, 2018).

Batteries from Finland activation two-year program started by Business Finland to establish battery market in Finland. Market of lithium carbonate internationally has been quite changing aggressively during the last few years. According to Banco Bilbao Vizcaya Argentaria's (BBVA) research, the price of lithium rose significantly since 2016. The rise in production of electric vehicles resulted in the increased demand of lithium worldwide from 20% in 2014 to 49% in 2018 and it is stated that the lithium share of demand could achieve 90% by 2030 (Casillas and Marcial, 2018).

To meet lithium demand in future it is essential to raise the recycle the lithium-ion batteries from approximately 3 percent to 95 percent (Sonoc et al., 2015). Recycling of the battery waste provides the advantage of abiding the regulations concerning the waste such as imposing restrictions in the hazardous sub- stances usage in the EEE (RoHS) directive and waste electrical and electronic equipment (WEEE) directive. Through recycling, importance was given to United Nations Environment Program e-waste management program, strategy related to extend producer responsibility (EPR) waste management and helped to follow e-waste crime. Lithium ion battery should be 100 percent recycled with at least 90 percent recovery of lithium to prevent the upcoming supply crises (Sonoc et al., 2015). To meet lithium need, it is important to search the alternative methods to meet the lithium demand in an efficient way (Swain, 2017).

1.2 Objective and scope of the work

This research aims to study and compare the thermodynamics and lithium carbonate precipitation kinetics on the gas-liquid heterogeneous reactive crystallization using Li_2SO_4 and CO_2, and in liquid-liquid homogeneous reactive crystallization by using Li_2SO_4 and Na_2CO_3. In both cases major phenomenon is investigated during the process. Key factors affecting the precipitation of lithium carbonate and kinetics studies regarding nucleation and crystal growth were investigated.

The goal is to study the influence of impeller speed, pump flow rate, residence time and ageing for precipitation of lithium carbonate in homogeneous system and gas flow rate, impeller speed, temperature, residence time and ageing for precipitation of lithium carbonate in heterogeneous system to find the optimal condition to develop and manufacture crystals having desired attributes such as uniform crystal to provide the knowledge for process optimization and scale up in an industrial level.

The studies concerning mixing in crystallizer to select optimum impeller speed for turbulent flow and gas flow rates to have efficient mixing and avoid flooding of gas were investigated. Cake filtration at constant pressure is one of the most important techniques for separation of a solid and a liquid phase from a slurry is considered in this study.

The influence of Li_2SO_4 concentration in the solution of ternary system Li_2SO_4-Li_2CO_3-H_2O on the solubility of Li_2CO_3 was studied with Pitzer model.

The produced samples were examined with Scanning Electron Microscope (SEM) and X-ray diffraction (XRD). Crystallization mechanisms such as nucleation and growth can be observed under ParticleTrack with Focused Beam Reflectance Measurement (FBRM) technology. Particle size distribution (PSD) was analyzed with the Malvern masterizer 2000.

The results obtained from the gas-liquid heterogeneous reactive crystallization and liquid-liquid homogeneous reactive crystallization were compared. Filterability, compressibility, particle shape, particle size distribution, product yield, nucleation, crystal growth, influence of process parameters and ageing were included.

Literature part

2 Industrial and battery grade lithium carbonate

Lithium can be found as third element on the periodic table and lithium is the first element in group of alkali metals. Lithium has the ability to be the most polarized element in the alkali metals and have the potential to possess chemical energy more efficiently due to the fact that it has very high electronegativity. Lithium in the form of lithium carbonate have many applications, such as in medications for the treatment of patients, manufacturing of metal alloys, glasses, ceramics, enamel, fritted grazes and refractories. Lithium is used to manufacture lithium grease for waterproofing purpose and potential to attain high viscosity, low melting point, attains mechanically high strength and potential of having high thermal resistance. Lithium is also used medically to treat hypertension, epilepsy, headaches and even in treatment of teethes (Kavanagh et al., 2018).

The battery grade lithium carbonate requires sodium less than $6x10^{-4}$ % because this metal has ability to react and oxidize with oxygen resulting in potential to ignite. The quantity of magnesium in battery grade lithium carbonate should be also less than $5x10^{-3}$ % because this metal makes a layer on the electrolyte during electro-winning of lithium results in shot circuiting of the cells (Swain, 2017).

3. Precipitation of lithium carbonate

Kelkar and Ng (1999) briefly describe that reactive crystallization, or precipitation is a process which precipitate solids as a result of reaction between the reactants. Precipitation is a process involving same time reaction, mass transfer, nucleation and growth, including aging, ripening, agglomeration and breakage as a secondary processes (Kelkar and Ng, 1999).

Pyrometallurgy and hydrometallurgy are the main processes which are engaged in precipitation of lithium from sources categorize as secondary and primary (Swain, 2017), (**Ordoñez et al., 2016), (Meshram et al., 2014)**. Precipitation of Li_2CO_3 from hydrometallurgical process is considered more feasible as compared to pyrometallurgy that needs big investment and causes pollution because of Advantages of this technology include of having ability to produce in small scale,

reducing hazardous emissions of gases, and having efficient energy usage and waste disposal (An et al., 2012), (Nguyen et al., 2018). According to Nguyen et al, (2018), disadvantage of precipitation are involving impurities present in the precipitates, the simultaneous precipitation of more than one compound from a solution and slow reaction kinetics.

3.1 Precipitation of lithium carbonate by heterogeneous reactive crystallization

The demand of Li_2CO_3 is increasing due to the use in batteries, pharmaceutical, atomic industry and information industry for microelectronic devices. Therefore there is a need to make efforts on manufacture lithium carbonate with highest purity. Precipitation of carbonate is one of the important proceses in synthesis of lithium carbonate. However, the study of thermodynamics and precipitation kinetics of CO_2-Li_2SO_4 reactive crystallization has not been studied yet. A typical gas-liquid reactive crystallization mechanism where the reactants, products, or both are in more than one phase is most suitable in the stirred tank reactor. In addition, it is difficult to maintain the quality of the precipitates because the crystal size and shape is not always the same after each batch during manufacturing (Sun et al., 2012).

Carbon dioxide is one of the gases that is contributing in the global warming (Gangopadhyay et al., 2008; Zhao et al., 2006). To overcome the climate changes the efforts in CO_2 reduction are made by many countries (Yoo et al., 2013). According to Yoo *et al.*, (2013), the potential method of capturing CO_2 is chemical absorption of CO_2 in a NaOH aqueous solution in a heterogeneous gas-liquid reaction.

One of the advantages of using CO_2 is economical and properties like low toxicity, easily recyclable and nonflammable, which makes it feasible in crystallization of Li_2CO_3 (Wang and Chiu, 2009). According to Jandova et al., (2012), one of the application is precipitation of Li_2CO_3 by CO_2 from waste water. Firstly, the solution is concentrated to achieve lithium concentration of 12-13 g Li/L by solvent. The condensation process allows recovery of some volatile organic compounds. Then, CO_2 in gaseous phase is fed at 40^oC resulting $LiHCO_3$ then the Li_2CO_3 is precipitated after solution temperature is elevated to 95^oC, as shown in Figure 4.

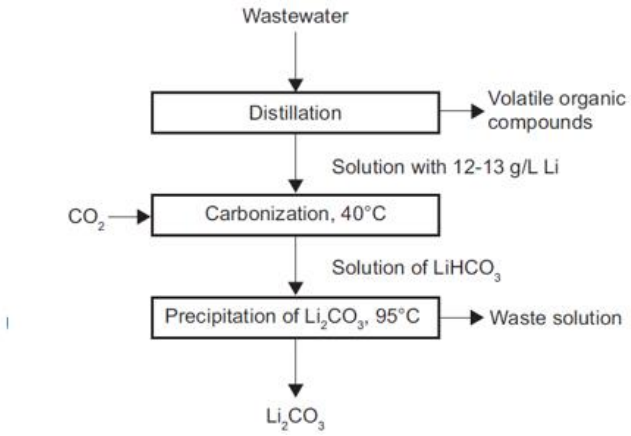

Figure 4. Li_2CO_3 precipitation process from waste water (Jandova et al., 2012).

Yoo et al., (2013) have explained the absorption process of CO_2 in NaOH aqueous solution in detail where CO_2 is physically absorbed in the NaOH aqueous solution The physical absorption is listed in the Eq. 1 (Yoo et al., 2013).

$$CO_2(g) \rightarrow CO_2(aq) \qquad \text{Eq. 1}$$

Subsequently, aqueous CO_2 reacts with OH^- to produce HCO_3^- and CO_3^{2-}, as shown in Eqs. (2) and (3).

$$CO_2(aq) + OH^- \rightleftarrows HCO_3^-(aq) \qquad \text{Eq. 2}$$

$$HCO_3^-(aq) + OH^-(aq) \rightleftarrows H_2O(l) + CO_3^{2-}(aq) \qquad \text{Eq. 3}$$

While CO_2 concentration is same during whole system it is considered to be as a pseudo first-order reaction. The reactions in Eq. 2 and Eq. 3 are reversible and fast at elevated pH. H_2O and CO_3^{2-} is produced as shown in Eq. 3 instantly after the reaction in Eq. 2. After the gaseous CO_2 is converted into aqueous CO_2 as seen in Eq. 2 and Eq. 3. High alkanity results in Eq. 3 to dominate which increases the CO_3^{2-} concentration whereas HCO_3^- concentration decreases. The pH constantly decreases during the reaction and concentration of CO_3^{2-} increases. Considering the above mentioned absorption of CO_2 mechanism, the net reaction is expressed in Eq. 4 (Yoo et al., 2013).

$$2NaOH(aq) + CO_2(g) \rightarrow Na_2CO_3(aq) + H_2O(l) \qquad \text{Eq. 4}$$

According to Xu et al., (2014), industrial grade lithium carbonate was produced by reacting lithium sulfate with sodium carbonate shown in Eq. 5.

$$Li_2SO_4 + Na_2CO_3 \rightarrow Li_2CO_3 + Na_2CO_3 \quad \text{Eq. 5}$$

According to Yoo et al., (2013), Eq. 6 represents the overall reaction in CO_2 absorption if the NaOH is limiting reactant, which represents the net reaction of Eq. 2 and Eq. 3.

$$NaOH(aq) + CO_2(g) \rightarrow NaHCO_3(aq) \quad \text{Eq. 6}$$

According to Jandova et al., (2012), lithium carbonate solubility is lower in water at lower temperature and it produces lithium bicarbonate in the presence of aqueous CO_2 as shown in Eq. 7. According to Martin *et al.*, (2017), the $LiHCO_3/Li_2CO_3$ equilibrium in the Eq. 7 shifts to Li_2CO_3 when the temperature is increased above 50°C. Solubility of lithium carbonate in water is much lower than the solubility of lithium bicarbonate as compared to bicarbonate of lithium. According to Jandova et al., (2012), heating the solution above 50°C results in convert of $LiHCO_3$ to less soluble Li_2CO_3.

$$H_2O + CO_2 + Li_2CO_3 \rightleftarrows 2\mathrm{LiH}CO_3 \quad \text{Eq. 7}$$

According to Xu et al., (2014), solubility of lithium carbonate decreases as the temperature increases and solubility of lithium sulfate slightly decreases as the temperature increases, which are shown in Figure 5 with the solubility curves of different lithium salts.

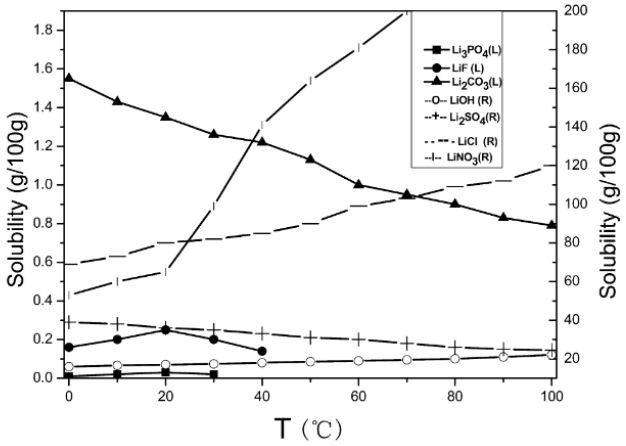

Figure 5. Solubility curves of different lithium salts with change of temperature (Xu *et al.*, 2014) R=Secondary Y-axis and L=primary Y-axis.

3.1.1 Concentration at different pH

According to Sun et al., (2012), the point at which the carbonation process is stopped is important to obtain the highest yield. Figure 6 shows that the most suitable end pH to have the highest yield is 9-9.5 as it can be seen from Figure 6 that the concentration of [Li^+] and [OH^-] falls at constant pH 12, later when the pH decreases the concentration of [Li+] decreases and then increases. The optimum pH to obtain the maximum yield is between 9 and 9.5 (Sun *et al*., 2012).

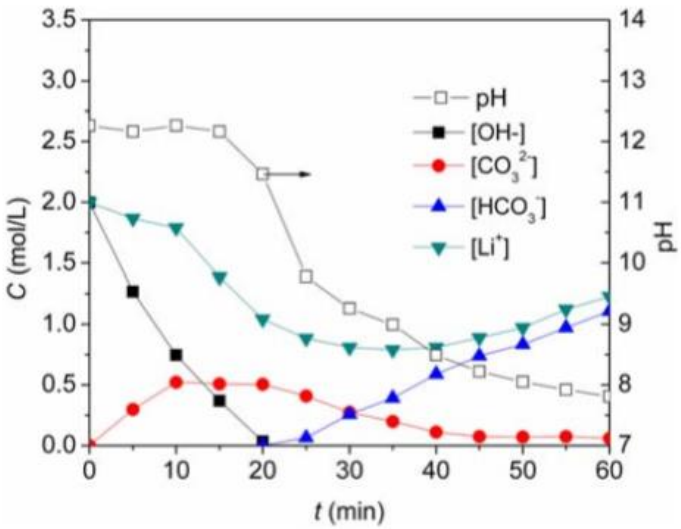

Figure 6. Concentration of ions present as the pH changes in the carbonation process (Sun *et al*., 2012).

3.1.2 Effects of operational variables

Sun et al, (2012) investigated the influence of operation variables on nucleation rate, crystal growth rate and crystal breakage with the aim to obtain high crystal yield and uniform crystal quality. According to Sun et al., (2012), temperature is one of the most important aspect in the heterogeneous reactive crystallization. The reason for the rise in absorption is that the reaction rate increases as the temperature of the solution is increased. In addition, increase in temperature reduces the viscosity, which results in reduction in mass transfer limitations and increase in mass transfer coefficient.

According to Sun et al., (2012), concentration of lithium in the solution controls the product yield since the rise of lithium concentration increases the reaction rate. The concentration of lithium should be above 2.0 mol/L to obtain the maximum Li_2CO_3 precipitates.

According to Sun et al., (2012), increase of CO_2 gas flow rate causes decrease in precipitates yield. Increase in CO_2 feed rate accelerates CO_2 absorption in the interface and accelerates of CO_3^{2-} ions in gas-liquid interface phase.

3.2 Precipitation of lithium carbonate by homogeneous reactive crystallization

According to Han *et al.,* (2018), a lithium carbonate was precipitated in a reactive crystallization in a homogeneous system which was depending on different conditions. The parameters affecting the precipitation of lithium carbonate are pH, lithium carbonate concentrations, temperature, impurities and residence time. According to Mikami *et al.,* (2014), temperature 60 to 75^{o}C, residence time of 90 min, agitation speed of 300rpm and 1.0 mol/L of Na_2CO_3 aqueous solution are used to precipitate lithium carbonate. The crystal size and crystal size distribution were varied with the concentration of impurities in the solution. The increase of temperature resulted in higher yield of lithium carbonate (Mikami *et al.,* 2014).

According to Xu *et al.*, (2014), industrial grade lithium carbonate was produced by reacting lithium sulfate with sodium carbonate, shown in Eq. 8.

$$Li_2SO_4 + Na_2CO_3 = Li_2CO_3 + Na_2CO_3 \qquad \text{Eq. 8}$$

According to Zhang et al., (1998), the lithium carbonate solubility concentration is inversely proportion to the temperature. Therefore the optimum temperature to precipitate the lithium carbonate is 100^{o}C.

The increase in agitation had a negative effect on the rate of nucleation since agitation increased the rate of molecules movement, which rose the collision between the molecules (McLeod et al., 2016).

According to Han *et al.,* (2018), lithium carbonate was successfully precipitated shown in SEM images in Figure 7 in a batch and semi-batch crystallization with the Na_2CO_3 with different pump rates and agitation rates at 50^{o}C. Particle size distribution was affected by the rotation speed of impeller. Results showed that the particle size decreased when rotation speed of impeller increased. The reason behind this was the reduction in reaction time to crystallize the solids. Particles with smaller size increased due to higher chemical reaction time.

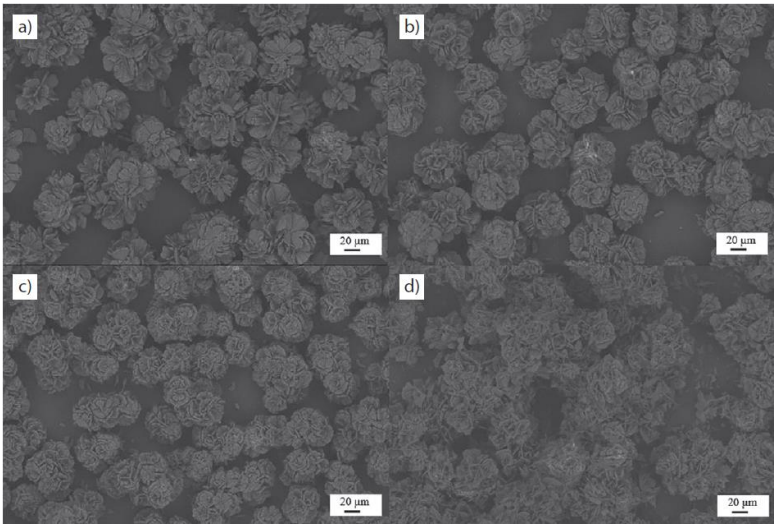

Figure 7. SEM analysis of lithium carbonate precipitates under different residence time (Han et al., 2018).

According to Peng et al., (2019), volume weight mean diameter and specific surface area of lithium carbonate produced was sulfate solution was 0.36 m^2g^{-1} and 63.34 µm, respectively. The particles were larger compared to the lithium carbonate production in nitrate system with mean diameter 24.10 m^2g^{-1} and specific area of 5.10 µm under the same parameters shown in Figure 8.

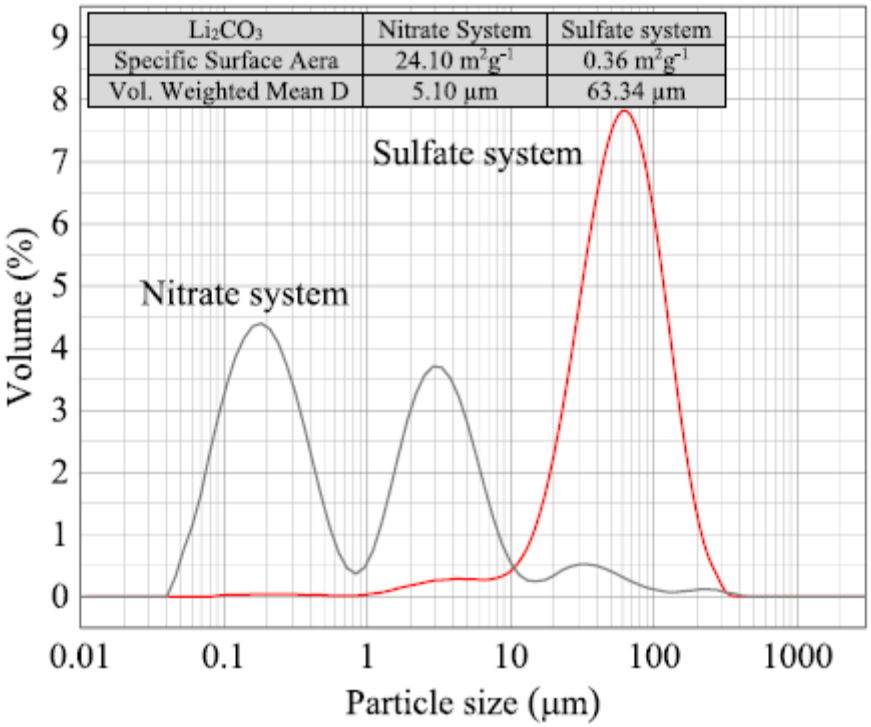

Figure 8. Crystal size distribution of lithium carbonate produced in sulfate system and nitrate system (Peng et al., 2019)

4 Solubility curves of the system being studied

4.1 Introduction

In precipitation and crystallization process, solubility plays an important role in production and purity of the solid products. In crystallization or precipitation it is important to study the compound solubility in the solvent used. To obtain high purity solids, it is necessary to study the solubility of impurities in the solvent. Solubility is known as a tendency of a solute in solid, liquids and gaseous phase to dissolve in solvent solid, liquid or gaseous phase. The properties of the solute and solvent have an effect on the solubility of the solute e.g. pressure, temperature and impurities in solution. The study of solubility model provides the data of solute concentration changes. Crystal properties were predicted with the solubility model (Widenski et al., 2010).

4.4.1 Pitzer thermodynamics modelling (Li_2CO_3-Li_2SO_4-H_2O)

Pitzer model is considered one of the thermodynamics models to predict the electrolyte behavior in aqueous electrolyte solutions, especially at high ionic strengths. Pitzer model is the model which helps to predict the ions behavior dissolved in water. Chemist Kenneth Pitzer was the first person who introduced the model and defined the interactions between the solvent and the ions through linear combined parameters having a viral expansion of the Gibbs free energy. In addition, to predicting the behavior of the ions, Pitzer model can be used for several electrolytes up to 6 mol/kg molarity solutions (Simons el al,. 2016).

4.4.2 Activity coefficient of Li_2CO_3 in binary system

Solubility-product constant is also known as equilibrium constant **Ksp.** Solubility product constant is known to be equilibrium constant in solid ion and solution equilibrium and it indicates the solubility of salts in molar solubility (mol dm^{-3}). At constant temperature solubility product remains same (Mayerser 2002).

$$ln\gamma_{\pm}^{\pm} = |Z_M Z_X| f^{\gamma} + m\left(\frac{2v_M v_X}{v}\right) B_{MX}^{\gamma} + m^2 \left[\frac{2(v_M v_X)^{\frac{3}{2}}}{v}\right] C_{MX}^{\gamma} \qquad \text{Eq. 9}$$

Where Z_m and Z_X represents the charges of the anion X and the cation M. In electrolyte system v_M and v_X are the number of cations and anions. The expressions of f^{Φ} , f^{γ}, B_{MX}^{γ} and B_{MX}^{Φ} are shown in following equations (Eq. 10-14).

$$f^{\Phi} = A^{\Phi} \frac{I^{1/2}}{1 + bI^{1/2}} \qquad \text{Eq. 10}$$

$$f^{\gamma} = -A^{\Phi}\left[\frac{I^{1/2}}{1 + bI^{1/2}} + \frac{2}{b}\ln(1 + bI^{1/2})\right] \qquad \text{Eq. 11}$$

$$B_{MX}^{\Phi} = \beta_{MX}^{(0)} + \beta_{MX}^{(1)} \exp\left(-\alpha_1 I^{1/2}\right) + \beta_{MX}^{(2)} \exp(-\alpha_2 I^{1/2}) \qquad \text{Eq. 12}$$

$$B_{MX}^{\gamma} = 2\beta_{MX}^{(0)} + \frac{2\beta_{MX}^{(1)}}{\alpha_1^2 I}\left[1 - \left(1 + \alpha_1 I^2 - \frac{I^2}{2}\right)\exp\left(-\alpha_1 I^{1/2}\right)\right] + \frac{2\beta_{MX}^{(2)}}{\alpha_2^2 I}[1 - (1 + \alpha_2 I^{1/2} - \frac{\alpha_2^2 I}{2})\exp(-\alpha_2 I^{1/2})] \qquad \text{Eq. 13}$$

$$I_m = (\sum_i Z_i^2 m_i)/2 \qquad \text{Eq. 14}$$

Where *I* is known as ionic strength. The function f indicates the contribution of electrostatic forces in accordance with the Debye-Hückel theory. At 25°C, the Debye-Hückel constant A^{ϕ} = 0.392. For all kinds of electrolytes, the coefficient b= 1.2. The B_{MX} function is a set of the second viral coefficients indicating the short range interaction of ions. α_1 = 1.4, α_2 = 12 are the optimum values for 2-2 electrolytes, and α_1 = 2 for other types of electrolytes. The set of parameters $\beta^{(0)}$, $\beta^{(1)}$, $\beta^{(2)}$, C^{ϕ} for lithium carbonate are -0.38934, -2.2737, 0 and -0.162859 respectively (Filippov *et al.,* 1986).

4.4.3 Activity coefficient for ternary system Equations

$$\mathrm{f'(B)} = \sum \mathrm{MX\, m_M m_X \beta^1_{MX} f_3} \qquad \text{Eq. 15}$$

$$\mathrm{f_2} = \frac{1}{2\mathrm{I}}\left[1 - \left(1 + 2\sqrt{\mathrm{I}}\right)\mathrm{e}^{-2\sqrt{\mathrm{I}}}\right] \qquad \text{Eq. 16}$$

$$\mathrm{Z} = \sum_{\mathrm{i}} \mathrm{m_i}|\mathrm{z_i}| \qquad \text{Eq. 17}$$

$$\begin{aligned}\ln\gamma_{\mathrm{x}} = {} & \mathrm{z_x^2 f^{\gamma}} + \sum_{\mathrm{c}} \mathrm{m_c}\,(2\mathrm{B_{cx}} + \mathrm{ZC_{cx}}) \\ & + \sum_{\mathrm{a}} \mathrm{m_a}\left(2\theta_{\mathrm{xa}} + \sum_{\mathrm{c}} \mathrm{m_c}\psi_{\mathrm{cXa}}\right) \\ & + \sum_{\mathrm{c}} \sum_{\mathrm{c<c'}} \mathrm{m_c m_{c'}}\psi_{\mathrm{cc'x}} + |\mathrm{z_X}| \sum_{\mathrm{c}} \sum_{\mathrm{a}} \mathrm{m_c m_a C_{ca}} + \mathrm{z_C^2 f'(B)}\end{aligned} \qquad \text{Eq. 18}$$

$$\begin{aligned}\ln\gamma_{\mathrm{M}} = {} & \mathrm{z_M^2 f^{\gamma}} + \sum_{\mathrm{a}} \mathrm{m_a}\,(2\mathrm{B_{Ma}} + \mathrm{ZC_{Ma}}) \\ & + \sum_{\mathrm{c}} \mathrm{m_c}\left(2\theta_{\mathrm{Mc}} + \sum_{\mathrm{a}} \mathrm{m_a}\psi_{\mathrm{Mca}}\right) \\ & + \sum_{\mathrm{a}} \sum_{\mathrm{a<a'}} \mathrm{m_a m_{a'}}\psi_{\mathrm{Maa'}} + |\mathrm{z_M}| \sum_{\mathrm{c}} \sum_{\mathrm{a}} \mathrm{m_c m_a C_{ca}} + \mathrm{z_M^2 f'(B)}\end{aligned} \qquad \text{Eq. 19}$$

$$\mathrm{B_{MX}} = \beta^0_{\mathrm{MX}} + \beta^1_{\mathrm{MX}} \mathrm{f_2} \qquad \text{Eq. 20}$$

$$f^{\gamma} = -A_{\varphi}\left[\frac{\sqrt{I}}{1+b\sqrt{I}} + \frac{2}{b}\ln(1+b\sqrt{I})\right] \quad \text{Eq. 21}$$

$$f_3 = \frac{1}{2I^2}\left[-1 + (1+2\sqrt{I}+2I)e^{-2\sqrt{I}}\right] \quad \text{Eq. 22}$$

$$\gamma_{MX} = (\gamma_M^{vM} * \gamma_X^{vX})^{\frac{1}{(v_M+v_X)}} \quad \text{Eq. 23}$$

In case of ternary systems with a common anion, MX-NX-H_2O, two more parameters, θ_{MN} and ψ_{MNX}, appear in the Pitzer equations for ϕ and γ.

θ_{MN} ψ_{MNX} , appears in the Pitzer equations for φ and lnγ. The parameter θ_{MN} is a combination of second virial coefficients characterizing the interaction between MN, MM, and NN. The parameter ψ_{MNX} corresponding to the interactions between MNX, MMX and NNX.

5. Crystallization kinetics

Crystallization is a term describing the change of phase that precipitates as the crystalline solids. One of the common type of crystallization is crystallization from solution. First the solute is dissolved in the solvent at required temperature and then at certain parameters (temperature, pressure, concentration, etc.) which causes the solute solubility to reduce and results in the crystals.

Reactive crystallization is a type of crystallization in which chemical reaction and crystallization simultaneously. During crystallization the driving force in the precipitation is due to the formation of super-saturation caused by chemical reaction (Nandi et al., 2014).

The precipitation kinetics is explained in terms of nucleation and crystal growth. The crystal properties (purity, crystal size, etc.) are obtained as a result of relation between nucleation rate and crystal growth rate.

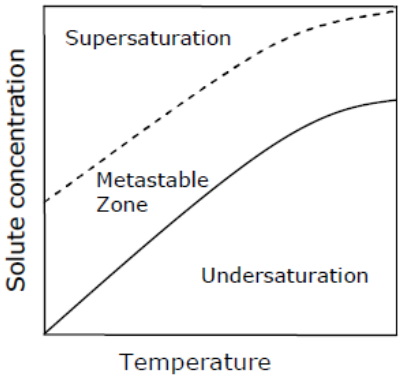

Figure 9. Different regions of solution conditions diagram (Beckmann, 2000). Solid line shows the solubility curve where the solution is saturated.

Saturated, undersaturated and supersaturated solution are three different conditions of a solution shown in Figure 9. The saturated solution respect to solute is at thermodynamic equilibrium. The rates of crystallization and dissolution is equal under the thermodynamic equilibrium.

The term undersatured solution is referred to the solution having solute concentration below the saturation value. Non-equilibrium conditions is required for the crystallization where the solute concentration exceeds the equilibrium concentration.

The region where spontaneous precipitation occurs is the metastable zone bounded by solubility curve and metastable limit. Methods to establish super-saturation in solution are evaporation of solvent, change in temperature, chemical reaction, change in pH, and change in concentration (Beckmann, 2000).

5.1 Crystal nucleation

Nucleation is described as the first process in the crystal formation and an important mechanism of the first order phase transition, transfer from old phase to new phase. Spontaneous nucleation occurs when the upper limit of metastable zone shown in Figure 9. Different regions of solution conditions diagram (Beckmann, 2000). The old phase has the higher free energy than that of new phase formed. (Hohenberg and Halperin 1977; Chaikin and Lubensky 1995). Nucleation is a mechanism in which formation of organized small cluster (embryos) as a newly built phase inside old phase.

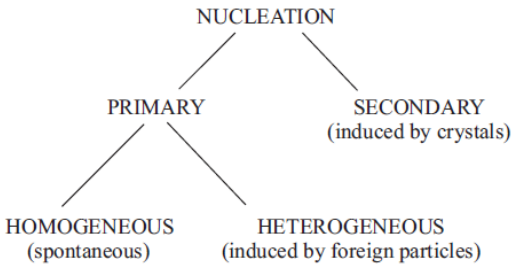

Figure 10. Nucleation mechanisms, according to [Mullin 2001, p. 181]

Crystal nucleation is divided into primary nucleation and secondary nucleation shown in Figure 10. In primary nucleation, solution does not contain any foreign particles. In secondary nucleation solution contains foreign particles mixed in the solution as seeds. The primary nucleation is divided into homogeneous and heterogeneous mechanisms. In homogeneous nucleation the crystallization occurs spontaneously in the solution that do not contain any foreign particles. If the foreign particles are already present or added as seeds in the solution. The nucleation is termed as heterogeneous nucleation. If the crystal is formed in a system that already contains crystals, which is termed as secondary nucleation (Mullin 2001, p. 181-204).

Nucleation has a major influence on crystal characteristics such as size distribution, polymorphic form and particle size (Lui et al., 2015).

5.2 Crystal growth

Crystal growth is the process that causes the growth of the crystal by addition of molecules and atoms and accumulates on the surface of the pre-existing crystal. Crystal growth is termed as discontinuation process and it is explained in absorption layer theories (Mullin 2001, p. 181-204).

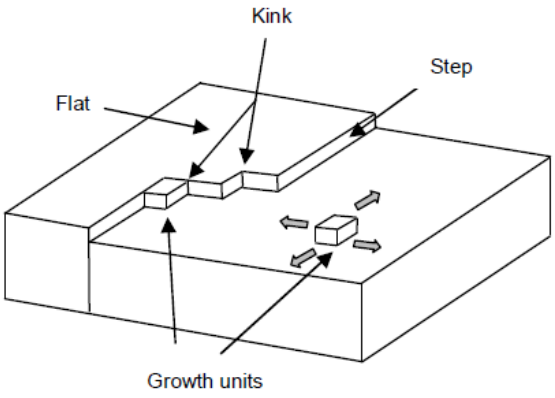

Figure 11. Terraces, kinks and step showing on a crystal surface.

The crystal surface is built up from a flat zone called terrace and constructed by the incomplete layers called steps having kinks shown in Figure 11. The sites of the kinks are important as it allows more bonds with the neighboring molecules as compared to the edges at the flat step and the molecules attached to the terraces (Chernov AA, 1961).

6 Filtration

Filtration is performed after the crystallization process. According to Bourcier et al., (2016), solid-liquid separation has great important in the industries. Solid-liquid separations are required in several industries such as chemistry, biotechnology, pharmaceutical and oil. Solid-liquid separation is mechanism of separating the solids from suspension. One of the most important procedures for solid-liquid separation is the cake filtration. Compressibility and filterability are two most important factors in the solid-liquid separation such as cake filtration.

According to Kobe (1958), pressure-driven filtration shown in Figure 12 is one type of batch filtration which is the best for solid-liquid separation. Pressure-driven filtration is suitable for high solid ratio and the solids are recovered from solid-liquid suspension. In batch filtration where a vacuum pump is attached to create a constant vacuum pressure. Solid particles accumulates on the filter cloth forming a cake. Some of the limitations of filtration are that the process is not efficient for example, few fractions of solids flow with the liquid phase and some of the liquid still remains in the filter cake.

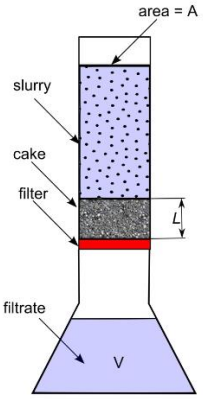

Figure 12. Schematic drawing showing Batch filtration at constant pressure

According to Kobe (1958), selection of the filter is depends on many factors such as material density, viscosity, and how corrosive a material behave. Temperature, concentration, particle size, particle size distribution, crystal shape, pressure drop, filtration surface area, cake resistance and filter medium resistance are important factors that affect filtration rate. These factors depends on the operational conditions applied in the crystallization process. According to the Pöllänen *et al.* (2005), the operational variables in the crystallization have effects on the filtration process.

6.1 Cake resistance

According to Bourcier *et al.* (2016), the cake resistance or permeability determined at constant pressure gives information how easily the fluid can pass through the voids of the cake. Particle size, particle size distribution and shape have an impacts on the cake resistance. Specific cake resistance increases as the particle size reduces. Cake resistance or cake permeability is one of the most important factors in designing filter.

According to Kobe (1958), viscosity of the filtrate and cake resistance have negative effects on the filtration rate.

6.2 Cake porosity

The cake porosity is one factor that affects the cake resistance is known as volume fraction of voids and the structure of packing is the factor affecting the porosity (Shirato et al., 1971).

$$\varepsilon = \frac{Volume\ of\ particulate\ voids}{(Volume\ of\ voids + volume\ of\ solids)} \qquad \text{Eq. 24}$$

6.3 Compressibility

According to Bourcier *et al.* (2016), as the filtering pressure is increased in a compressible cake, it has a negative effect on the cake porosity, and thus results in the increase the resistance of liquid flow passing the cake.

During filtration loosely packed layers are formed. As time passes during the filtration, cake is formed and the layers in the bottom exerts the pressure on the particles. Incompressible cake does not have any effect on the porosity of the cake. The filter cake is considered as compressible if the porosity is affected by the force applied to its particle distribution (Pöllänen et al., 2005).

According to Pöllänen et al., (2005), compressibility is effected by particle shape, particle size distribution, average particle size and surface properties of the particles. Higher filtration pressure cause for compressible filter cakes decrease in cake porosity and increase in cake resistance.

6.4 Effects of factors on the filtration

Particle size is one of the important factors in filtration process and selection of the filtration equipment. The separation becomes difficult as the particle size becomes finer. Particle shape has an influence on the distribution of filter cake and porosity increases as the shape of the particles changes from sphere to cubes, needles and platelets. Particle size distribution strongly affects the porosity. The porosity decreases because the voids can be filled with the small particle, which resulting in the increase in the cake resistance. Properties of the liquid phase such as viscosity is the one of the most important factors affecting the suspension filterability. Viscosity plays an important role in the fluid flow through the cake. Liquids having low viscosity can flow easily through the fluids (Pöllänen et al., 2005)

7 Understanding the mixing in crystallizer.

A careful selection of optimized stirred tank design is necessary to have maximum efficiency of mixing that produces turbulence in the process to obtain quality product and to minimize cost of production. Mixing has an important role in the mass transfer between the phases by increasing interfacial area and preventing settling (Torotwa and Torotwa, 2018). Crystallizers are mostly stirred tank reactors and impeller is placed centrally for better mass and heat transfer in the vessel to prevent the crystals to settle during the process, reduce the formation of scale, and provide uniform crystal shape and size. Baffles are important for properly dispersed flow conditions in a stirred tank which is required to enhance the mixing, mass and heat transfer. Therefore it is necessary to have baffles with specified structure. Baffle also helps to reduce the swirling flow in a vessel (Pöllänen et al., 2005).

Cavities are formed in the low-pressure regions of the impellers blade as the gas feed is increased. Figure 13 shows the fluid flow when six blades Rhuston turbine impeller is used in a vessel. Rushton turbine used was selected because of its ability of gas-handling. Flooding can be avoided even at high gas feeding rate (Paul et al., 2004, p. 601).

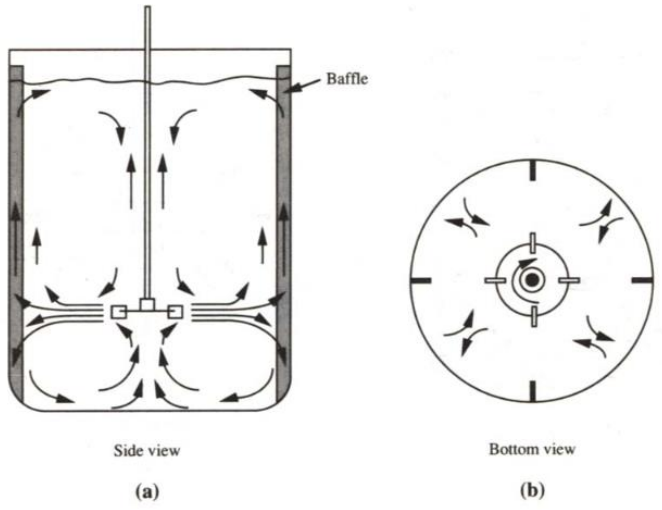

Figure 13. Flow pattern produced by a radial-flow impeller in a baffled tank.

7.1 Sparger

There are different designs of sparger such as perforated tubes, simple open pipes, two-phase complex injector devices and porous diffusers. Point sparger, which spreads bubbles at specified location in the tank. Ring sparger releases the gas from multiple outlets. Bubbles released through the sparger have a range of narrow size depending on type of sparger. As the bubble rises from the sparger into impeller zone, it was broke-up by the shear force with the agitator. Usually sparger type has no influence on the mixing in the vessel although the number of outlet bubbles, and distance between the sparger and agitator have influences on efficiency of the dispersion of the gas (Doran, 2013).

7.2 Design of crystallizer

A cylindrical tank equipped with four baffles symmetrically arranged on the inner side of the wall of the stirred tank is shown in Figure 14. It presents the experimental stirred tank, with one baffle cut off to explain the inner design of the stirred tank for crystallization (Torotwa and Torotwa, 2018).

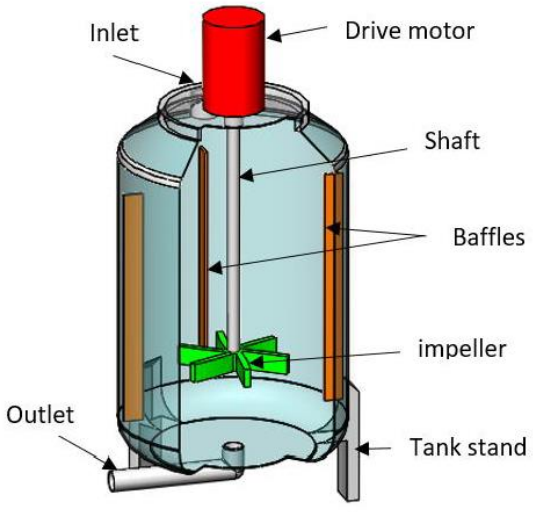

Figure 14. 3 dimensional representation of a stirred tank with other components (Torotwa and Torotwa, 2018).

Experimental part

8 Mixing

8.1 Reynolds number and flow regime

According to Doran, (2013), mixing is affected by several parameters. The first important parameter is Reynolds number. Reynolds number depends on the impeller diameter and its tip speed stated in Eq. 25. The flow regime of turbulent, laminar and transition is predicted.

$$Re = \frac{\rho N D^2}{\mu} \qquad \text{Eq. 25}$$

Where Re is the impeller Reynolds number, N is the stirrer speed, D is the impeller diameter, ρ is the fluid density, and μ is the fluid viscosity.

The Reynolds number is a dimensionless variable. Flow is laminar at Re<10 and turbulent at Re>10^4. Transition region of Reynolds number is between 10 and 10^4 (Doran, 2013).

Table 1. Flow prediction by calculating Reynolds number.

Agitation, rpm	Reynolds number (Re) at 25°C temperature	Reynolds number (Re) at 50°C temperature	Flow-regime
400	13790	22474	Turbulent
500	17238	28069	Turbulent
600	24637	33704	Turbulent

Table 1 shows the flow-regime prediction at different impeller agitation (400 rpm, 500 rpm and 600 rpm) by calculating Reynolds number using Eq. 25 and it was observed that the flow is turbulent at 400, 500 and 600 rpm.

8.2 Power number and power consumption

For a specific speed of stirrer, the required power depends on solution in a vessel. It is important to know about the energy consumption for optimization of the process economics.

$$N_p = \frac{P}{\rho N^3 D^5} \qquad \text{Eq. 26}$$

In Eq. 26, Np is stirrer speed, D is impeller diameter, ρ is fluid density, μ is fluid viscosity, and P is power.

Reynolds number and power number relationship is evaluated experimentally for specified impeller and tank dimension shown in Figure 15.

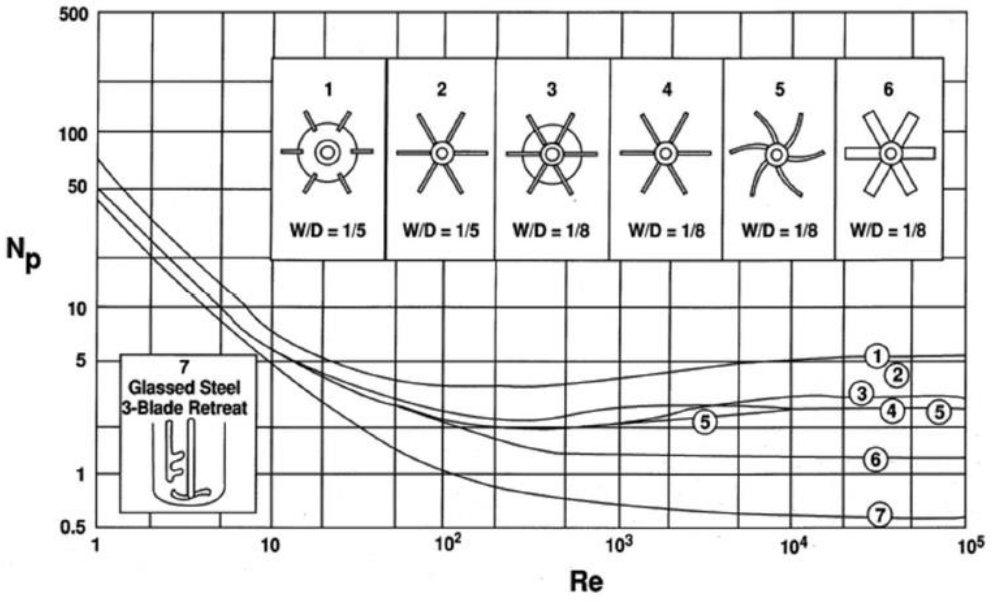

Figure 15 Power number at different Reynolds number for different kind of impellers (Robert et al. 1988).

For Rushton turbine (impeller 1), according to Reynolds number listed in Table 1 the power number (N_p) is 5 for impeller speed 400, 500 and 600 rpm. Detailed calculated data is shown in Table 2.

Table 2. Power number (Np) and power consumption calculation at different impeller speed

Agitation rpm	Reynolds number (Re) at 25oC temperature	Reynolds number (Re) at 50oC temperature	Power number (Np)	Power, W
400	13790	22474	5	0.15
500	17238	28069	5	0.29
600	24637	33704	5	0.60

Once the value of N_p is known, the power can be calculated from Eq. 26. Mixing power is affected by the impeller configuration, impeller speed and fluid properties such as viscosity and density.

The power (W) calculated are 0.15, 0.29 and 0.6 at impeller speed of 400, 500 and 600 rpm respectively, which is shown in Table 2.

8.3 Impeller flooding for gassed tanks

In the aerated stirred tank reactor system, to minimize losses in aerated stirred tank reactor under optimal operating condition, flooding characteristics in stirred tank plays an important role (Cai *et al.,* 2010*)*.

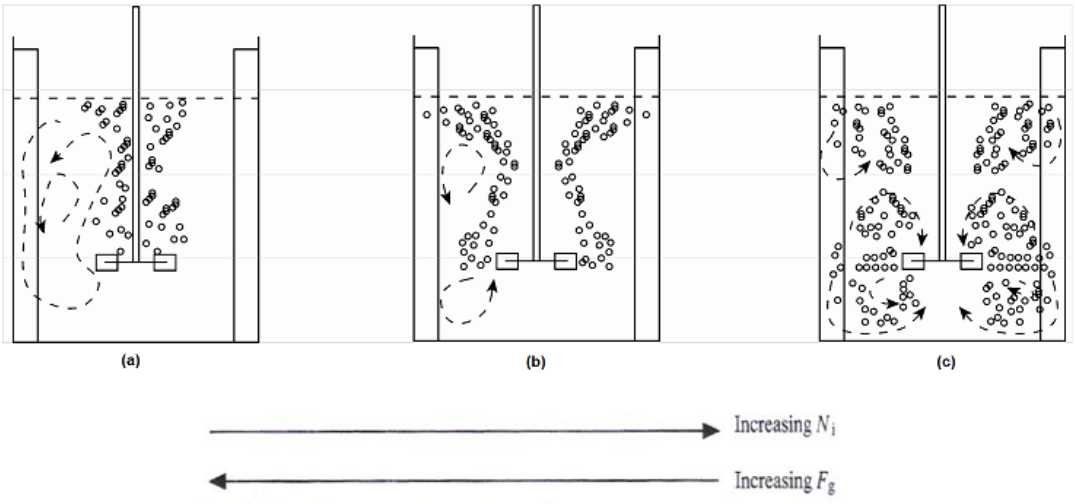

Figure 16. Gas spreading arrangements in an aerated stirred tank having Rushton turbine in used as agitator is represented by N_i and gas feed rate F_g. (a) impeller flooding, (b) impeller loading, (c) complete gas dispersion (CAI *et al.,* 2010)

According to Cai et al. (2010), poor gas hold up and performance is due to the passing around of gas bubbles through the shaft and impeller, loading shown in

Figure 16. The gas is well dispersed in the upper region of the vessel by the impeller and the vessel where the gas is scattered evenly in all parts by the impeller is known as complete gas dispersion.

8.4 Impeller speed calculation to avoid flooding

Eq. 27 shows complete gas dispersion in an aerated stirred tank (Van't Riet 1991).

$$\frac{F_{gs}}{ND^3} < 0.3\frac{N^2D}{g} \qquad \text{Eq. 27}$$

Where F_{gs} is volumetric gas flow rate at constant pressure, N is stirring speed. D is impeller diameter and g is gravitational acceleration (Van't Riet 1991).

It can be seen from Table 3 that the minimum impeller speed calculated using Eq. 27 is less than the impeller speed 500 and 600 rpm used in the experiment. The value of $\frac{\mathrm{F_{gs}}}{\mathrm{ND^3}}$ is less than $0.3\frac{\mathrm{N^2D}}{\mathrm{g}}$ for the parameters used in the stirred tank experiment. Therefore, it can be predicted that there is no gas flooding at gas flow rate of 0.5 L/min and 0.3L/ with impeller speed of 500 and 600 rpm.

Table 3. Prediction of gas flooding characteristics with the parameters used in aerated stirred tank experiment

Volumetric gas flow rate , L/min	Impeller speed, rpm	$\frac{F_{gs}}{ND^3}$	$0.3\frac{N^2D}{g}$	Minimum impeller speed to avoid flooding, rpm
0.5	500	0.018	0.081	304.37
0.3	500	0.011	0.081	256.72
0.5	600	0.015	0.116	304.37
0.3	600	0.009	0.116	256.72

8.5 Dimension of the crystallizer set-up

The schematic drawing of the tank and Rushton impeller are shown in Figure 18. The gas sparger used in this study is shown in Figure 17.

Figure 17. Sparger used in this study.

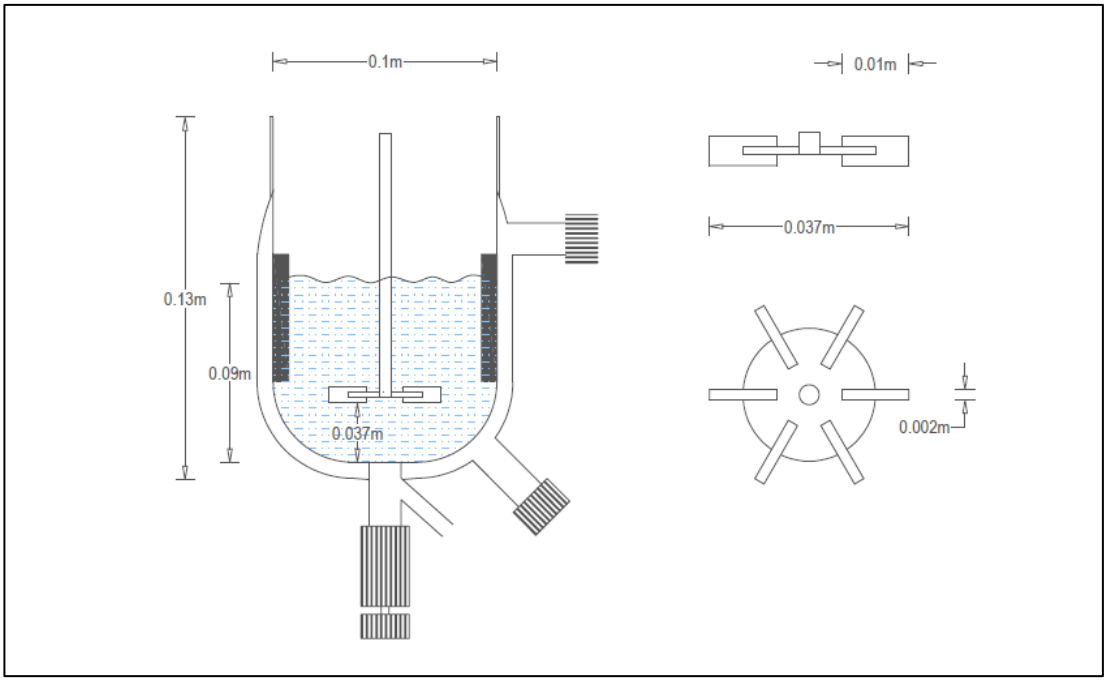

Figure 18. Dimensions of the Rushton impeller and tank used in this work

Table 4. Stirred tank specification used in this work

Stirred tank parts	Symbol	Value
Tank diameter	T	0.1 m
Impeller diameter	D	0.037 m
Blade height	W	0.003 m

Impeller distance from bottom	C	0.037 m
Baffle width	I_{Baffle}	0.01 m
Liquid height	H	0.01 m

8.6 Scale up of crystallizer

It is expensive and time consuming to study the optimum operating parameters at large scale production. Therefore, it is always recommended to study the optimum condition in a small scale before it is constructed in large scale.

Problems in scale up are the reasonable dissolution time, foam formation, the effect of geometry of the tank, selection of the mixing equipment and their critical operating variables such as temperature, gas feed rate, impeller speed (Robert et al, 1988).

Determine scale up ratio R (Robert et al, 1988).

$$\frac{V_2}{V_1} = \frac{\pi D_{T2}^3/4}{\pi_{T1}^3/4} = \frac{D_{T1}^3}{D_{T1}^3} \quad \text{Eq. 28}$$

Where, V_2 is the volume of scale up vessel, V_1 is the volume of original vessel, D_{T2} is the tank diameter of scale up vessel and D_{T1} is the diameter of original vessel

$$R = \frac{D_{T2}}{D_{T1}} = \left(\frac{V_{T2}}{V_{T1}}\right)^{\frac{1}{3}} \quad \text{Eq. 29}$$

Using the value of R, calculate the new dimensions of geometric sizes. That is

$$R = \left(\frac{400L}{0.4L}\right)^{\frac{1}{3}} \quad \text{Eq. 30}$$

$$R = 0.1 \quad \text{Eq. 31}$$

$$D_{A2} = RD_{A1} \quad \text{Eq. 32}$$

Where D_{A2} is the diameter of agitator of scale up vessel and D_{A1} is the diameter of agitator of original vessel.

9 Solubility of Li_2CO_3 in the Li_2SO_4-Li_2CO_3-H_2O ternary system

Solubility data is important in several experimental work for optimization and designing such as crystallization, process development of organic materials, screening of polymorph and salts, and analysis of chemicals (Black et al., 2013).

The objective of this work is to gain knowledge about solubility which is important in prediction of solubility of chemicals in solution and it is prerequisite for crystallization process by verifying the data of Stephen & Stephen, p668 solubility data of Li_2CO_3-Li_2SO_4-H_2O ternary electrolyte system with the help of FBRM (focused laser beam reflectance measurement) technology. The Particle Track is placed into the beaker containing dispersed system where the slurry flows closely the probe window. The focused beam reflectance measurement worked in such a way that the high speed rotation of laser beam and spread over the particles in the slurry which is being studied. The backscattering of the signal into the probe happens when the particle comes in front of the probe and focused beam crosses that particle. The chord length is calculated in electrical system and these electrical signals are converted into the chord particle count and information of the dimension of the particle. Sampling time can be of 2 seconds where a new CLD information can be recorded the process dynamics (Dave et al., 2017)

9.1 Solubility prediction of Li_2CO_3 in the Li_2SO_4-Li_2CO_3-H_2O electrolyte system

Pitzer model parameters database for this Li_2CO_3-Li_2SO_4-H_2O is not developed extensively. The predicted model did not fit with the reference data due to lacking data on Pitzer parameters.

Pitzer thermodynamic modeling requires three stages. Firstly, the average activity coefficient of Li_2CO_3 calculated by using different modalities in a pure binary Li_2CO_3-H_2O solution at 25°C, which is shown in Eq. 9. Secondly, solubility product constant is calculated of Li_2CO_3 at 25°C. Solubility product is calculated using the solubility of Li_2CO_3 in the Li_2CO_3-H_2O binary system at 25°C (Myerson 2002).

$$K_{SP(Li_2CO_3)} = (\gamma * m)^2 * (\gamma * m) \qquad \text{Eq. 33}$$

To calculate activity coefficient in the ternary system, Eq. 18 and Eq. 19 can be used.

Ion-Interaction parameters for lithium carbonate for predicting Pitzer thermodynamic model at 25°C are shown in Table 5.

Table 5. Ion-Interaction parameters for predicting Pitzer thermodynamic model at 25°C (Denf et al., 2002)

Interaction	$\beta^0_{Li_2CO_3}$	$\beta^1_{Li_2CO_3}$	$C^{\varphi}_{Li_2CO_3}$
	-0.389335	-2.27267	-0.162859

Pitzer mixing parameters for Li^+, CO_3^{-2} and SO_4^{-2} was not available and the mixing parameters shown in Table 6 are used to develop the model.

Table 6. Pitzer model parameters (Pitzer, 2019)

Mixing parameters	$\theta_{CO_3^{-2},SO_4^{-2}}$	$\theta_{Na^+,SO_4^{-2}}$
	0.02	-0.005

Predicted solubility model is compared with the reference data, which is shown in Figure 19.

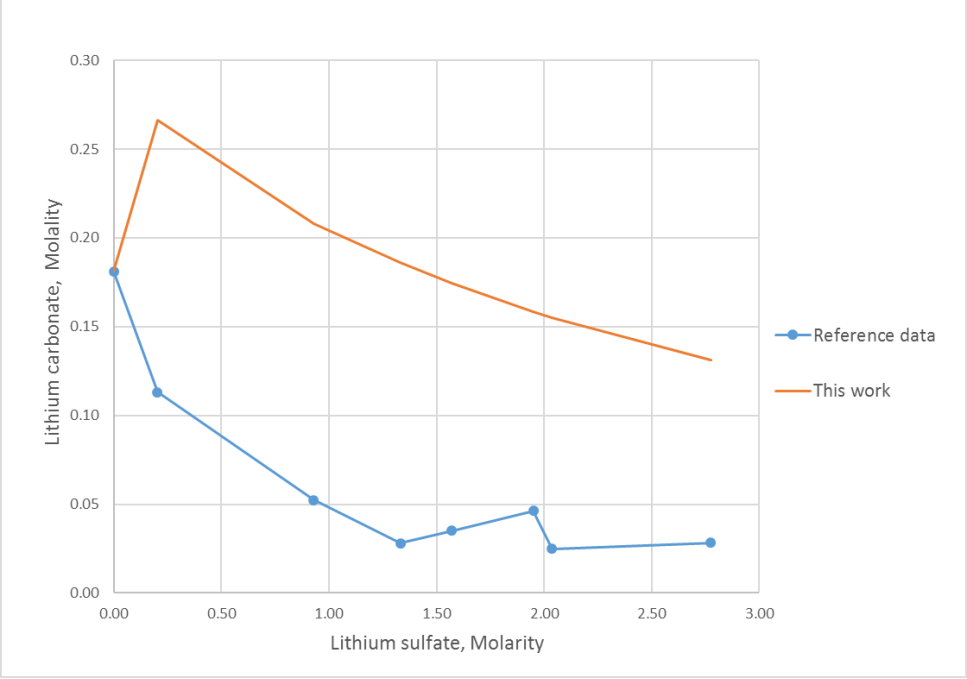

Figure 19. Predicted solubility data compared with reference data.

9.2 Characterization of precipitated lithium carbonate.

All the crystallized lithium carbonate samples were analyzed with X-Ray Diffraction with PANalytical X'pert Pro MPD Powder using Cobalt radiation source and

operated at 40kV with 40 mA. In addition, Scanning Electron Microscope (SEM) Hitachi TM-4000Plus was used to identify lithium carbonate morphology. SEM pictures were taken at least using three different magnifications. To determine crystal size distributions, Mastersizer 2000 was used. Counts were observed with Mettler Toledo Particle Track having (FBRM) technology. Conductivity and pH were recorded and observed with Consort C3050.

9.3 Chemicals

For the solubility measurements of lithium carbonate in lithium sulfate solution, the synthetic solution was prepared with analytical-grade lithium sulfate anhydrous [Li_2SO_4] (purity ≥ 99.7 %, Alfa Aesar) and lithium carbonate [Li_2CO_3] (purity≥99%).

9.4 Experimental setup and procedure

The experiments were carried out according to the procedure published in the reference Black et al., 2013. The solid-liquid equilibrium experiments were carried out by adding a water into the supersaturated solution ($Li2CO_3$-Li_2SO_4-H_2O) in a 250mL cylindrical beaker and particle track immersed into the beaker, which is shown in Figure 20. Each sample was stirred at room temperature. Supersaturated solutions of initial mass of 100g Li_2CO_3-Li_2SO_4-H_2O was prepared for each experiments.

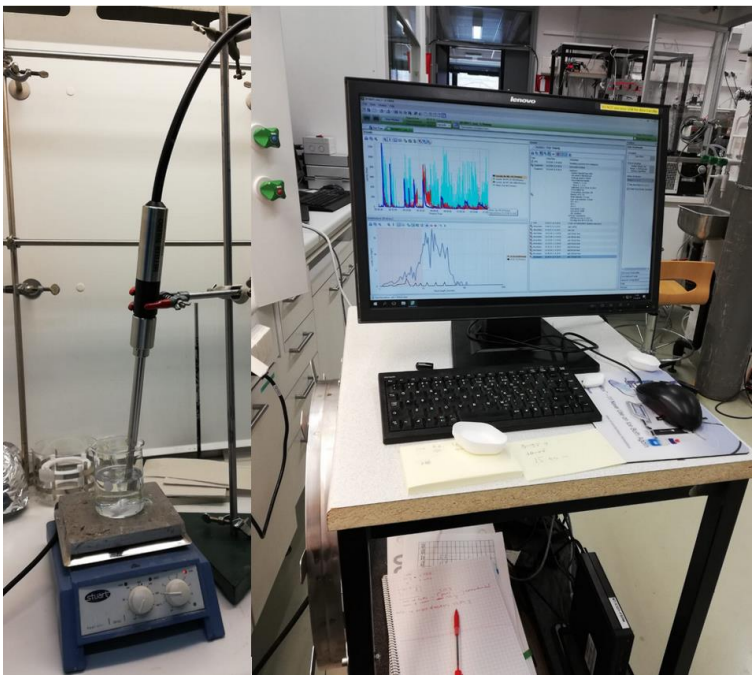

Figure 20. Experimental set-up of the solubility measurement of Lithium in ternary electrolyte system.

To prepare a Li_2CO_3-Li_2SO_4-H_2O supersaturated solution, Table 8 shows that three experiments were performed with weight of lithium sulfate of 3.26g, 27.41g and 35.01g and weight of lithium carbonate was 0.5g, 0.2g and 0.2g respectively with 70g of water initially according to the measured solubility results published by Stephen and Stephen (Table 7). Firstly, required amount of lithium sulfate was weighted on balance with accuracy 0.01g. Then 70g of water was added and stirred with a magnetic stirrer. Time of 10-15 min was given for dissolution. Compete dissolution was verified visually to check that there was no solids remained. While preparing lithium sulfate solution, there were initial yellow precipitates similar as in heterogeneous reactive crystallization, which is shown in Figure 23. 2.7-µm micro-filters Whatman filter paper (No. 50) was used to remove the yellow precipitates through filtration under vacuum using Büchner funnel. The filter paper was wetted with the distilled water and tap water made a certain vacuum. The impurities obtained after filtration, similar as impurities obtained in heterogeneous reactive crystallization, which is shown in Figure 25 which was later analyzed in Energy Dispersive X-Ray Spectroscopy *(*EDS*).* A clear filtrate was obtained after filtering out the initial impurities, and then poured into 250mL glass beaker. Mettler Toledo

Particle track with FBRM technology was immersed in the beaker for the real time particle size and count analysis. Then water is weighed and added in the Li_2CO_3-Li_2SO_4-H_2O supersaturated solution drop by drop with the help of laboratory plastic pipette and gradually all the solid dissolve. It is important to check that the slurry has been in a homogeneous state. Mettler Toledo Particle track was used to observe the equilibrium status between solid and liquid due to the increase of solvent volume.

Table 7. Solubility data of Li_2CO_3-Li_2SO_4-H_2O (Stephen and Stephen 1964).

Weight percent Li_2CO_3	Weight percent Li_2SO_4	Weight percent water	Temperature, ^oC	Comp. of solid phase
1.32	0	98.68	25	Li_2CO_3
0.81	2.17	97.02	25	Li_2CO_3
0.35	9.24	90.41	25	Li_2CO_3
0.18	12.76	87.06	25	Li_2CO_3
0.22	14.69	85.09	25	Li_2CO_3
0.28	17.61	82.11	25	Li_2CO_3
0.15	18.27	81.58	25	Li_2CO_3
0.16	23.34	76.5	25	Li_2CO_3

Table 8. Weight of chemicals required according to stephen and stephen data for 100 g of total solution.

Li_2CO_3, g	Li_2SO_4, g	Water, g
0.8	2.17	97.02
0.4	9.24	90.41
0.2	18.27	81.58
0.2	23.34	76.50

10 Precipitation of lithium carbonate from heterogeneous and homogeneous reactive crystallization

10.1 Materials and Methods

10.2 Chemicals

For the lithium carbonate precipitation in heterogeneous system, the synthetic solution was prepared with analytical-grade lithium sulfate anhydrous [Li_2SO_4] (purity ≥ 99.7 %, Alfa Aesar). Sodium hydroxide [NaOH] (≥ 98 %, Sigma-Aldrich) solution was prepared. Carbon dioxide (CO_2) and used to precipitate lithium carbonate.

For the lithium carbonate precipitation in homogeneous system, the synthetic solution was prepared with analytical-grade lithium sulfate anhydrous [Li_2SO_4] (purity ≥ 99.7 %, Alfa Aesar), instead of sodium hydroxide [NaOH] and carbon dioxide (CO_2), anhydrous sodium carbonate [Na_2CO_3] (purity ≥ 99.9%, EMSURE®) was selected and used to precipitate lithium carbonate.

10.3 Precipitation of Li_2CO_3 by heterogeneous reactive crystallization

10.3.1 Experimental setup and procedure

The experimental setup can be seen in Figure 21 and Figure 22. The experiments were all carried out in a baffled stirred vessel, with a diameter of 0.1m and a height of 0.13m. Teflon Rushton turbine with 6 blades having diameter of 0.037m was used to achieve the desired stirring rate, which is shown in Figure 18. The Rushton turbine used was selected because of efficient gas-handling.

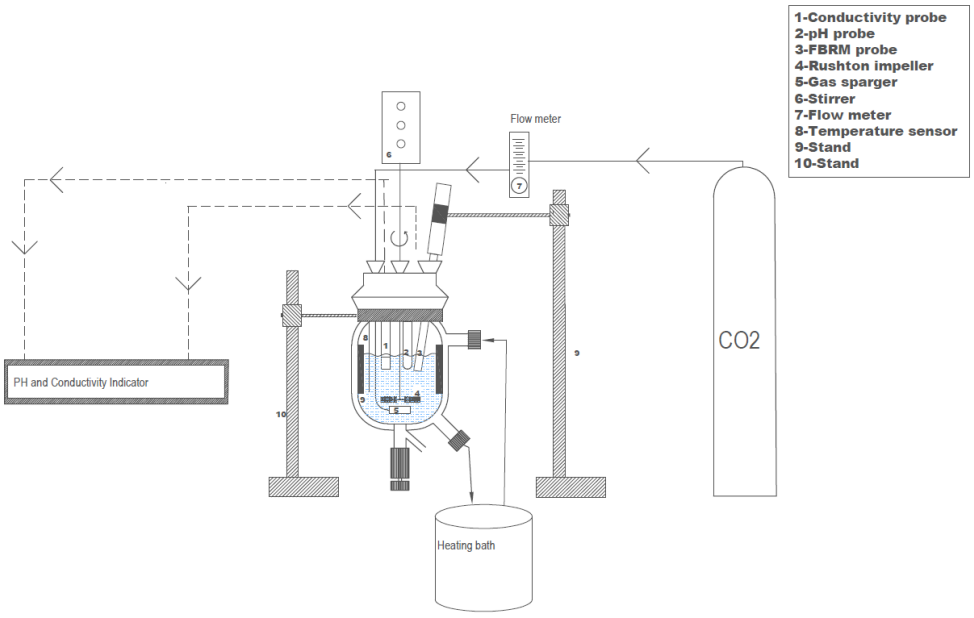

Figure 21. Schematic drawing of precipitation of lithium carbonate in heterogeneous system setup.

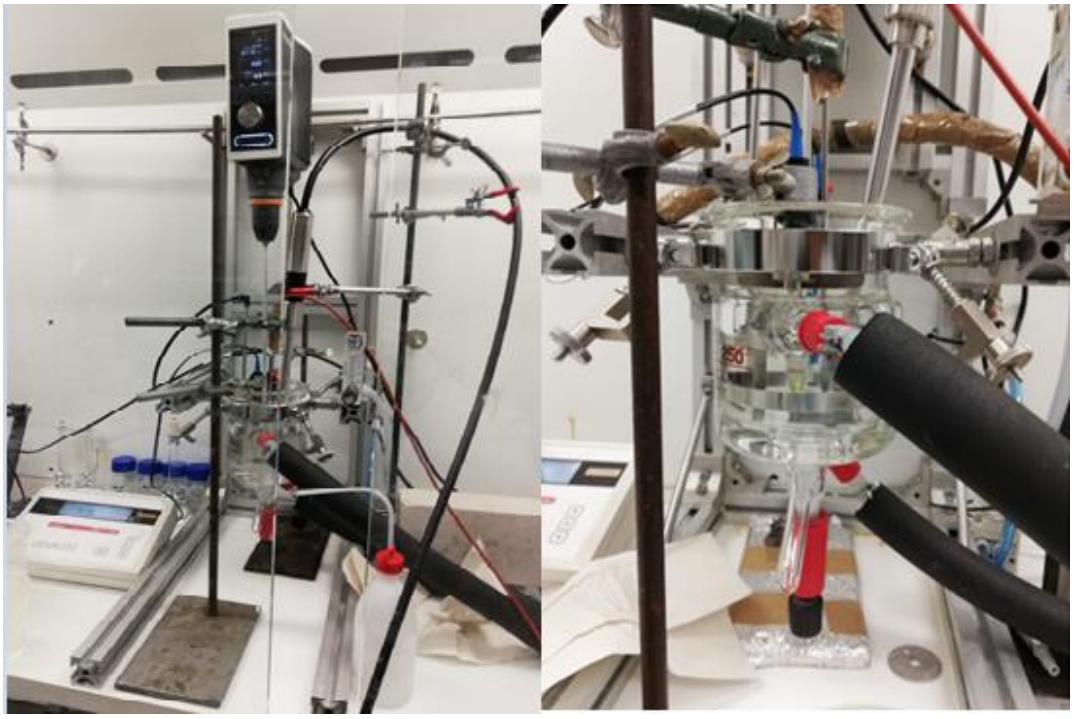

Figure 22. Experimental setup of lithium carbonate precipitation in heterogeneous system.

Lithium sulfate is soluble in water. The trend of lithium sulfate solubility shows that its solubility decrease with increase of temperature. The density of anhydrous lithium sulfate is 2.22 g/cm^3. Lithium sulfate has the ability to absorb moisture from the environment, therefore it was stored under the nitrogen atmosphere.

To prepare a solution having lithium concentration of 20g/L, 47.5 gms of lithium sulfate were weighed using a balance manufactured by Kern 572 precision of 0.001 g in a 600 mL beaker. 300 mL of water was added and stirred with a magnetic stirrer. The solution was mixed for 10-15 min and verified visually to check that no solids remained. There were some initial yellow precipitates formed while preparing lithium sulfate solution shown in Figure 23 and the impurities were separated using same procedure and analyzed in same way as mentioned previously in solubility studies of lithium carbonate in ternary system.

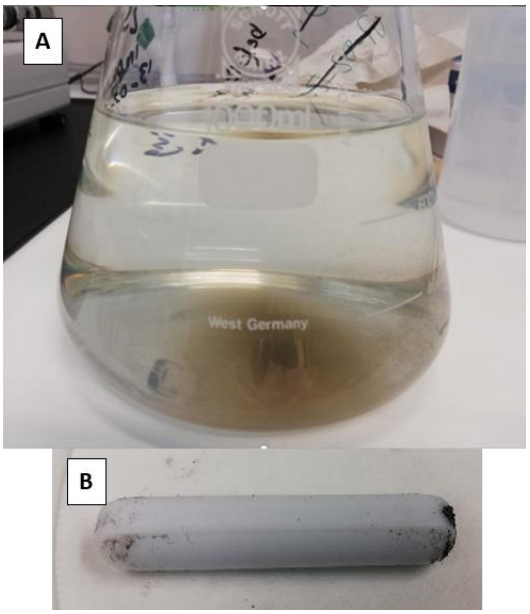

Figure 23. Yellow precipitates in the lithium sulfate solution (A) and impurities attached to the stirrer (B).

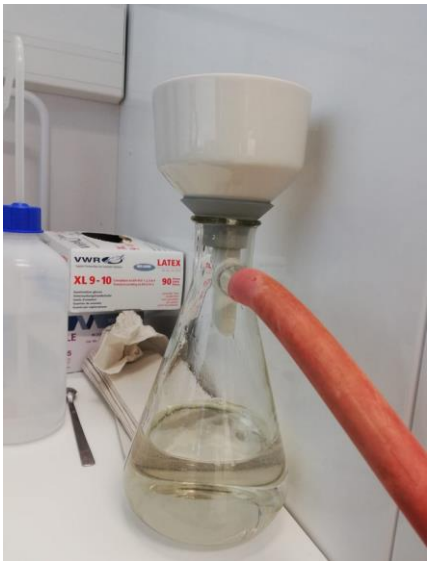

Figure 24. Vacuum filtration under Büchner funnel.

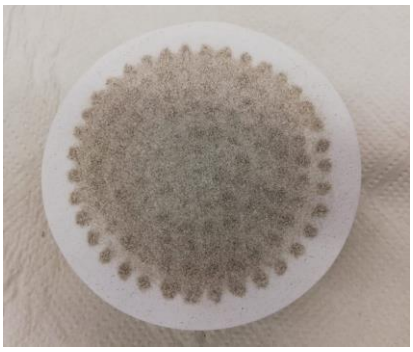

Figure 25. Impurities obtained after filtration.

Sodium hydroxide is termed as inorganic compound, also known as caustic soda. Sodium hydroxide is an extremely caustic base and alkali. Sodium hydroxide is extremely soluble in water and absorbs carbon dioxide and moisture from air. Different molarities of sodium hydroxide (NaOH) such as 1M and 5M were prepared. Molecular weight of sodium hydroxide is 40 gms (Addition of atomic mass of Na=23, O=16, H=1). Sodium hydroxide with concentration of 5 M was used to adjust the pH. To prepare 5 M sodium hydroxide solution, Firstly, 20g sodium hydroxide pellets and 50 mL of distilled water were added in 300 mL beaker and stirred with a magnetic stirrer. Then, it was transferred to a 100 mL volumetric flask after the solution cooled down. More distilled water was then added to the scale mark and stored in a glass sealed bottle.

The lithium sulfate solution after removal of impurities solution was transferred to a jacketed Pyrex cylindrical stirred reactor equipped with a thermostat (Lauda RK 8 CS). An external temperature probe connected with the thermostat was immersed into the solution and the temperature of the solution is thermostatically controlled. pH probe, and conductivity probe were immersed into the solution in the reactor to monitor the changes of conductivity, pH and temperature with a multiparameter analyzer (Consort C3050). The Mettler Toledo Particle Track with FBRM technology was immersed in the reactor for the real time particle size and count analysis. Four baffles in the reactor were placed symmetrically for efficiency mixing and ensure that there was no vortex formation. The mixing of the solution was done by using a Rushton impeller with 6 blades to reduce the effect of temperature and concentration gradient in the solution.

Experiments were carried out with various parameters shown in Table 9. When the solution achieved the target temperature, then 100 ml of 5 M soda (NaOH) was poured into the reactor and then wait till the temperature was constant. Then carbon dioxide (CO_2) gas was fed to the reactor through a pipe connected to a gas cylinder. A sparger with 1mm pore size was placed at the bottom of the reactor and used to distribute CO_2. The CO_2 was stopped when target pH achieved. Then the whole system was kept stirring 30min for ageing. After adding CO_2 gas, the suspension was seen in a short time. After ageing, precipitates were vacuum filtered with a Büchner funnel and a filter paper (VWR European Cat. Not. 516-0350 12-15-µm). The weight of crystals, dish, moisture and filter paper were recorded and placed into the oven for 24 hours drying. Yield was calculated based on the mass of the dry samples. The crystals were analyzed with XRD, SEM and particle size distribution.

Table 9. Parameters used in the precipitation of lithium carbonate in heterogeneous system.

Temperature, ^{o}C	Gas flow rate, L/min	Impeller, rpm
25	0.3	600
25	0.3	500
25	0.5	600
25	0.5	500
50	0.5	600
50	0.5	500
50	0.3	600
50	0.3	500

10.4 Precipitation of Li_2CO_3 by homogeneous reactive crystallization

10.4.1 Experimental setup and procedure

Preliminary experiments were carried out in a 40ml beaker. The experimental setup shown in Figure 26 was used in lithium carbonate precipitation based on homogeneous system. Experiments consist of a 40 ml beakers having a magnetic stirrer, a syringe needed to add sodium carbonate into the 40mL containing lithium sulfate solution. Conductivity and pH probe were immersed in the reactor to monitor the changes of conductivity and pH with a multiparameter analyzer (Consort C3050).

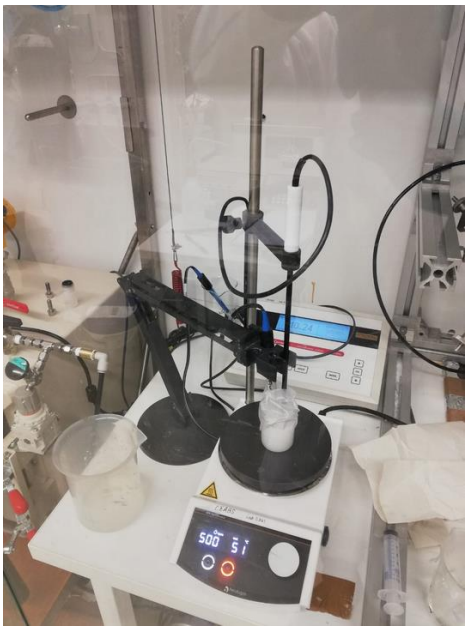

Figure 26. Experimental set-up used for preliminary tests (Homogeneous system).

45.79 g of sodium carbonate was prepared in 102mL deionized water and kept in a water bath shaker at 50^{o}C for 72 hours. 15.84 g of lithium sulfate was added in 100mL deionized water. At the beginning 30mL lithium sulfate solution was taken into the 40mL beaker. 10mL saturated sodium carbonate was added. First experiment was performed without adding sodium hydroxide and rest with sodium hydroxide at stirring speed of 500 rpm.

After the preliminary tests, 47.51 g lithium sulfate in 300mL of distilled water was prepared as discussed before in heterogeneous reactive crystallization and transferred in a baffled stirred vessel as discussed before, which is shown in Figure 29. Saturated sodium carbonate solution was prepared in a 300mL jacketed Pyrex cylindrical reactor shown in Figure 30. The reactor was equipped with a thermostat (Lauda E 200) and the solution was mixed with a magnetic stirrer and complete dissolution was ensured by visual examination. An external temperature probe was immersed into the disperse system and used to control the temperature of solution thermostatically. The arrangement of the set-up was similar as discussed before in heterogeneous reactive crystallization. Experiments were carried out at 50^{o}C, two stirring speed (500 and 600 rpm) and 30 min ageing.

Table 10. Parameters in the precipitation of lithium carbonate in homogeneous system.

Impeller speed, rpm	Na_2CO_3 flow rate, mL/min	Residence time, min
500	2.54	40
600	2.54	40
600	4.42	23
500	4.42	23
500	5.65	18
600	5.65	18

When the lithium sulfate and sodium carbonate solution achieved 50^{o}C, sodium carbonate was pumped into the reactor containing lithium sulfate solution with a peristaltic pump (Easy Load II 77200-60) at different flow rates of 2.54, 4.42 and 5.65 mL/min (residence time 40, 23, and 18 min, respectively). In the experiments, two different mixing rates and three different residence times were used show in Table 10. A schematic representation of experimental setup is given in Figure 27.

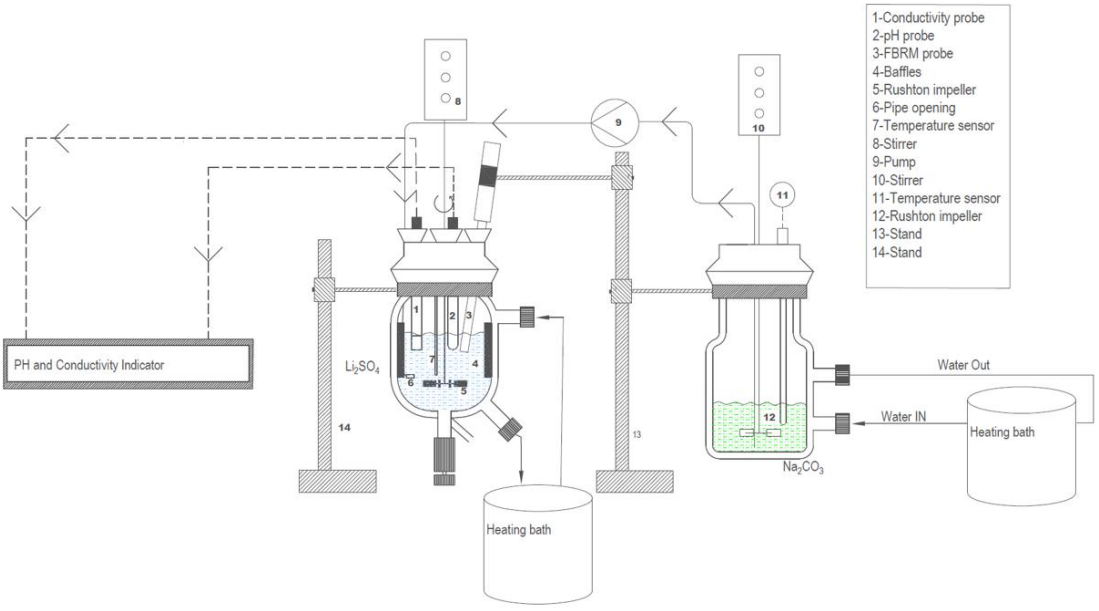

Figure 27. Schematic drawing of homogeneous reactive crystallization set-up.

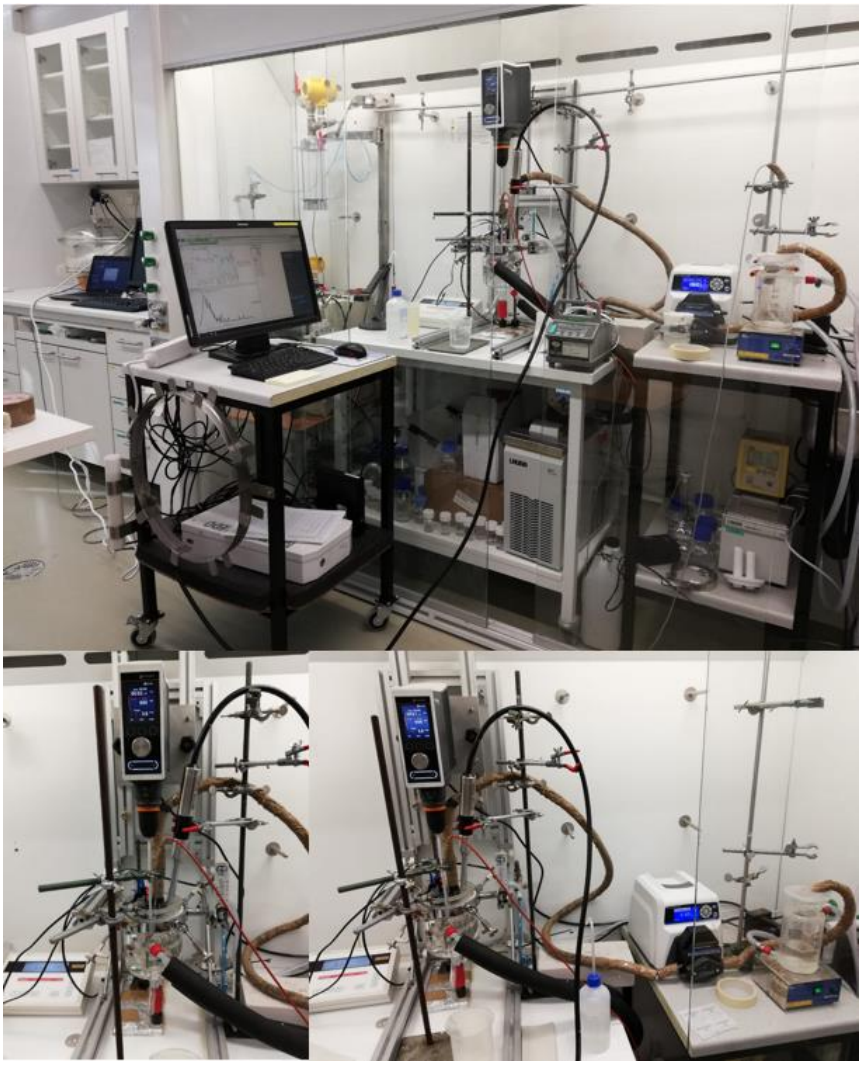

Figure 28. Experimental setup of lithium carbonate homogeneous reactive crystallization system.

The crystal yield and filter cake moisture were determined in a similar manner as described in section 10.3.1.

Figure 29. Close-up of the continuous stirred tank reactor used in the experiment.

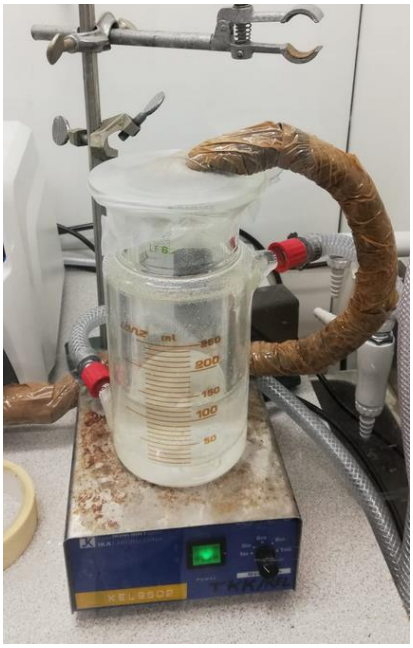

Figure 30. Close-up of the sodium carbonate dissolution vessel.

11 Cake filterability and Compressibility

The objective of this work was to perform experimental study to observe the filterability and compressibility concerning the product obtained through precipitation in homogeneous and heterogeneous system. Laboratory scale tests are important to provide useful information required for a filter design and crystal properties.

11.1 Material, experimental setup and method

11.1.1 Material preparation

The material used here was the precipitates obtained from crystallization in homogeneous and heterogeneous system. 10g of solids was added in a 350mL clear solution (mother liquor) obtained from the filtration by Büchner funnel after crystallization. The density of the suspension was around 1100 kg/m^3 and all the experiments were performed at solid concentration of 28 g/L.

11.1.2 Experimental setup and procedure

The filterability test performed was explained by Kobe et al., 1958. Firstly, approximately 10 Vol-% of solid concentration of slurry was prepared and then the solids-liquid separation was performed through the vacuum filtration. The filtration experiments were carried out with a laboratory-scale vacuum filtration unit prepared by eLabs having a data collection program which has the accuracy of 0.01bar. A photo of the filter is shown in Figure 32 and the schematic experimental setup can be seen in Figure 31. Filtration was performed using filter paper provided by VWR European Cat. Not. 516-0350 12-15µm that having 0.06m diameter and area of 0.002827m^2. The vacuum was created by a vacuum pump. Data collection program can record data every 2 s. The constant vacuum filtration experiments were conducted in 80 mbar, 60 mbar, and 40 mbar. In each filtration experiment, the pressure was kept constant.

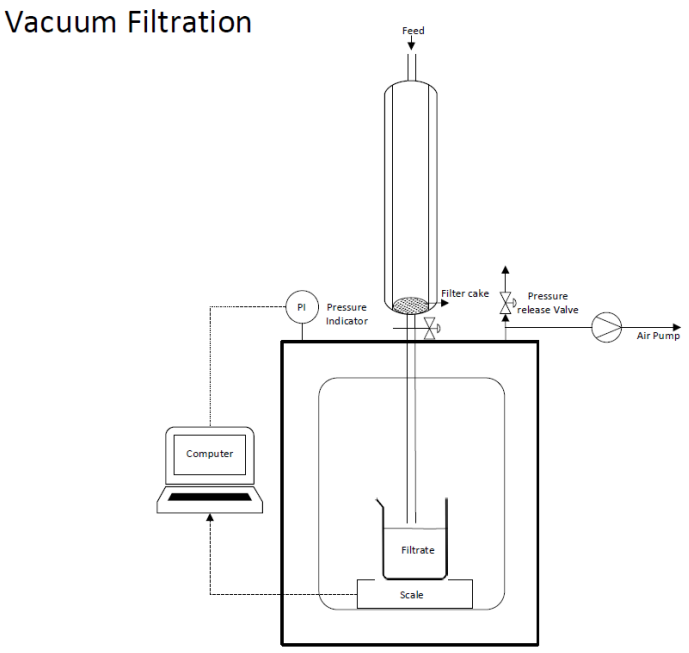

Figure 31. Schematic drawing of experimental setup of vacuum filtration.

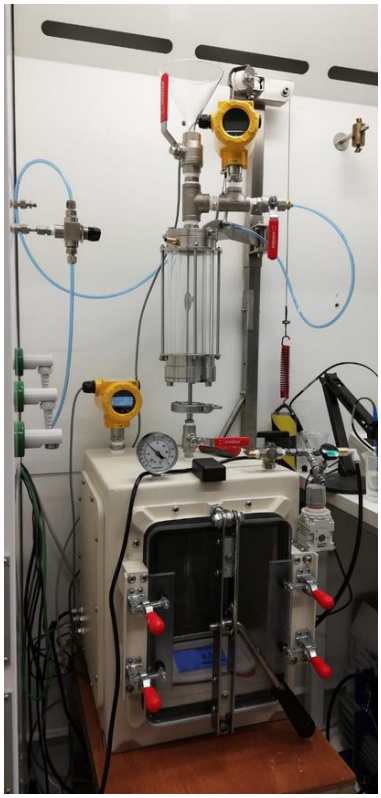

Figure 32. Experimental setup-up of vacuum filtration.

Fluid flows through a filter medium by virtual of pressure differential across the medium when solids are separated forming a filter cake.

The overall pressure drop is $\triangle p$ ($\triangle p = \triangle p_K + \triangle p_{SV} = (p_1 - p_2) + (p_2 - p_2)$).

Eq. 34 was used to plot t/V versus V. Then, K/2 is calculated as it is slope of the line while *B* is the y intercept.

$$\frac{t}{V} = \frac{K}{2}V + B \qquad \text{Eq. 34}$$

Where,

K and B= constants

V = Volume of filtrate, m^3

$\triangle p$ = Change in pressure, pa

$\triangle p_K$ = Pressure drop through cake, pa

$\triangle p_{SV}$ = Pressure drop through filter media, pa

Specific cake resistance (α) and compressibility (S) is obtained from Eq. 35.

$$\log(\alpha) = \log(\alpha_0) + Slog(\triangle p) \qquad \text{Eq. 35}$$

Where

α = Specific cake resistance, m/kg

S = Compressibility of cake, dimensionless

12 Results and Discussion

12.1 Solubility of Li_2CO_3 in the Li_2SO_4-Li_2CO_3-H_2O ternary system

As mentioned before, solubility data of Li_2CO_3-Li_2SO_4-H_2O ternary system at 25^oC have not been extensively study by other authors. Points from literature data chosen for solubility test and verify the solubility data from the literature is presented in Table 11 which shows mass of components in ternary system for comparison. It is concluded that the results from this work was not able to compare with the solubility data from the literature (Stephen and Stephen 1964), which is shown previously Table 7.

It can be seen in Figure 33 and Figure 34 , particle counts which is shown in the graph plotted by the Particle Track was not zero even after adding water stepwise for 1 hour. This was because the lithium sulfate solution still having some impurities even after filtration because the filter paper do not make a perfect seal on the Buchner, causing liquids to be able to get underneath the filter paper. The filter paper was wetted before filtration but still solution passes under the paper, resulting in not so efficient filtration.

The change in particle counts for solution with different weight percentage of lithium carbonate and lithium sulfate are shown in appendix II.

Table 11. Weight of components according to the solubility points of the literature.

Li_2CO_3 , g	Li_2SO_4 , g	Water, g
0.8	2.17	97.02
0.4	9.24	90.41
0.2	18.27	81.58
0.2	23.34	76.50

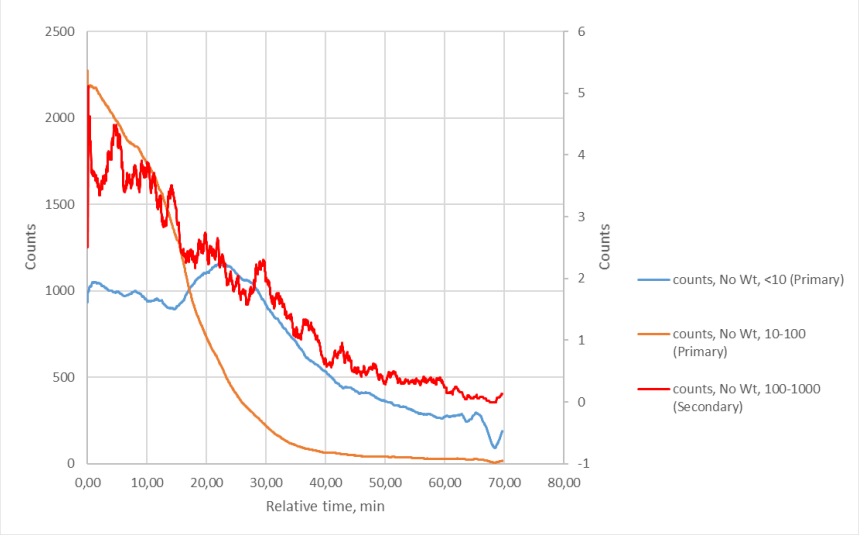

Figure 33. Change of particle counts as distilled water is added in solution having 0.2g of lithium carbonate and 18.27g of lithium sulfate.

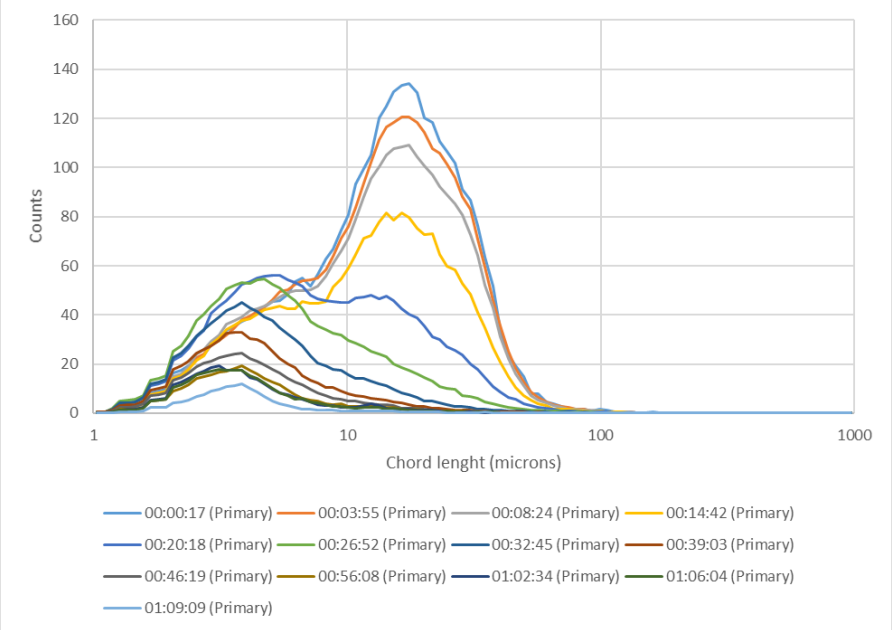

Figure 34. Chord length distribution of solution as distilled water is added 0.2g of lithium carbonate and 18.27g of lithium sulfate.

12.2 Precipitation of lithium carbonate from heterogeneous reactive crystallization

All the obtained results from precipitation of lithium carbonate in heterogeneous system experiments are explained in this chapter. The overall procedure of experimental structure is shown in Figure 35.

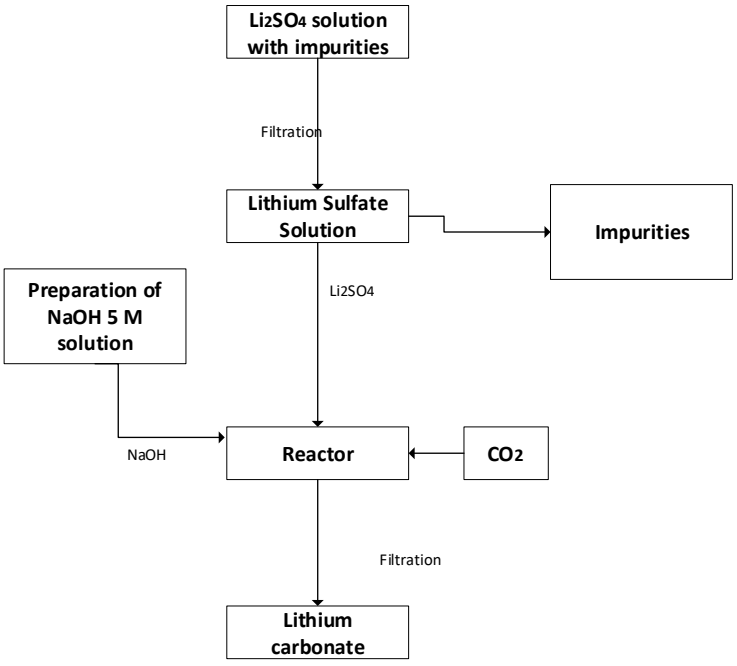

Figure 35. Experimental procedure

This chapters contains information of conductivity, pH, particle size distribution, shape of the crystals and impurities for the obtained crystal products.

Precipitation of lithium carbonate in heterogeneous system was investigated with different gas flow rates, two stirring rates, and two different temperature, which are tabulated in Table 9.

The first part of the experiments was carried out to determine the pH and conductivity of the experiments at 25^{o}C and 50^{o}C temperature. 100mL of sodium hydroxide was used to adjust the pH for all the experiments and it can be seen that the initial pH of the solution at 50^{o}C was between 9 and 9.5 shown in Figure 36 and initial pH of the solution at 25^{o}C was between 11 and 11.5.

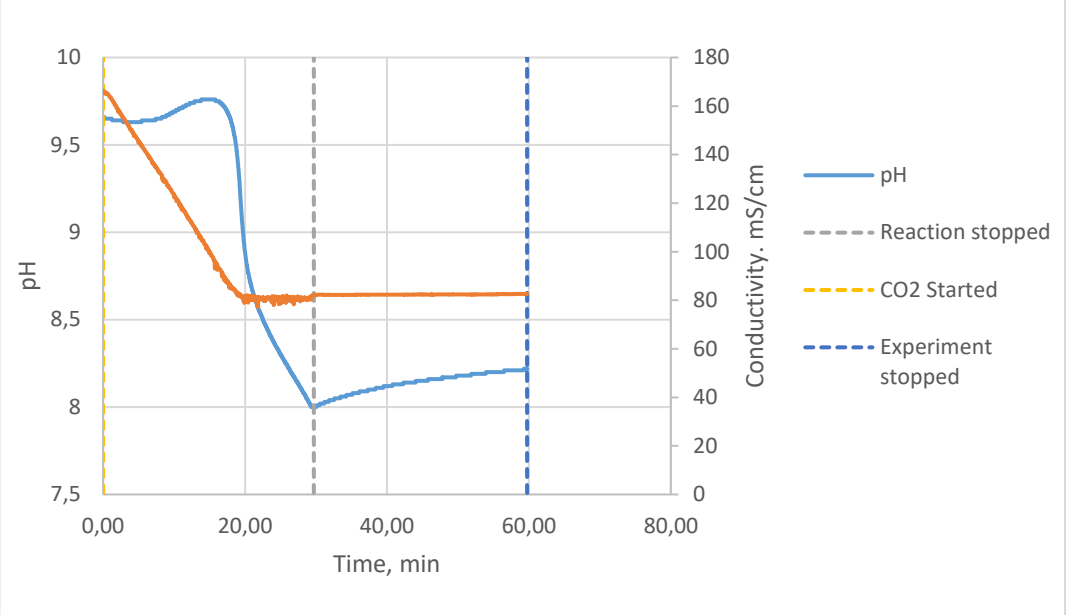

Figure 36. Conductivity and pH curves of experiment at 50°C, 500 rpm stirring rate, 0.3 L/min gas flow rate (29min residence time), 30min ageing. The experiment was stopped at pH 8.

Results in Li_2CO_3 precipitation shown in Figure 39 and Figure 41 indicate that the counts increases as a function of time.

Higher yield was obtained at 50°C, which is because the solubility of lithium carbonate is lower at higher temperature. The primary vertical axis shows pH curves and secondary vertical axis shows the conductivity changes in Figure 36. pH of the solution began around 9.6. After approximately 5 minutes suspension was seen and pH decreased sharply till the end of the reaction. The pH slightly increased during the ageing.

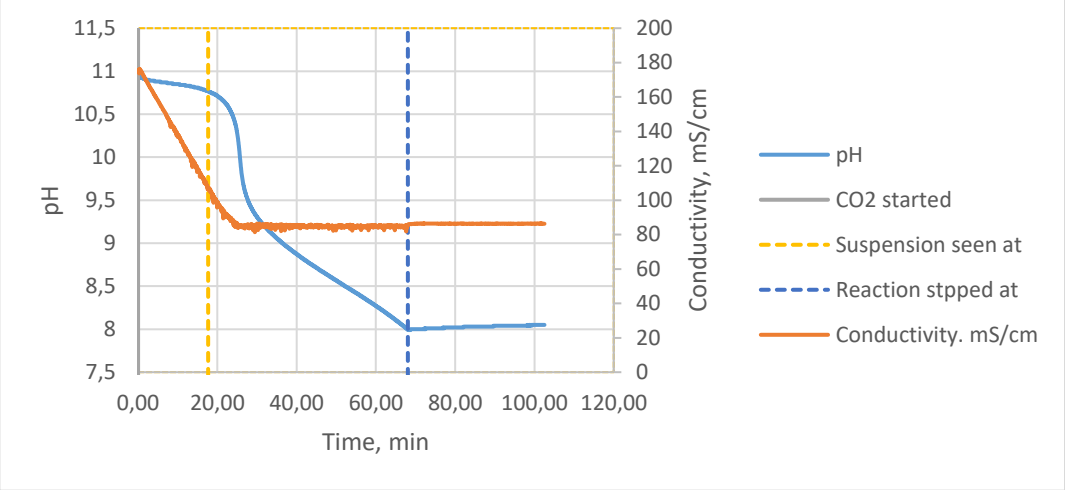

Figure 37. pH and conductivity curves of experiment at 25ºC, stirring rate of 500, gas flow rate of 0.3 L/min (68.03min residence time) and ageing of 30min. The experiment was stopped at pH 8.

Primary and secondary nucleation data obtained by the Particle Track, which is shown in Figure 39 and Figure 41. It was seen that crystals obtained by crystallization at 25ºC and 50ºC was less than 100 microns in terms of chord length.

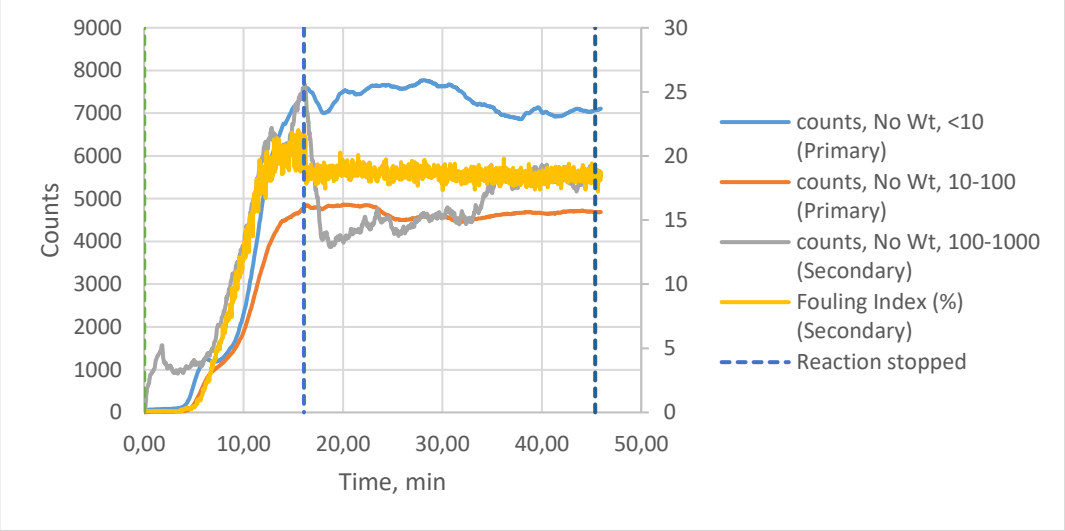

Figure 38. Counts with respect to time of experiment at 50ºC, stirring rate of 600 rpm, gas flow rate of 0.5 L/min (16.1min residence time), ageing of 30min. The experiment was stopped at pH 8.

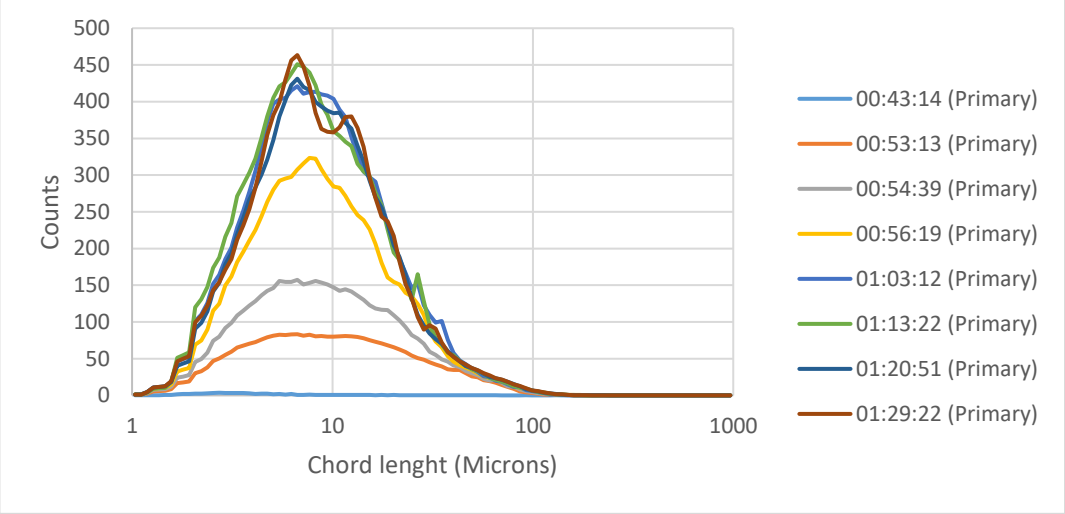

Figure 39. Chord length distribution of crystals obtained in experiment at 50°C, 600 rpm stirring rate, 0.5 L/min gas flow rate(16.1min residence time), 30min ageing. The experiment was stopped at pH 8.

Lower yield was obtained at 25°C. This could be because the $LiHCO_3/Li_2CO_3$ equilibrium reaction shifts towards $LiHCO_3$ at temperature below 50°C, which is shown previously in Eq. 7. Figure 37 shows the change in pH curve and conductivity in the heterogeneous reactive crystallization at 25°C. Nucleation time can be recognized from the counts curve obtained by particle track. pH of the solution begins with 11. After approximately 5 minutes suspension was seen and pH decreased sharply till the end of reaction. When the desired pH was achieved, CO_2 feed was stopped. pH and conductivity became constant during the ageing. On the other hand constant counts during ageing in Figure 40 shows that no significant change was seen during ageing.

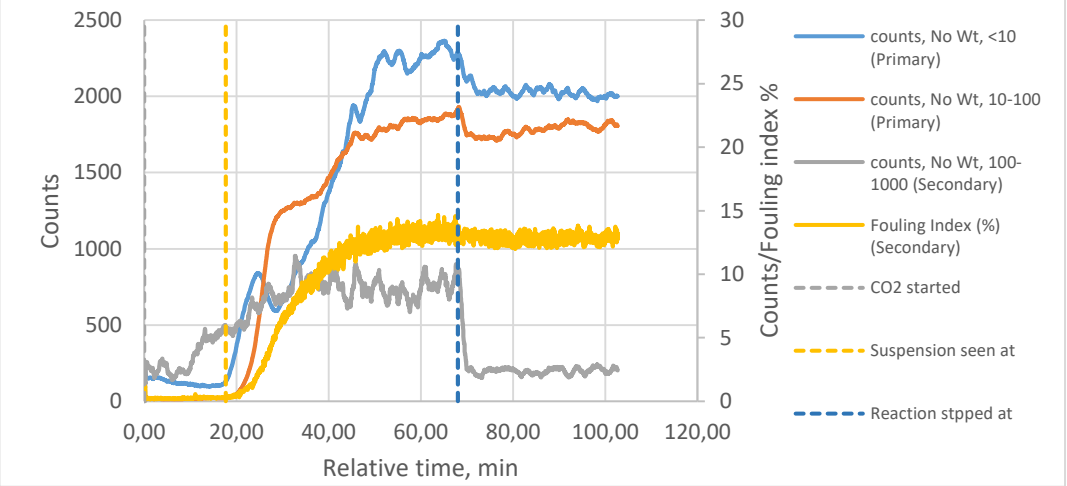

Figure 40. Counts with respect of time of experiment at 25°C, 500 rpm stirring rate, 0.3 L/min gas flow rate (68.03min residence time), 30min ageing. The experiment was stopped at pH 8.

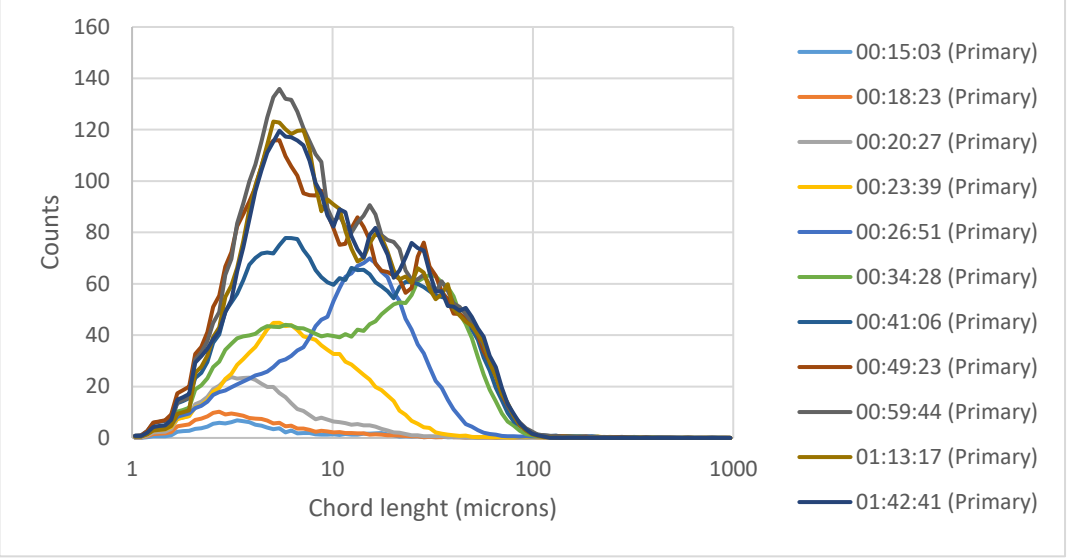

Figure 41. Chord length distribution of crystals obtained in experiment at 25°C, 500 rpm stirring rate, 0.3 L/min gas flow rate (68.03min residence time), 30min ageing. The experiment was stopped at pH 8.

12.2.1 Effect of temperature

Maximum product yield obtained at 25°C was around 44% and at 50°C was 78%. XRD analysis of the sample shows that the lithium carbonate was produced at 25°C. This result contradicts to the results obtained from Martin et al., (2017). According to Martin et al., (2017), at temperature higher than 50°C $LiHCO_3/Li_2CO_3$ equilibrium reaction shifts towards Li_2CO_3. In this study Li_2CO_3 was precipitated at temperature below 50°C.

Although the operational parameters are different, it is clear by comparing the trend of particle counts for two different temperatures (25^{o}C and 50^{o}C) during the experiment in Figure 38 and Figure 40 that the precipitation rate increases and desired pH is achieved in less time at temperature of 50^{o}C.

The pH decreased sharply and attained the desired pH faster at temperature of 50^{o}C than experiment at 25^{o}C with same operational variables, which is shown in Figure 36. Figure 37 shows that the pH 8 is achieved in less time at higher temperature (50^{o}C) than lower temperature (25^{o}C) with same operational variables.

12.2.2 Effect of impelling stirring

Rate of nucleation increases as the impeller agitation is increased, which is shown in Figure 42 and Figure 43. Increase in stirring rate of impeller promotes collision molecules with the neighboring molecules. Agitation have an impact on the time needed to achieve desired pH.

Table 12 shows the product yield obtained from experiments with different stirring rates (500 and 600 rpm), gas flow rates (0.3 and 0.5 L/min) and initial pH and final pH of the experiment.

It was calculated in section 8.4 that the stirring rates of 500 and 600 rpm are in turbulent-flow range so that no flooding of gas in the reactor for heterogeneous reactive crystallization of lithium carbonate. The increase of the stirring speed at constant gas flow rate increased the rate of absorption of gas (CO_2). Thus it accelerated gas liquid mass transfer due to enhanced interaction between CO_2 gas bubbles and active molecules.

Table 12. Product yield of precipitated lithium carbonate obtained from heterogeneous system with different parameters at 50^{o}C.

Impeller speed, rpm	Gas feeding rate, L/min	Residence time, min	$pH_{initial}$	pH_{final}	Precipitated lithium carbonate, %
600	0.3	23.5	9.18	8	78.39
500	0.3	29.33	9.66	8	74.43
600	0.5	16.07	9.35	8	73.14
500	0.5	21.23	9.44	8	71.57

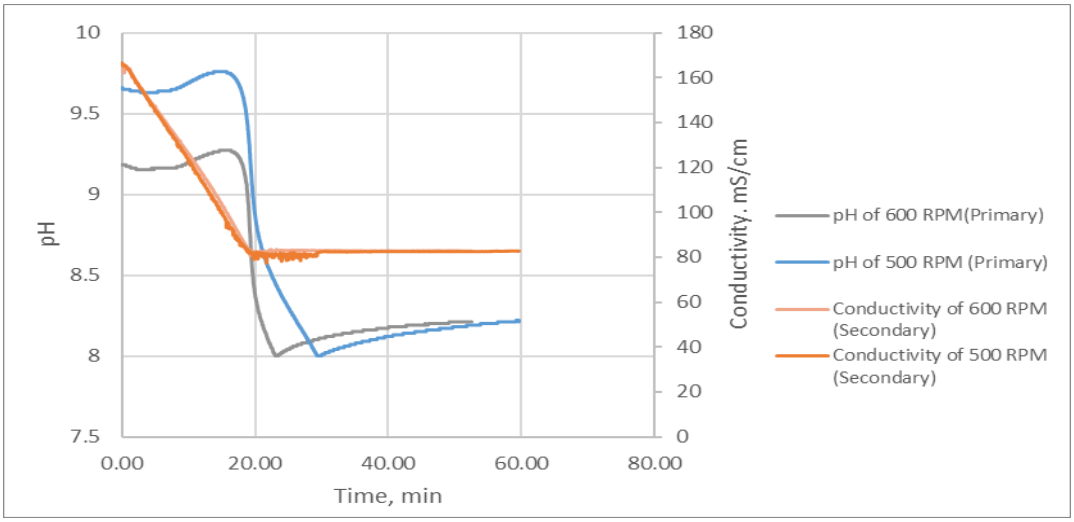

Figure 42. pH and conductivity curves for two different stirring speed (500 and 600 rpm) at temperature of 50°C, gas flow rate of 0.3 L/min and ageing of 30min.

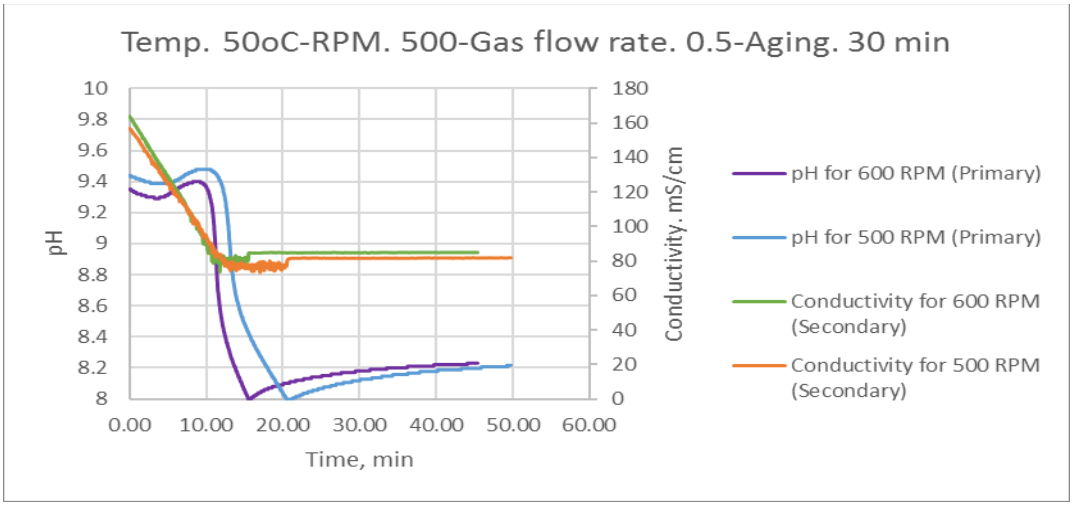

Figure 43. pH and Conductivity curves for two different stirring speed (500 and 600 rpm) at Temperature of 50°C, gas flow rate of 0.5 L/min and ageing of 30min.

At CO_2 flow rate of 0.3 L/min, Figure 44 shows the reduction in particle size of the crystals at higher stirring speed, which means smaller particles were formed at higher stirring speed. However, when the CO_2 flow rate was increased to 0.5 L/min, particle size distribution of lithium carbonate were almost the same at both stirring speeds, which is shown in Figure 45.

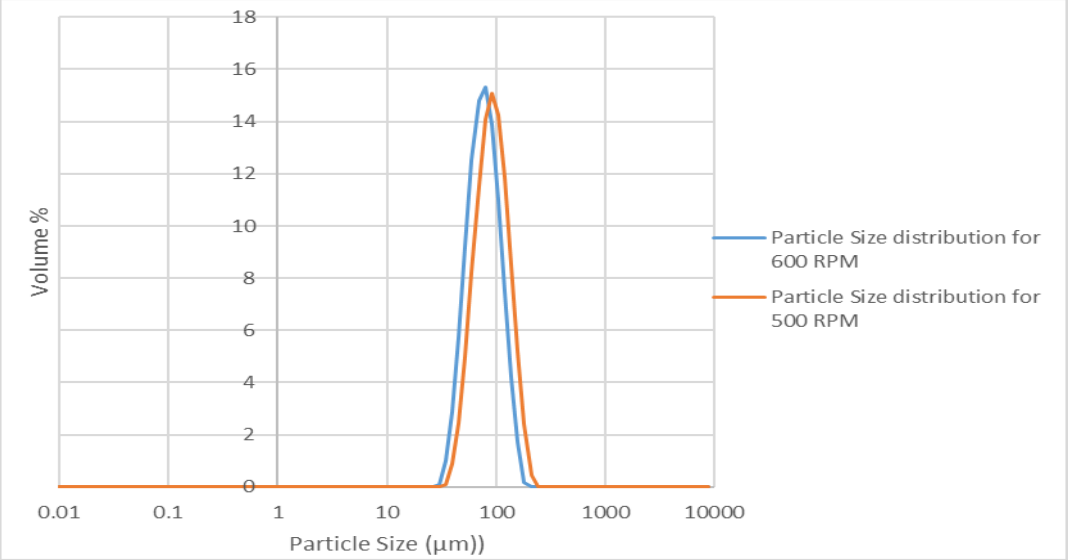

Figure 44. Particle size distribution of samples for two different stirring speed (500 and 600 rpm) at temperature of 50°C, gas flow rate of 0.3 LPM and ageing of 30min.

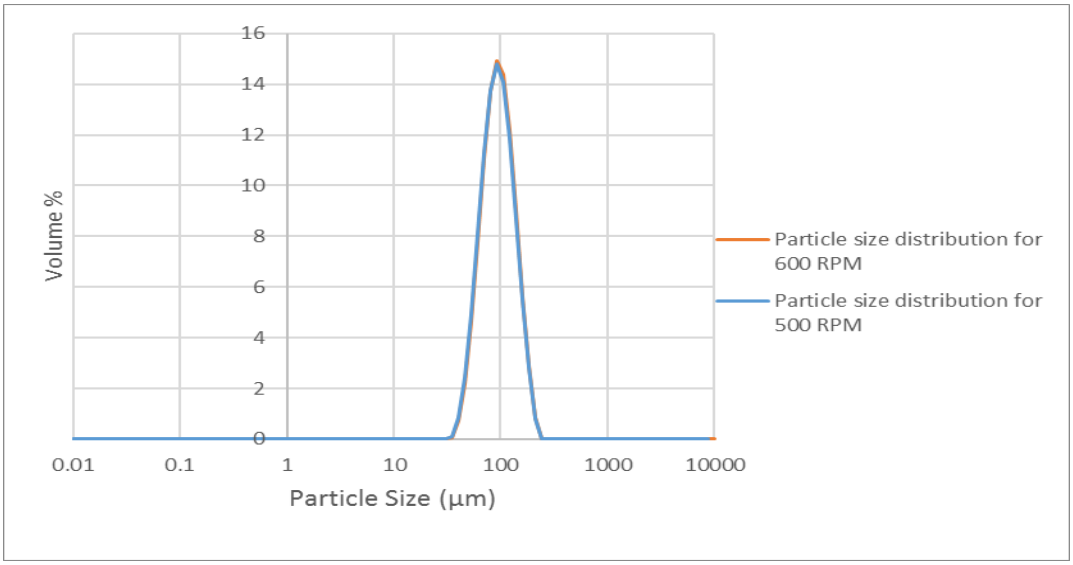

Figure 45. Particle size distribution of samples for two different stirring speed (500 and 600 rpm) at temperature of 50°C, gas flow rate of 0.5 LPM and ageing of 30min.

Figure 46 and Figure 47 show SEM images taken from the samples obtained by crystallization in heterogeneous system at 50°C with different impeller speeds for gas flow rate 0.3 L/min and 0.5 L/min, respectively. It can be seen that similar kind of morphology of flower shape crystals were obtained.

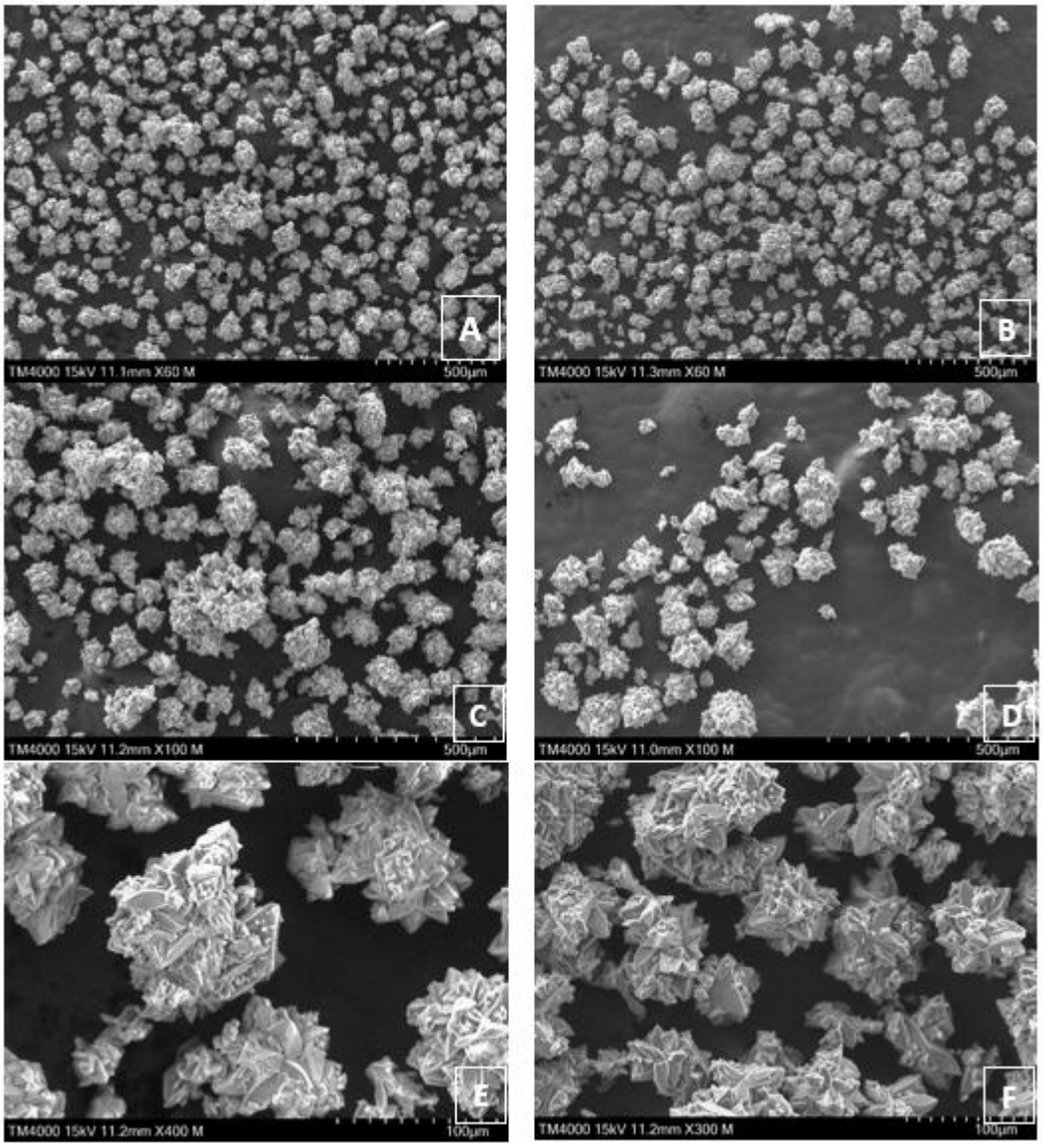

Figure 46. SEM images of samples obtained from stirring speed of 600 rpm (A, C and E) and 500 rpm (B, D and F) at constant temperature of 50ºC, gas flow rate of 0.3 L/min and ageing of 30min.

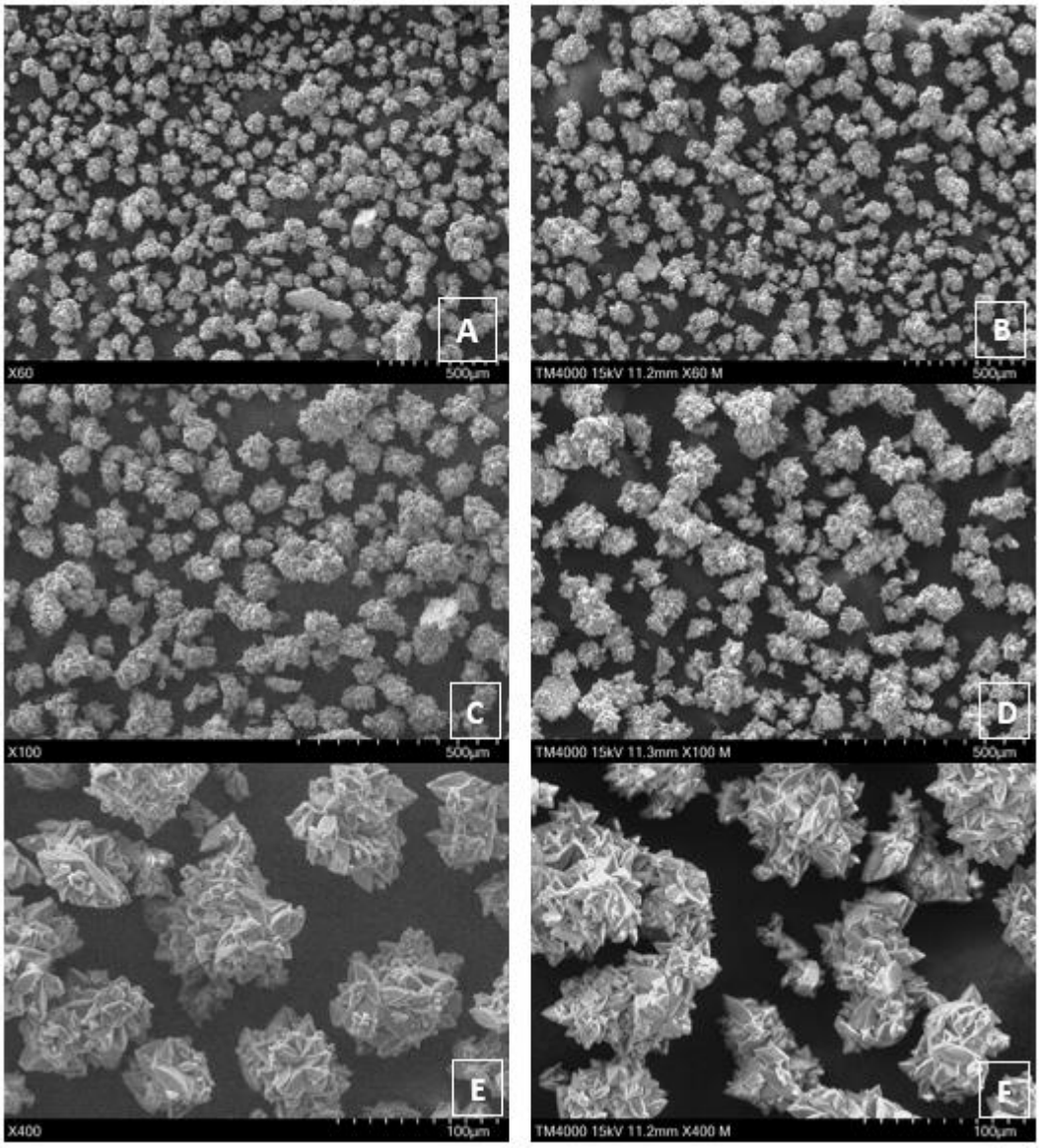

Figure 47. SEM images of samples obtained from stirring speed of 600 rpm (A, C and E) and 500 rpm (B, D and F) at constant temperature of 50ºC, gas flow rate of 0.5 L/min and ageing of 30min.

The crystals obtained from heterogeneous system was characterized by XRD. It can be seen in appendix I that the samples analyzed obtained at different operating parameters have the same XRD peaks.

The XRD data was compared with the reference pattern in MATCH program. It can be seen in Figure 48 that peaks of the sample obtained by crystallization is consistent with the reference pattern (ICSD 98-010-0324 C1 Li_2O_3).

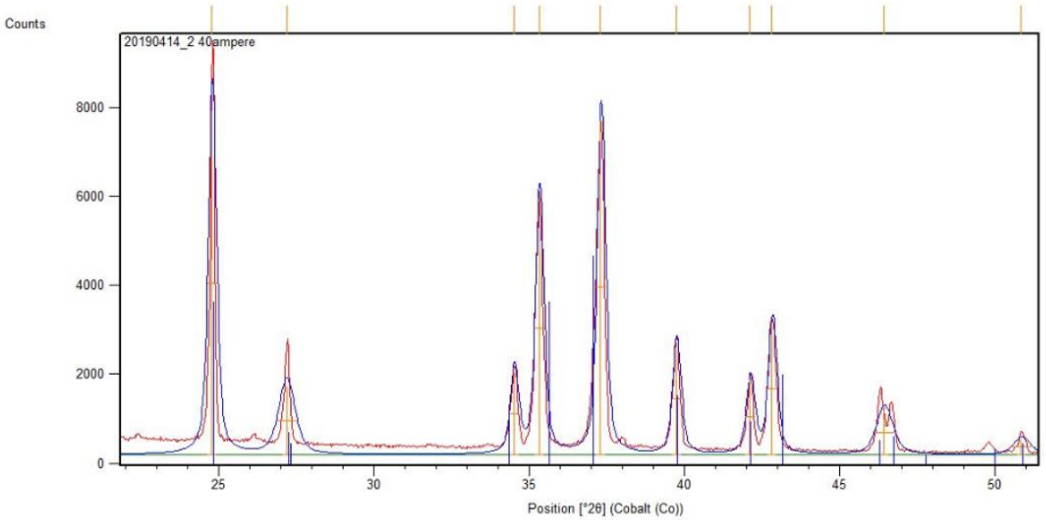

Figure 48. XRD analysis of samples obtained from stirring speed of 600 rpm and 500 rpm at constant temperature of 50°C, gas flow rate of 0.5 L/min and ageing of 30min.

For heterogeneous reactive crystallization at 25°C, similar results were obtained compare to the results obtained at 50°C, which are shown in Figure 49, Figure 50 and Table 13.

From pH measurements, it was found that all solutions before crystallization had a pH range between 10.87 and 11.27. The yield of the product was around 44%, which is shown in Table 13.

Table 13. Product yield of precipitated lithium carbonate obtained from heterogeneous system with different parameters at 25°C

Impeller speed, rpm	Gas feeding rate, L/min	Residence time, min	$pH_{initial}$	pH_{final}	Precipitated lithium carbonate, %
600	0.3	30.4	10.92	9	41.47
500	0.3	38.90	11.27	9	42.06
600	0.5	24.33	11.17	9	44.01
500	0.5	26.07	10.87	9	38.60

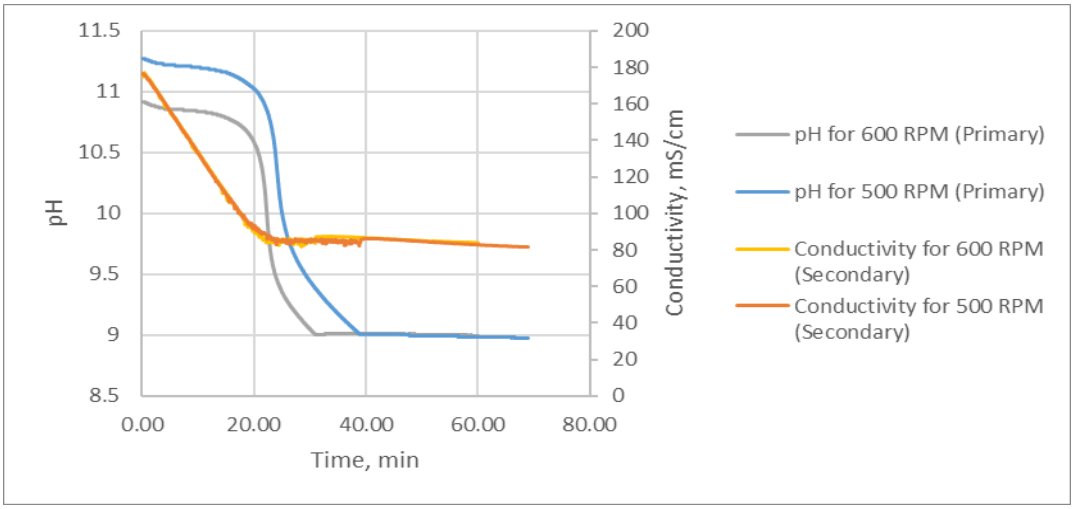

Figure 49. pH and conductivity curves for two different stirring speed (500 and 600 rpm) at temperature of 25ºC, gas flow rate of 0.3 L/min and ageing of 30min.

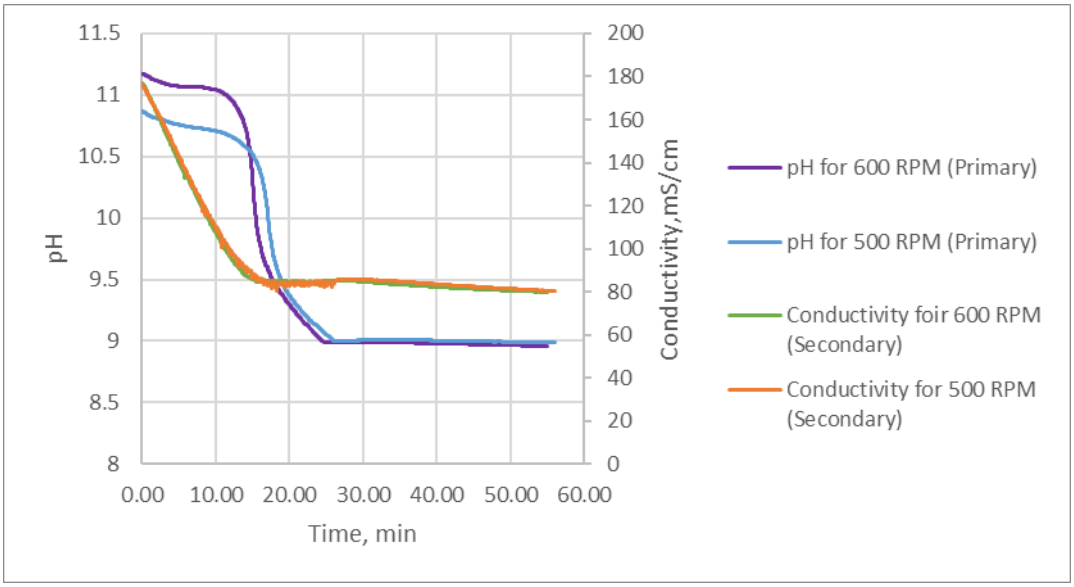

Figure 50. pH and conductivity curves for two different stirring speed (500 and 600 rpm) at temperature of 25ºC, gas flow rate of 0.5 L/min, ageing of 30min.

For heterogeneous reactive crystallization at 25ºC, similar results of crystal shape were obtained compare to the results obtained at 500 and 600 rpm, which are shown in Figure 51 and Figure 52. It can be seen that small particles are obtained at 600 rpm and particles obtained at 500rpm were agglomerates.

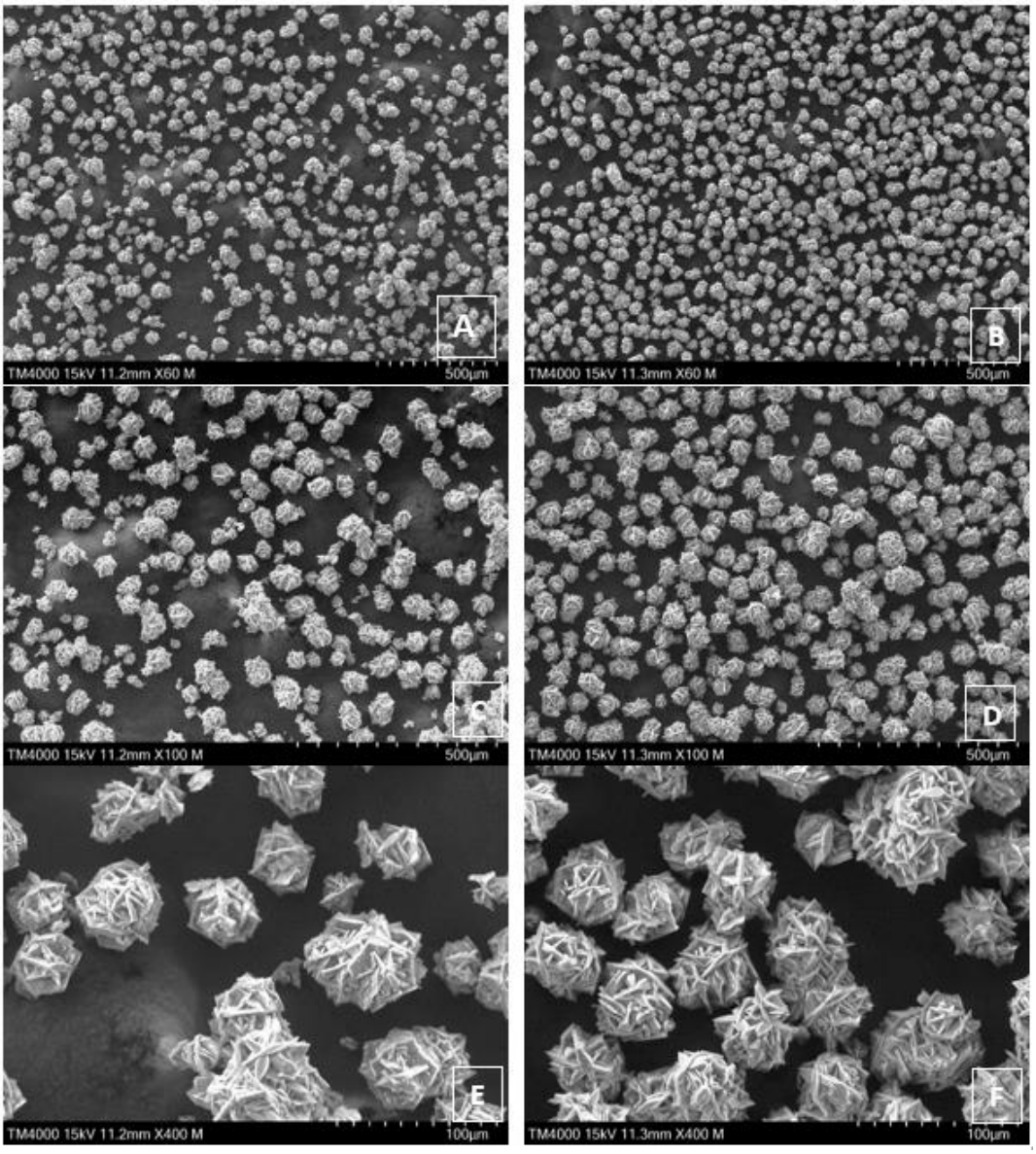

Figure 51. SEM images of samples obtained from stirring speed of 600 rpm (A, C and E) and 500 rpm (B, D and F) at constant temperature of 25ºC, gas flow rate of 0.3 L/min and ageing of 30min.

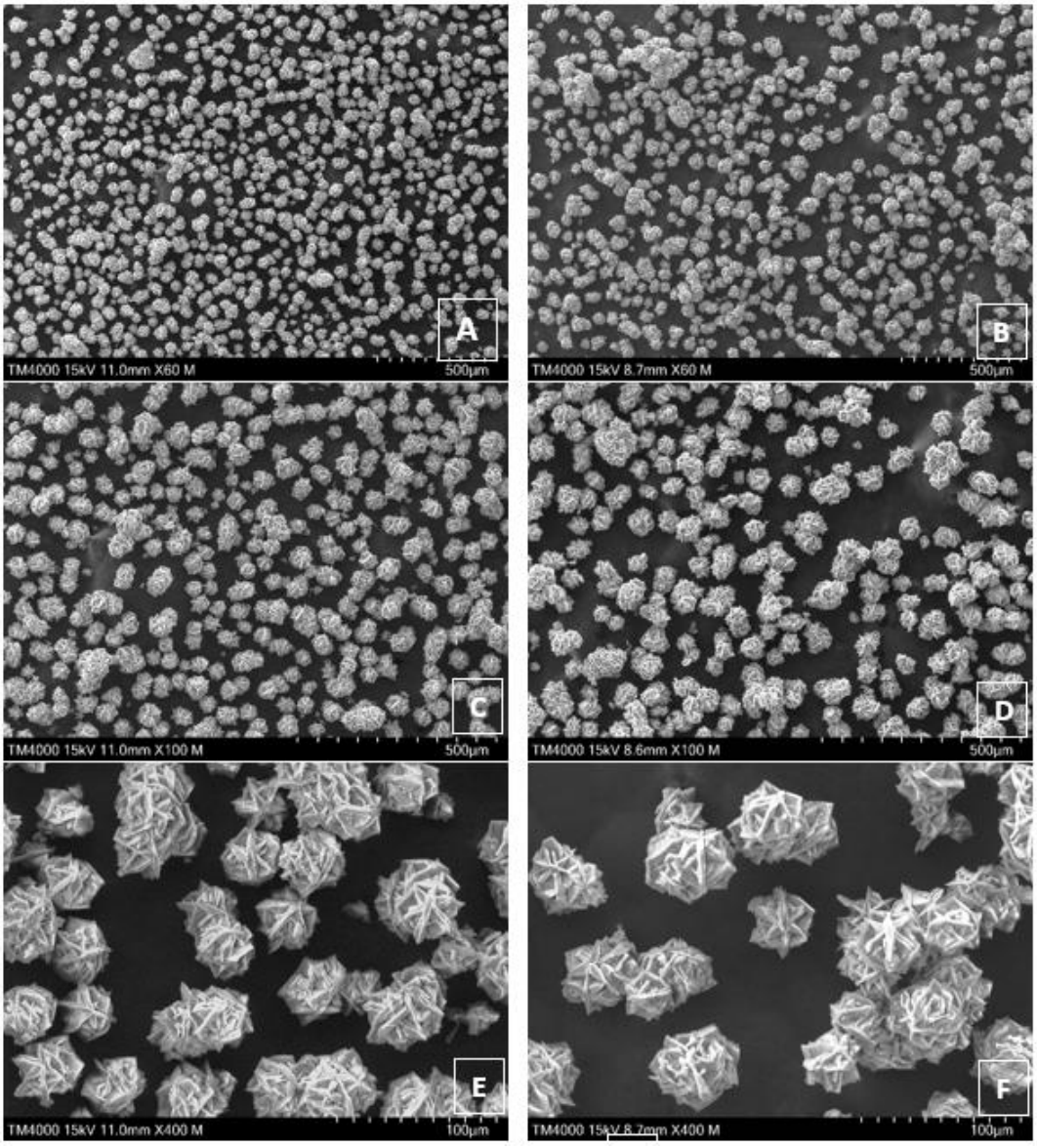

Figure 52. SEM images of samples obtained from stirring speed of 600 rpm (A, C and E) and 500 rpm (B, D and F) at constant temperature of 25ºC, gas flow rate of 0.5 L/min and ageing of 30min.

At CO_2 flow rate of 0.3 L/min, particle size distribution shown in Figure 53 indicates the reduction in particle size with higher stirring speed. However, when the CO_2 flow rate was increased to 0.5 LPM, particle size distributions of lithium carbonate at two stirring speeds were the same shown in Figure 54 and Figure 45.

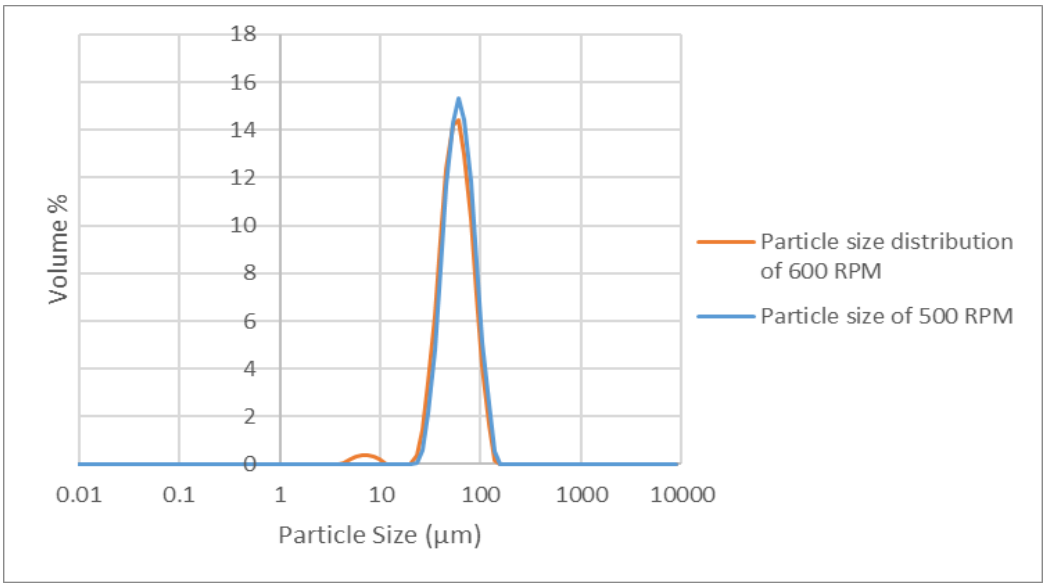

Figure 53. Particle size distribution of samples for two different stirring speed (500 and 600 rpm) at temperature of 25ºC, gas flow rate of 0.3 L/min and ageing of 30min.

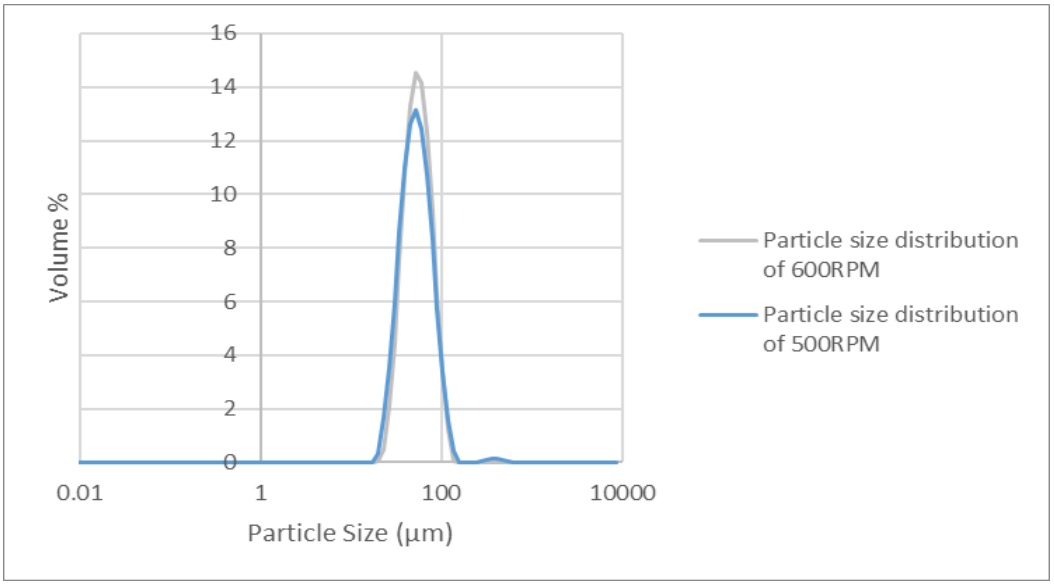

Figure 54. Particle size distribution of samples for two different stirring speed (500 and 600 rpm) at temperature of 25ºC, gas flow rate of 0.5 L/min and ageing of 30min.

12.2.3 Effect of gas feeding rate

Precipitation rate rises as the CO_2 gas flow rate is increased from 0.3 to 0.5 L/min at constant temperature and mixing condition. Time to reach the desired pH increases as the gas flow rate is decreased, which is shown in Figure 55-59. It can be seen from Table 14 and Table 15 that more crystals were obtained at lower gas flow rate for both the impeller speeds (500 and 600 rpm). At lower gas feeding, gas

bubbles was prevented to be in the reactor center and uniform mixture is obtained resulting in efficient mass transfer of CO_2 gas with active molecules.

For heterogeneous reactive crystallization at 50°C, similar flower-shape pellets were obtained compare to the results obtained at two different stirring speeds (500 and 600 rpm), which are shown in Figure 59 and Figure 60 .

Particle size distribution of precipitates obtain at different operational conditions are shown in Figure 63, Figure 64, Figure 65 and Figure 66. The results show that there is not any significant difference of PSD at different stirring speed.

Table 14. Product yield of precipitated lithium carbonate obtained at two different gas flow rates (0.3 and 0.5 L/min) from heterogeneous system with different parameters at temperature of 50°C.

Impeller speed, rpm	Gas feeding rate, L/min	Residence time, min	$pH_{initial}$	pH_{final}	Precipitated lithium carbonate, %
600	0.3	23.48	9.18	8	78.39
600	0.5	16.07	9.35	8	73.14
500	0.3	29.33	9.66	8	74.43
500	0.5	21.23	9.44	8	71.57

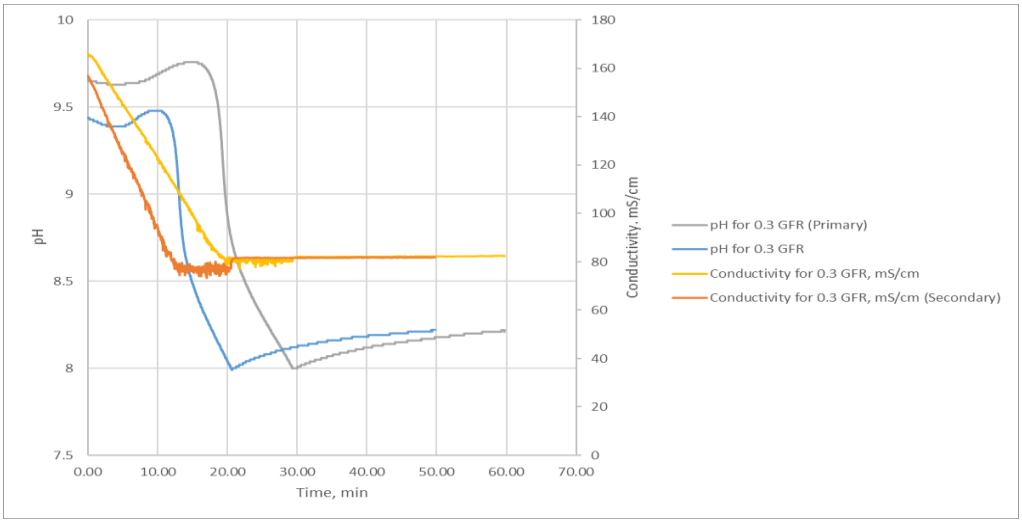

Figure 55. pH and conductivity curves for two different gas flow rates (0.3 and 0.5 L/min) at temperature of 50°C, impeller speed of 500 rpm, ageing of 30min.

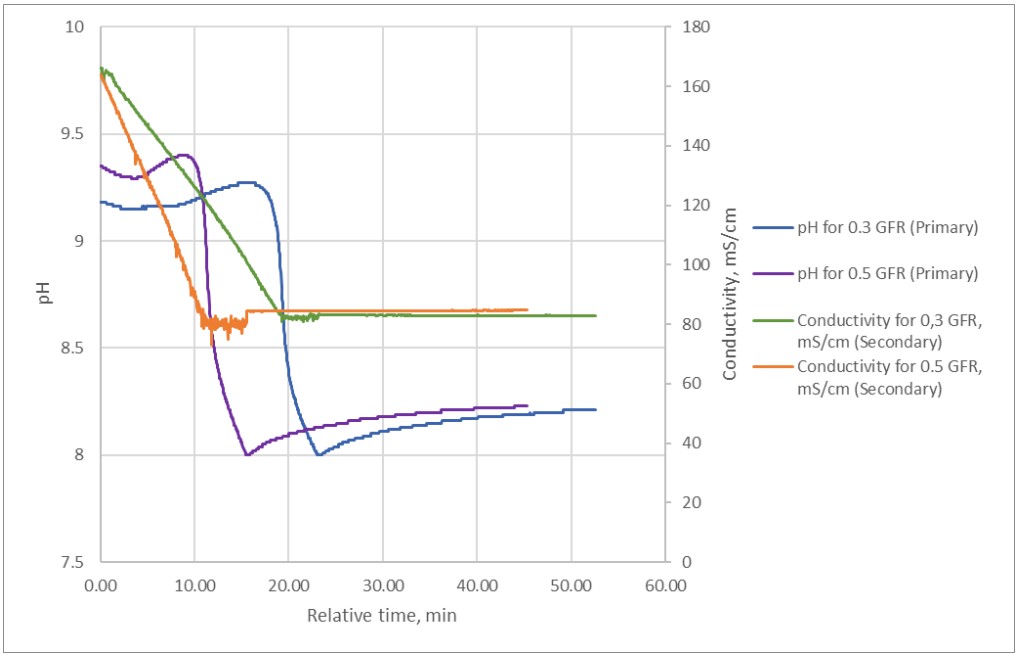

Figure 56. pH and conductivity curves for two different gas flow rates (0.3 and 0.5 L/min) at Temperature of 50°C, impeller speed of 600 rpm, ageing of 30min.

Table 15. Product yield of precipitated lithium carbonate obtained at two different gas flow rates (0.3 and 0.5 L/min) from heterogeneous system with different parameters at temperature of 25°C.

Impeller speed, rpm	Gas feeding rate, L/min	Residence time, min	$pH_{initial}$	pH_{final}	Precipitated lithium carbonate, %
600	0.3	30.43	10.92	9	41.47
600	0.5	24.33	11.17	9	44.01
500	0.3	38.90	11.27	9	42.06
500	0.5	26.07	10.87	9	38.60

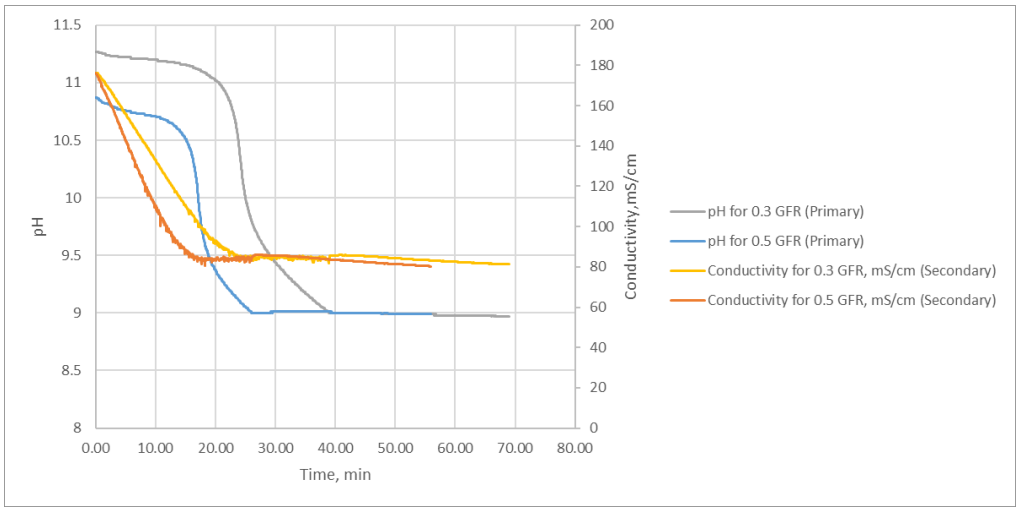

Figure 57. pH and conductivity curves for two different gas flow rates (0.3 and 0.5 L/min) at temperature of 25ºC, impeller speed of 500 rpm and ageing of 30min.

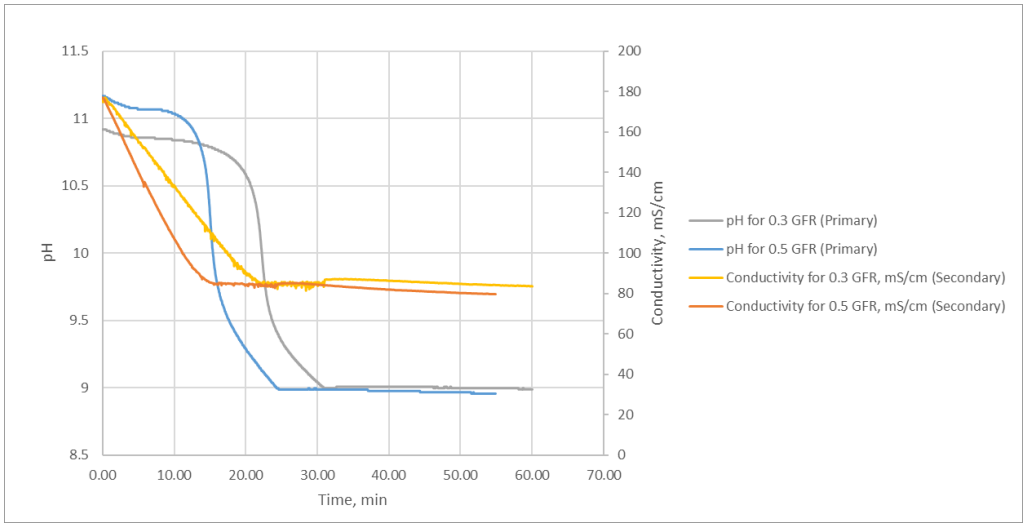

Figure 58. pH and conductivity curves for two different gas flow rates (0.3 and 0.5 L/min) at temperature of 25ºC, impeller speed of 600 rpm and ageing of 30min.

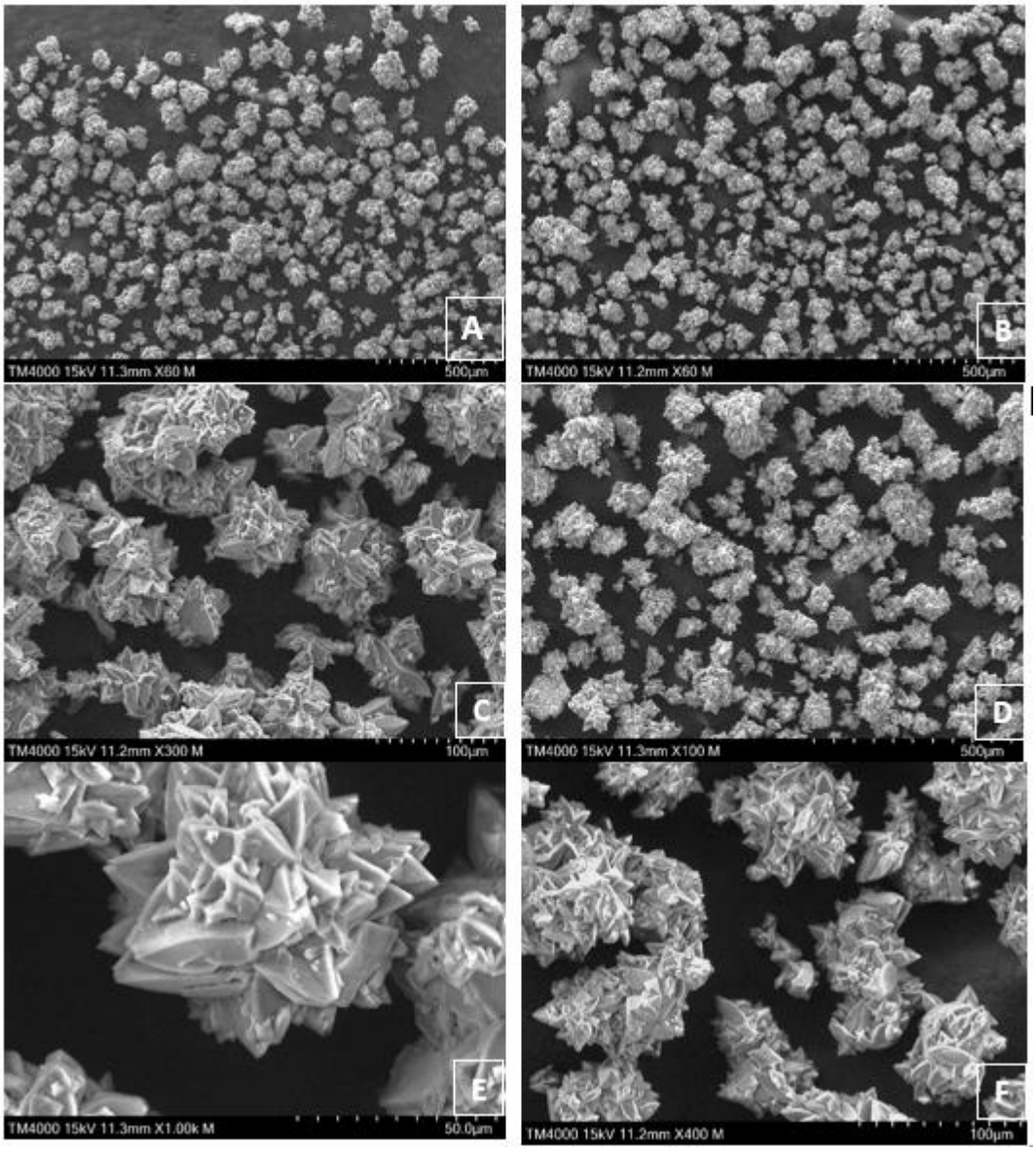

Figure 59. SEM images of samples obtained from gas flow rate of 0.3 L/min (A, C and E) and gas flow rate of 0.5 L/min (B, D and F) at constant temperature of 50ºC, impeller speed of 500 rpm and ageing of 30min.

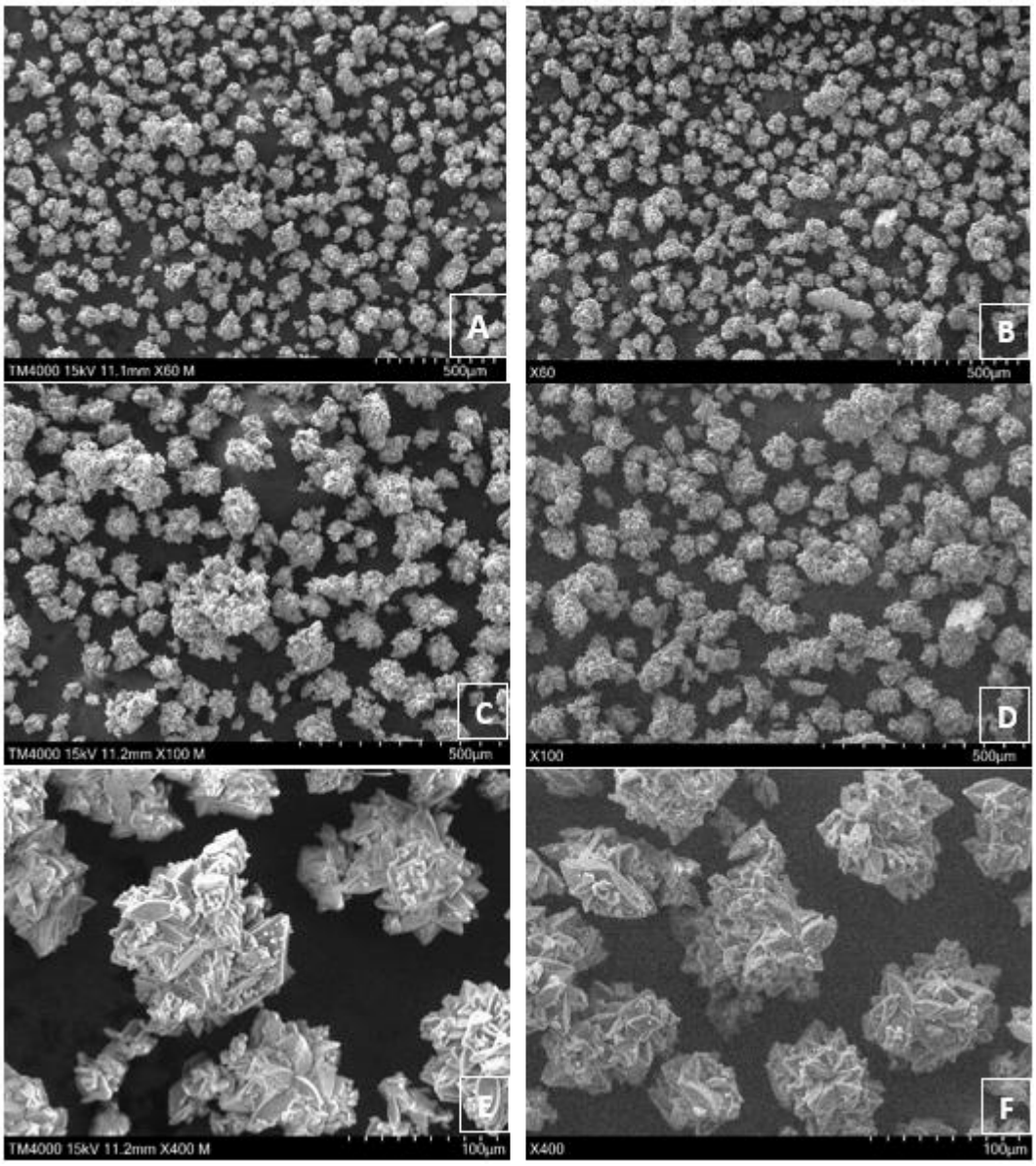

Figure 60. SEM images of samples obtained from gas flow rate of 0.3 L/min (A, C and E) and gas flow rate of 0.5 L/min (B, D and F) at constant temperature of 50^{o}C, impeller speed of 600 rpm and ageing of 30min.

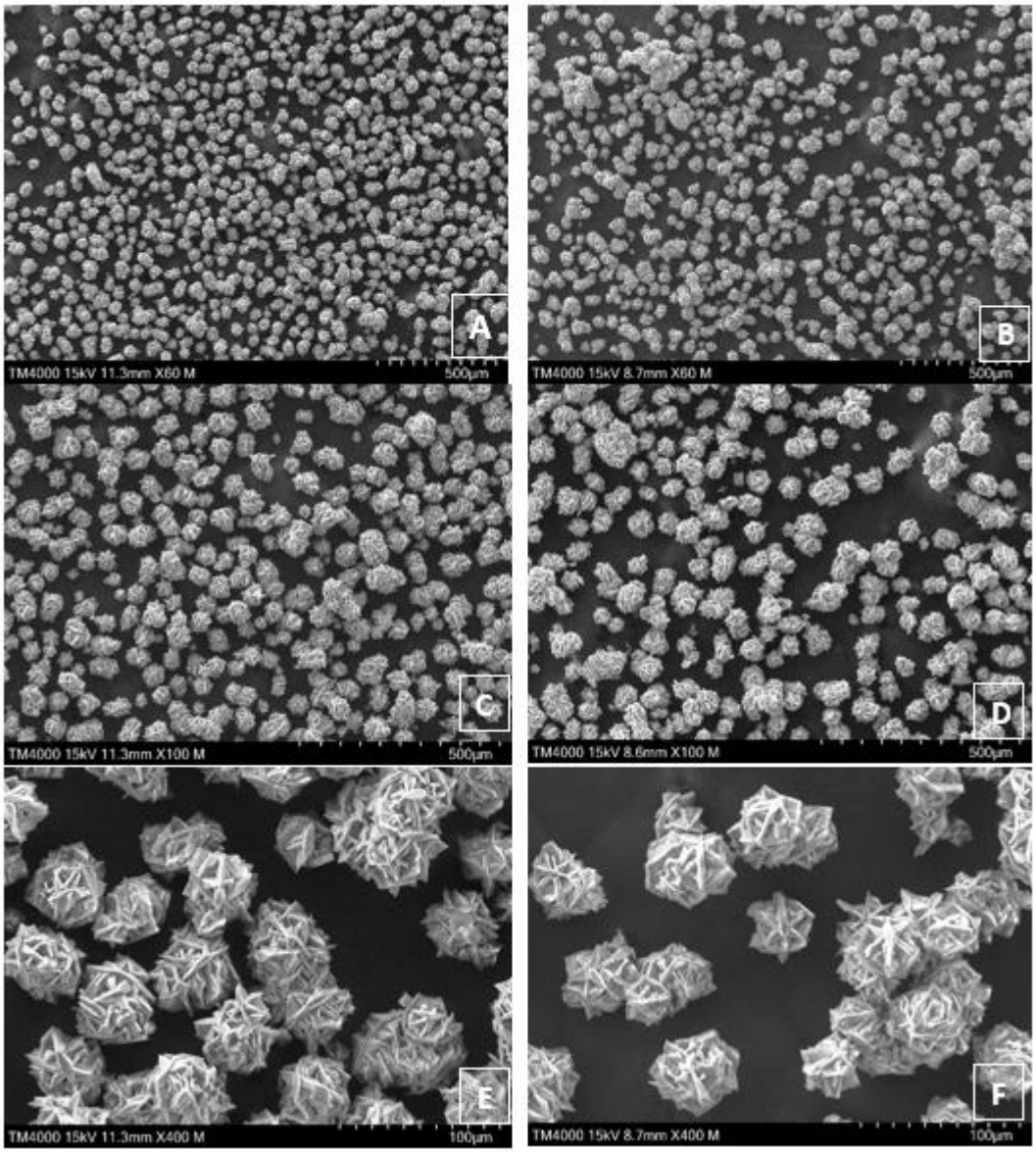

Figure 61. SEM images of samples obtained from gas flow rate of 0.3 L/min (A, C and E) and gas flow rate of 0.5 L/min (B, D and F) at constant temperature of 25ºC, impeller speed of 500 rpm and ageing of 30min.

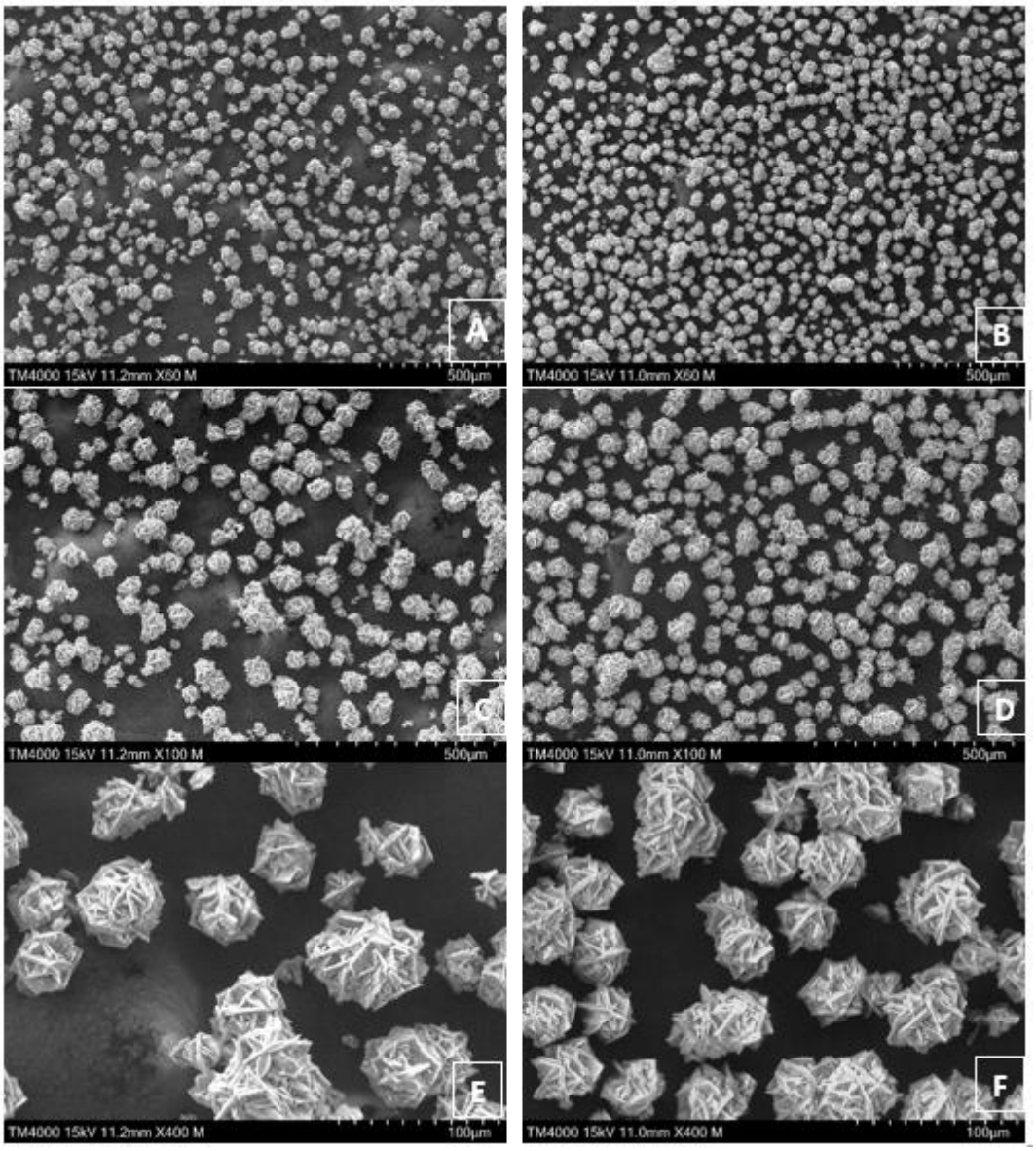

Figure 62. SEM images of samples obtained from gas flow rate of 0.3 L/min (A, C and E) and gas flow rate of 0.5 L/min (B, D and F) at constant temperature of 25^{o}C, impeller speed of 600 rpm and ageing of 30min.

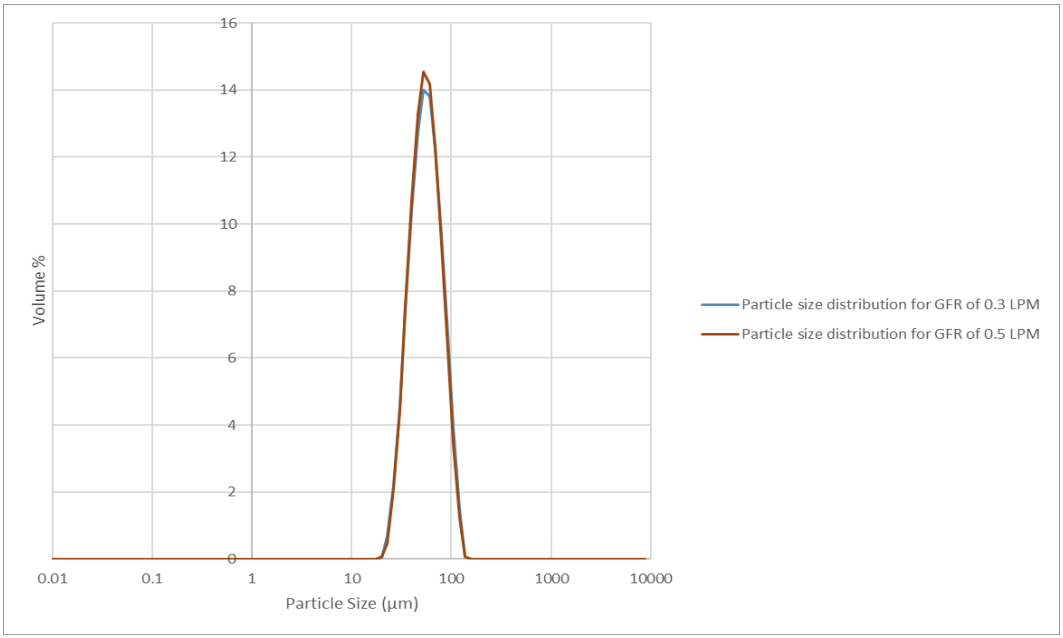

Figure 63. Particle size distribution of samples for two different gas flow rates (0.3 L/min and 0.5 L/min) at temperature of 25°C, impeller speed of 600 rpm and ageing of 30min.

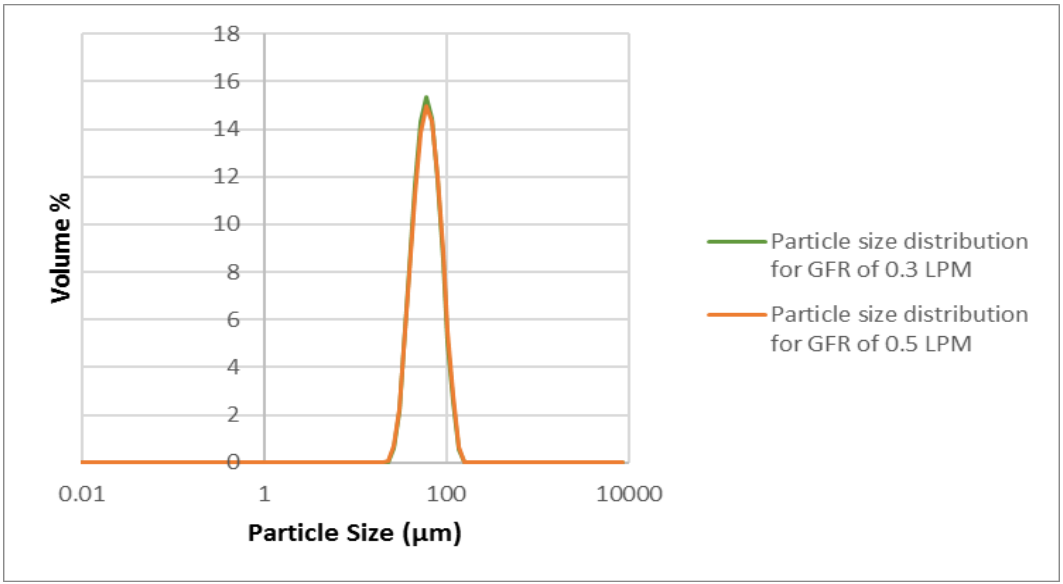

Figure 64. Particle size distribution of samples for two different gas flow rates (0.3 L/min and 0.5 L/min) at temperature of 25°C, impeller speed of 500 rpm and ageing of 30min.

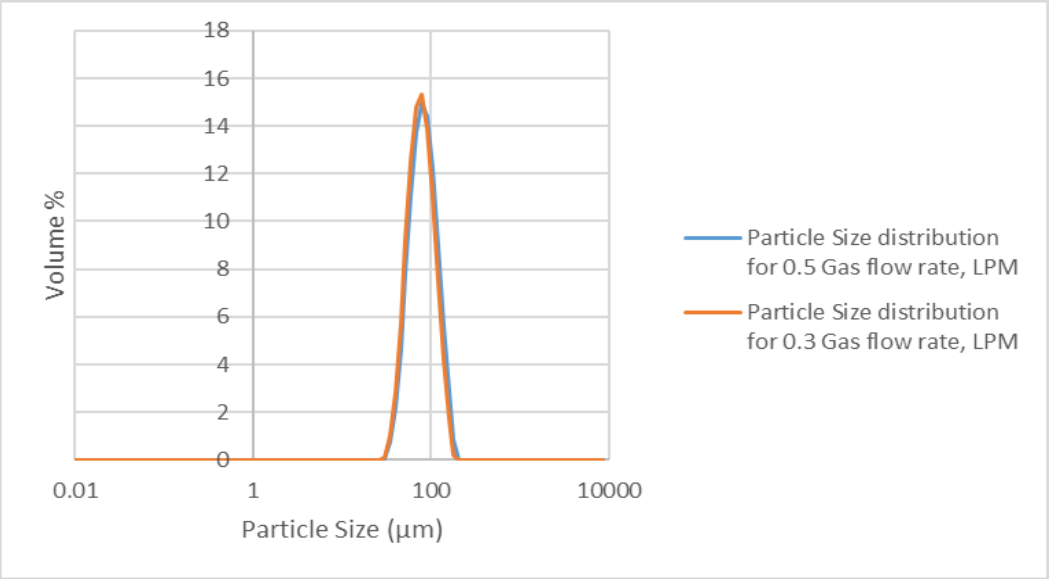

Figure 65. Particle size distribution of samples for two different gas flow rates (0.3 L/min and 0.5 L/min) at temperature of 50°C, impeller speed of 600 rpm and ageing of 30min.

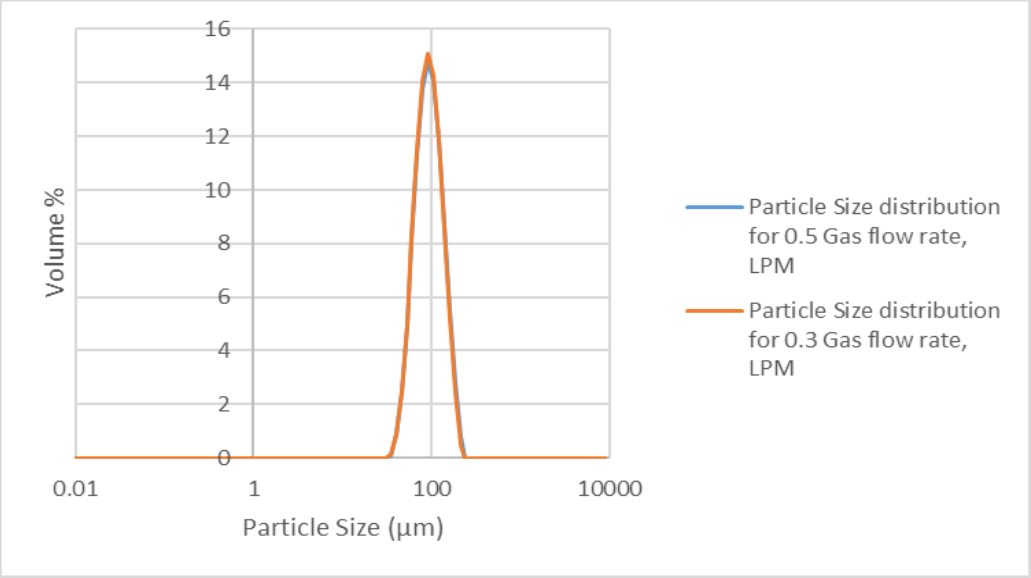

Figure 66. Particle size distribution of samples for two different gas flow rates (0.3 L/min and 0.5 L/min) at temperature of 50°C, impeller speed of 500 rpm and ageing of 30min.

12.3 Homogeneous reactive crystallization of lithium carbonate

12.3.1 Effect of pump flow rate

Nucleation is accelerated with the increase of feed rate since the reaction is enhanced. It can be seen in the Figure 67 and Figure 68 that the pump flow rate have an impact on the rate of nucleation and on the time needed to achieve equilibrium.

Table 16 shows the product yield obtained from experiments with different stirring rates (500 and 600 rpm), Na_2CO_3 pump flow rate (2.54 and 4.42 mL/min), $pH_{initial}$, and pH_{final} of the experiment at 50°C.

Figure 69 and Figure 70 show SEM images taken of the samples obtained by homogeneous reactive crystallization at 50°C, two Na_2CO_3 pump flow rates and ageing of 30min for impeller speed of 500 and 600 rpm, respectively.

Similar results were obtained as the results obtained from effects of gas flow rate in heterogeneous reactive crystallization. It can be seen that in each case similar kind of morphology of flower shape crystal is obtained. Particle size distribution can be seen in Figure 71 and Figure 72. It indicates that same particle size distribution were obtained for different impeller speed at constant Na_2CO_3 pump flow rate and 50°C.

Table 16. Product yield of precipitated lithium carbonate obtained from homogeneous system with different parameters at 50°C.

Impeller speed, rpm	Pump flow rate, mL/min	Residence time, min	$pH_{initial}$	pH_{final}	Precipitated lithium carbonate, %
500	2.54	43.37	9.17	9.76	72.25
500	4.42	23.70	9.03	9.65	74.19
600	2.54	46.67	8.96	9.6	72.00
600	4.42	28.28	8.22	9.64	73.79

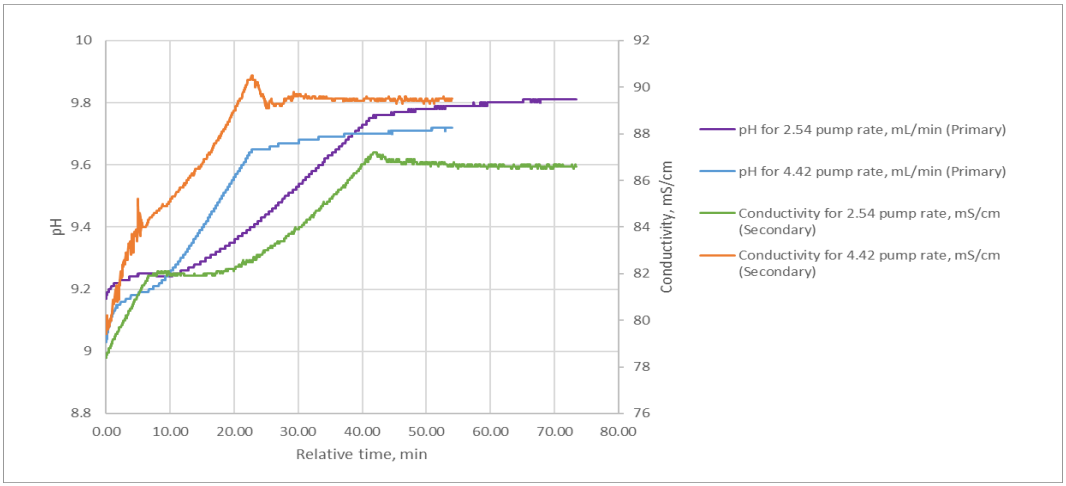

Figure 67. pH and conductivity curves for two different Na_2CO_3 pump flow rates (2.54 and 4.42 mL/min) at temperature of 50ºC, impeller speed of 500 rpm and ageing of 30min.

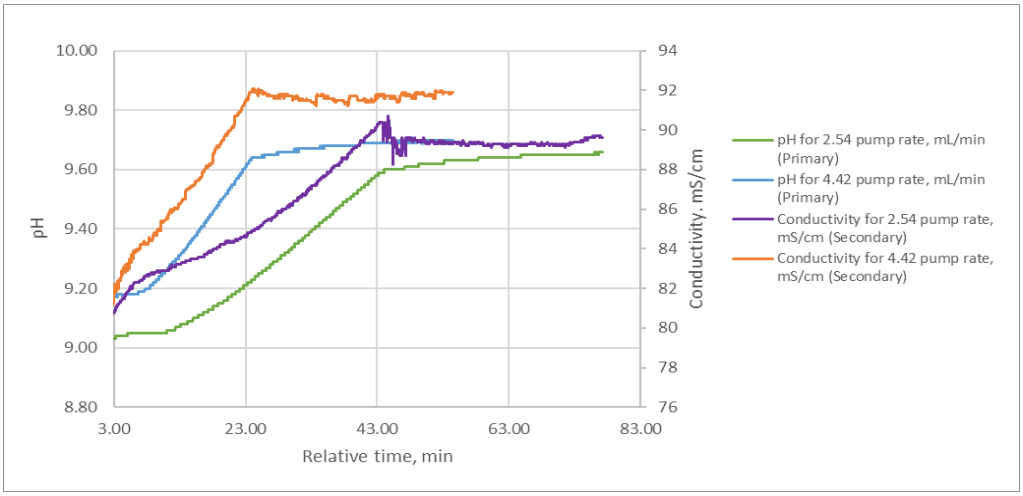

Figure 68. pH and conductivity curves for two different Na_2CO_3 pump flow rates (2.54 and 4.42 mL/min) at temperature of 50ºC, impeller speed of 600 rpm and ageing of 30min.

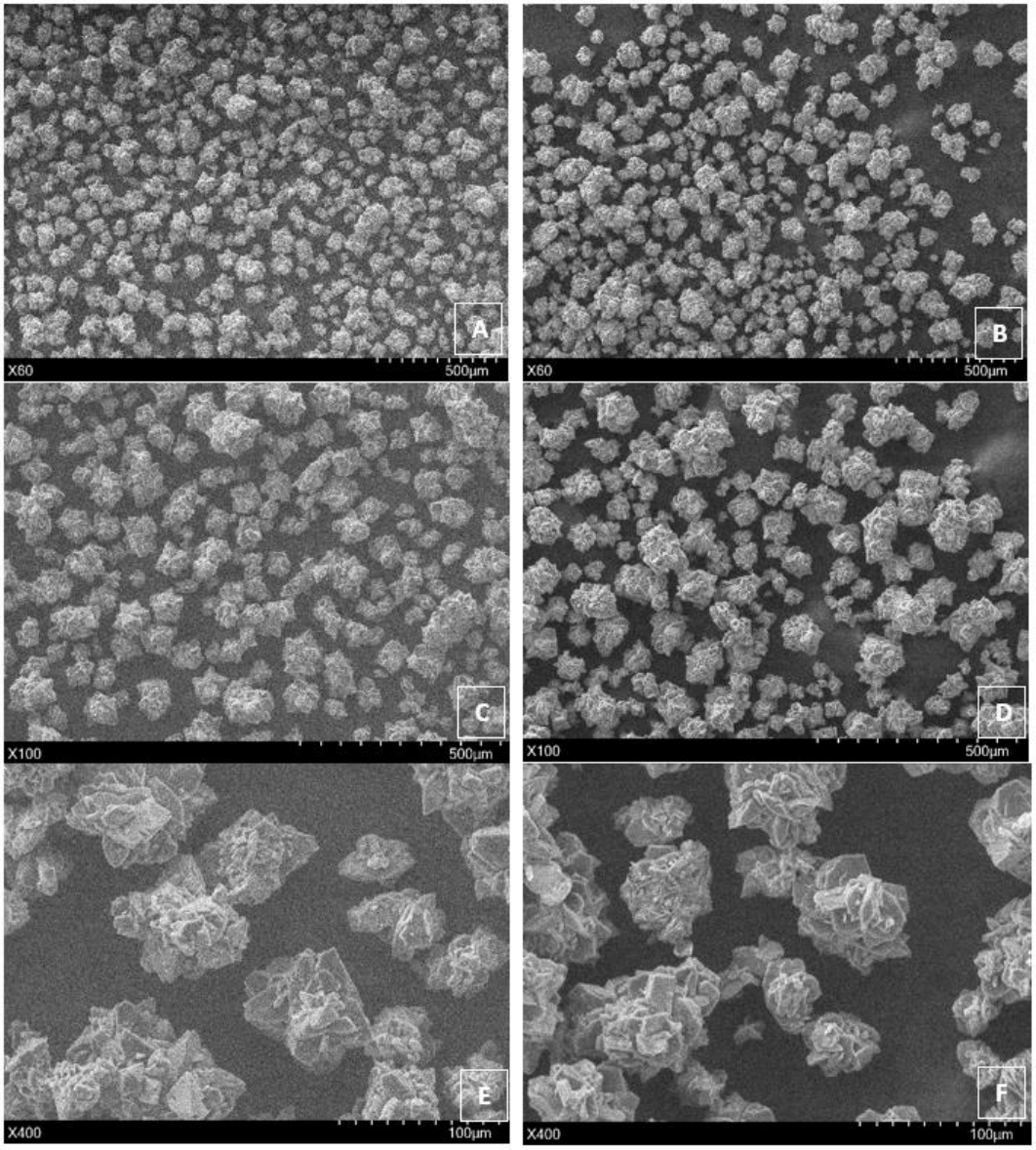

Figure 69. SEM images of samples obtained from Na_2CO_3 pump flow rate of 2.54 mL/min (A, C and E) and Na_2CO_3 pump flow rate of 4.42 mL/min (B, D and F) at constant temperature of 50^oC, impeller speed of 500 rpm and ageing of 30min.

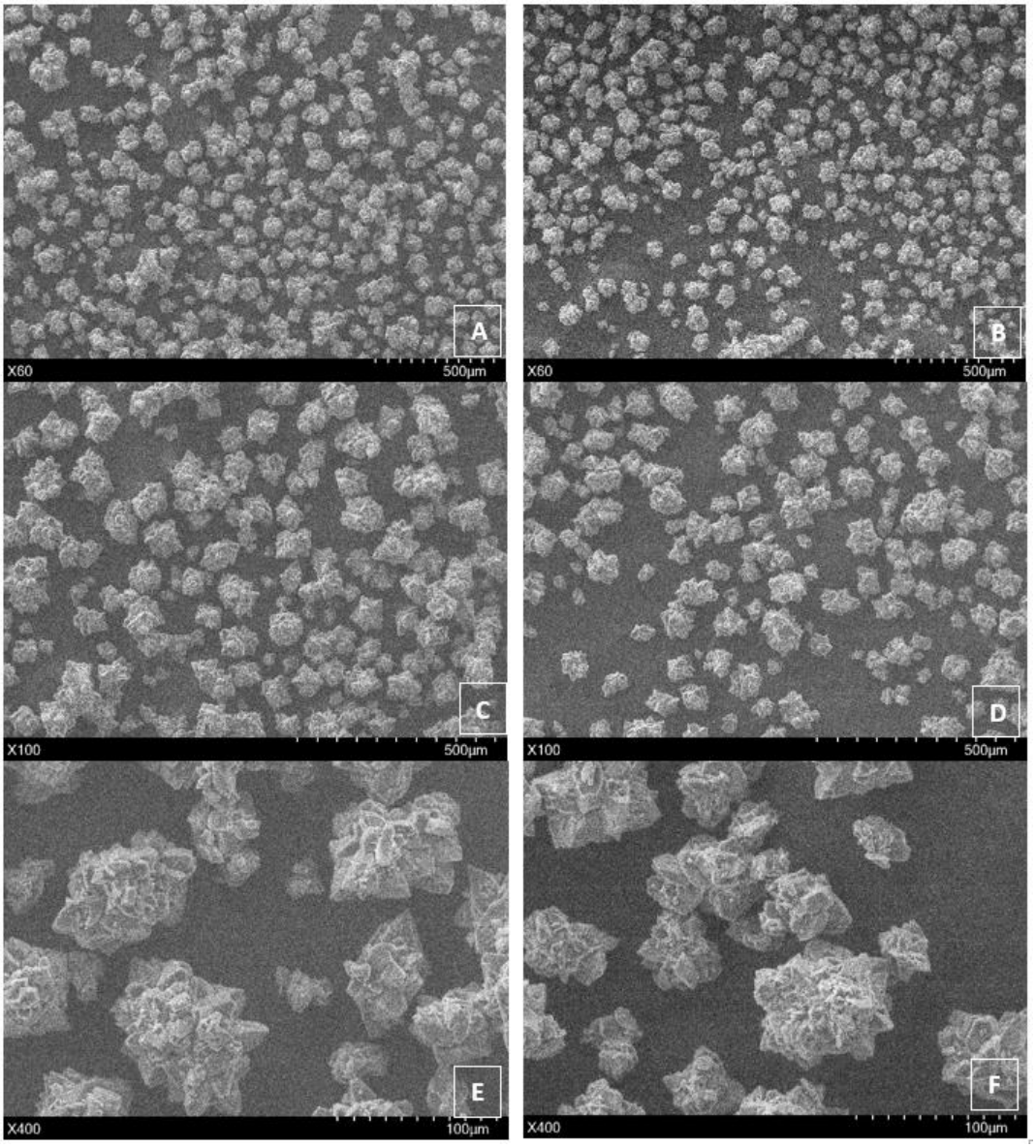

Figure 70. SEM images of samples obtained from Na_2CO_3 pump flow rate of 2.54 mL/min (A, C and E) and Na_2CO_3 pump flow rate of 4.42 mL/min (B, D and F) at constant temperature of 50^oC, impeller speed of 600 rpm and ageing of 30min.

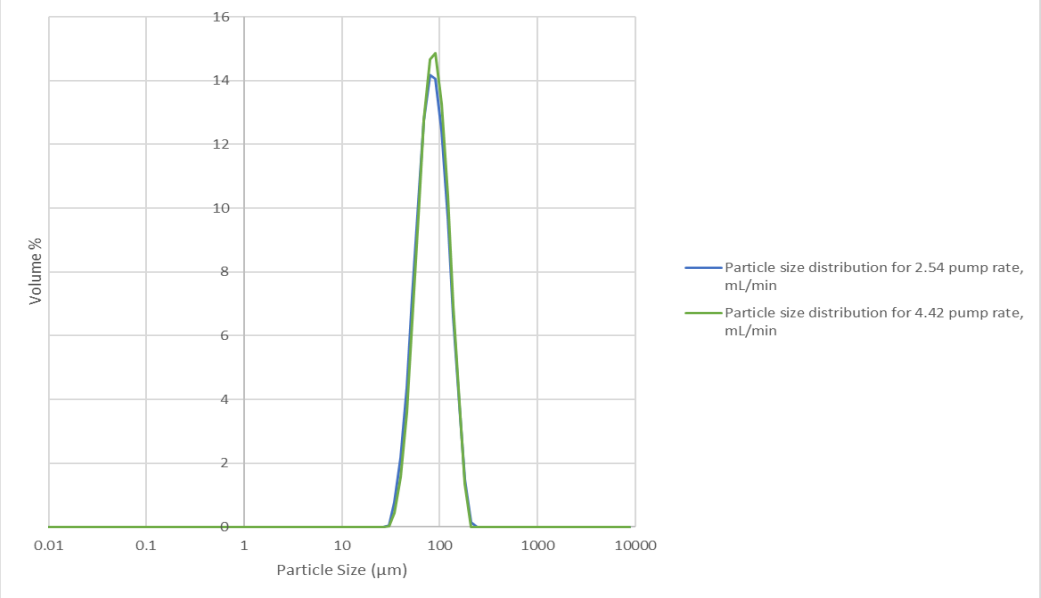

Figure 71. Particle size distribution of samples for two different Na_2CO_3 pump flow rates (2.54 L/min and 4.42 L/min) at temperature of 50ºC, impeller speed of 500 rpm and ageing of 30min.

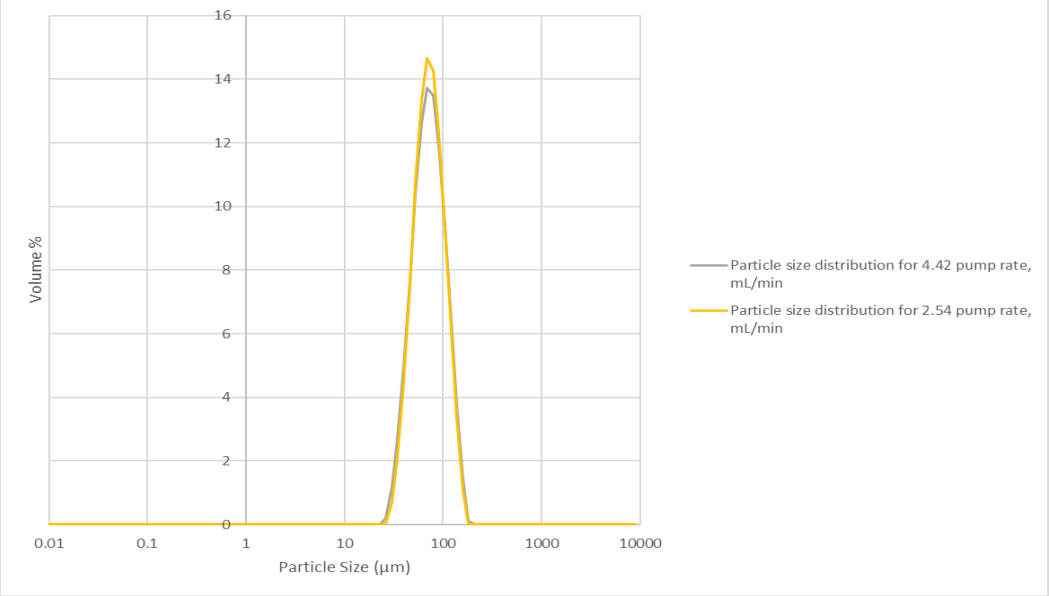

Figure 72. Particle size distribution of samples for two different Na_2CO_3 pump flow rates (2.54 L/min and 4.42 L/min) at temperature of 50ºC, impeller speed of 600 rpm and ageing of 30min.

12.3.2 Effect of impeller speed

There is no significant effect on the precipitation as the impeller speed is increased from 500 to 600 rpm at constant temperature and feeding rate. Time to reach the desired pH remains the same for two mixing rates. Figure 73 and Figure 74 show that the trends of pH and conductivity obtained were similar at two different impeller

speed (500 and 600 rpm). It can be seen in Table 17 that there was no significant change on the amount of crystals obtained at two different impeller speeds (500 and 600 rpm).

Figure 75 and Figure 76 show SEM images taken of the samples obtained by homogeneous reactive crystallization at 50^{o}C, two Na_2CO_3 pump flow rates and ageing of 30min for impeller speed of 500 and 600 rpm, respectively. Similar results were obtained as the results obtained from effects of gas flow rate in heterogeneous reactive crystallization. It can be seen that in each case similar kind of morphology of flower shape crystal is obtained.

Figure 77 and Figure 78 show that smaller particles were obtained at higher impeller speed at constant temperature and feeding rate, which is consistent with the findings obtained from the literature (Han et al. 2018).

In fact, all the XRD results were same and consistent with the reference patterns (ICSD 98-010-0324 C1 Li_2O_3), which is shown in Figure 79.

Table 17. Product yield of precipitated lithium carbonate obtained from homogeneous system with different parameters at 50^{o}C.

Impeller speed, rpm	Pump flow rate, mL/min	Residence time, min	$pH_{initial}$	pH_{final}	Precipitated lithium carbonate, %
500	2.54	43.37	9.17	9.76	72.25
600	2.54	46.67	8.96	9.6	72.00
500	4.42	23.70	9.03	9.65	74.19
600	4.42	28.28	8.22	9.64	73.79

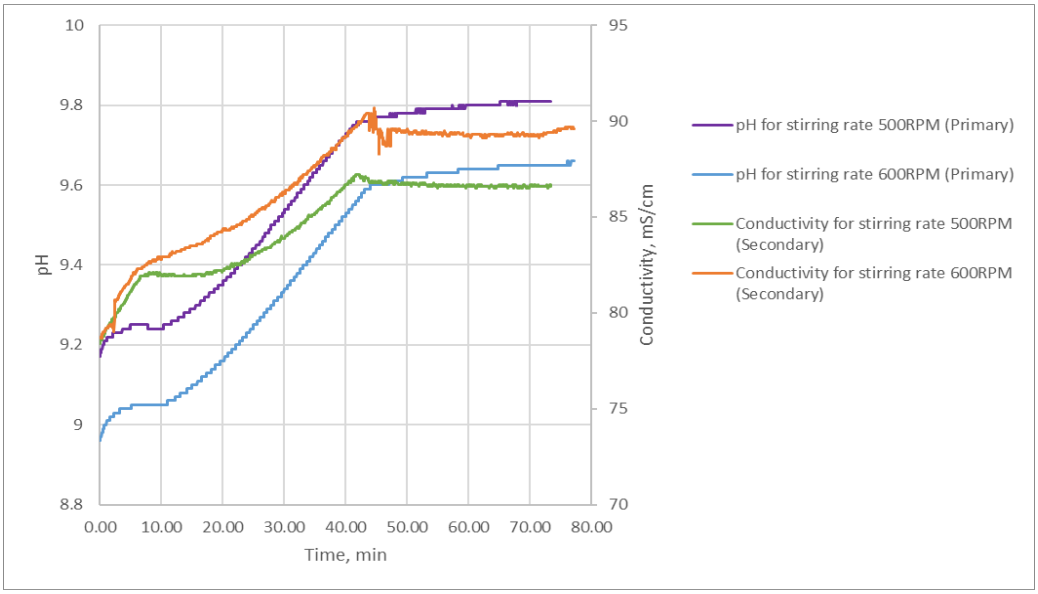

Figure 73. pH and conductivity curves for two different impeller speeds (500 and 500 rpm) at temperature of 50°C, Na_2CO_3 Pump flow rate of 2.54 mL/min and ageing of 30min.

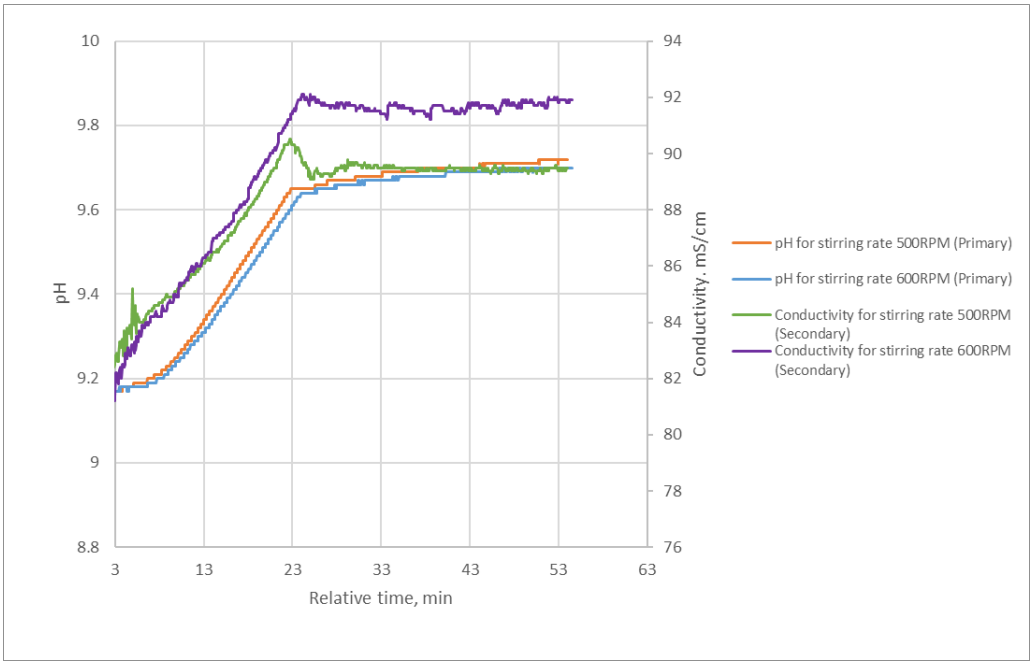

Figure 74. pH and conductivity curves for two different impeller speeds (500 and 500 rpm) at temperature of 50°C, Na_2CO_3 Pump flow rate of 4.42 mL/min and ageing of 30min.

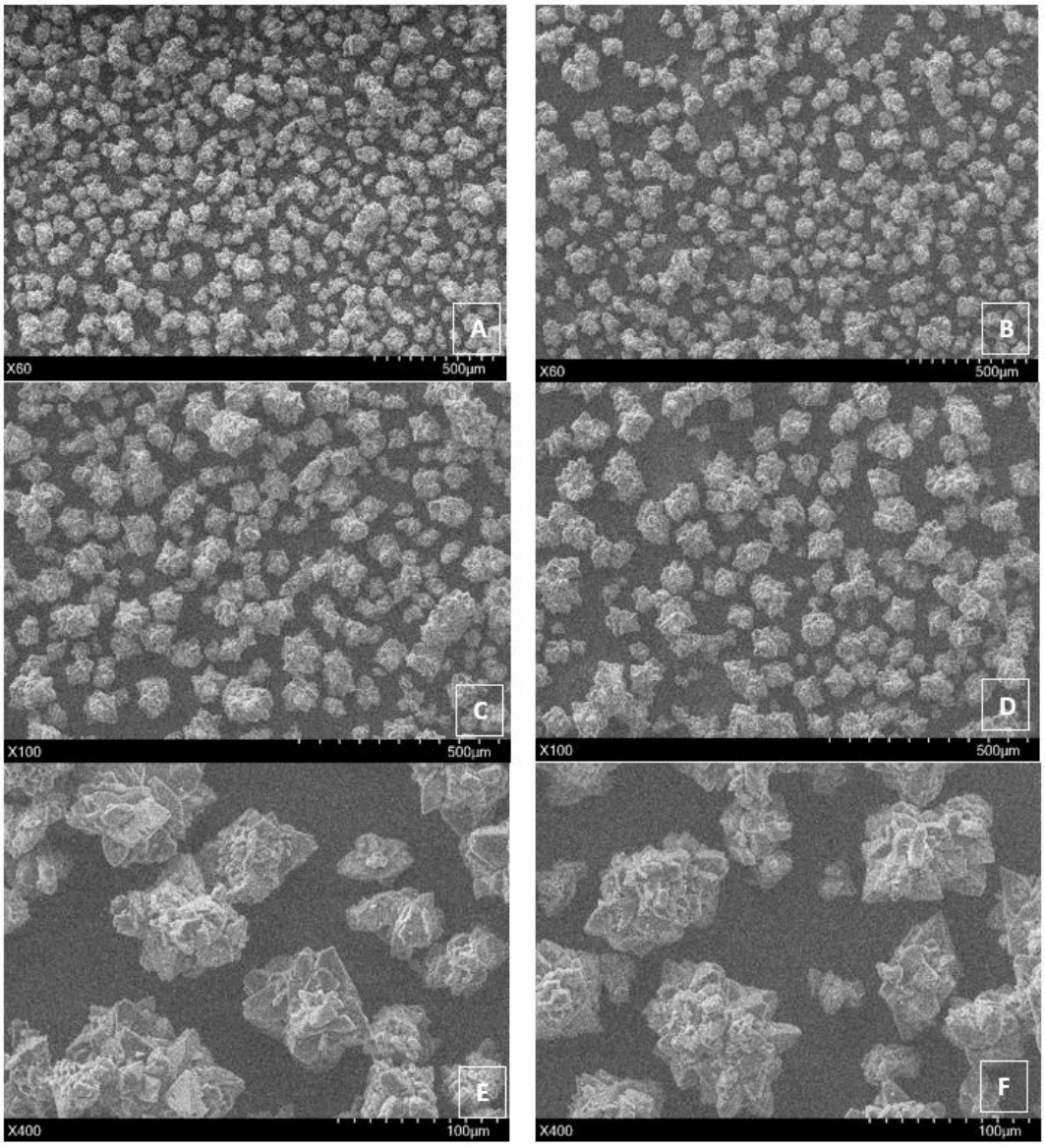

Figure 75. SEM images of samples obtained from impeller speed of 500 rpm (A, C and E) and impeller speed of 600 rpm (B, D and F) at constant temperature of 50ºC, Na_2CO_3 pump flow rate of 2.54 mL/min and ageing of 30min.

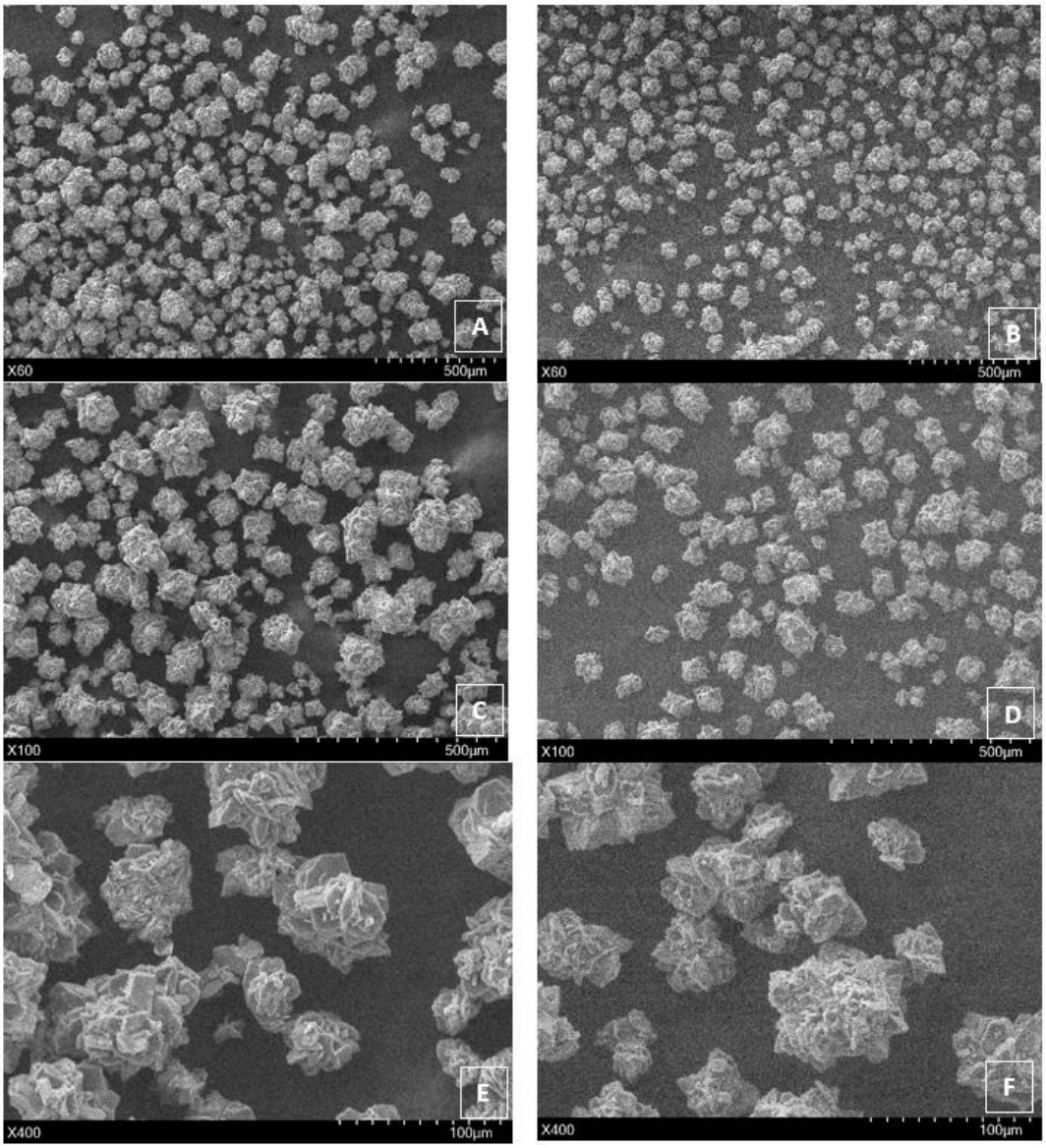

Figure 76. SEM images of samples obtained from impeller speed of 500 rpm (A, C and E) and impeller speed of 600 rpm (B, D and F) at constant temperature of 50ºC, Na_2CO_3 pump flow rate of 4.42 mL/min and ageing of 30min.

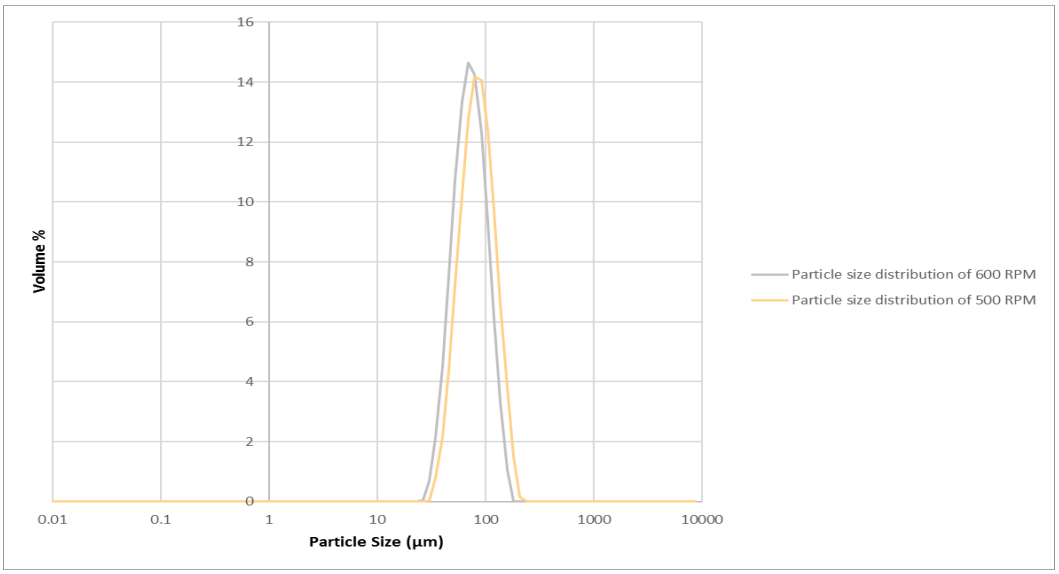

Figure 77. Particle size distribution of samples for impeller speeds (500 rpm and 600 rpm) at temperature of 50°C, Na_2CO_3 pump flow rate of 2.54 mL/min and ageing of 30min.

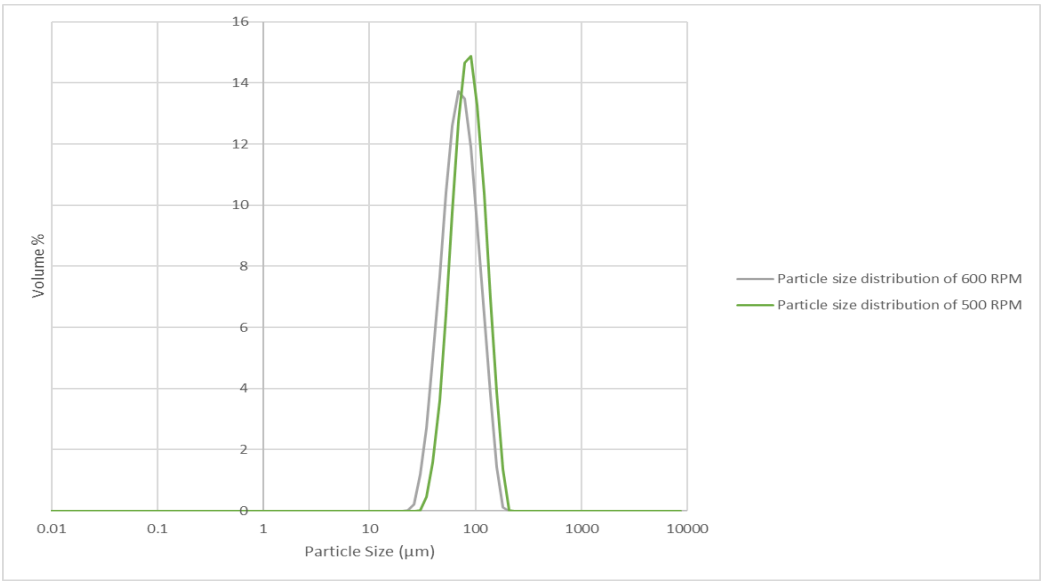

Figure 78. Particle size distribution of samples for impeller speeds (500 rpm and 600 rpm) at temperature of 50°C, Na_2CO_3 pump flow rate of 4.42 mL/min and ageing of 30min.

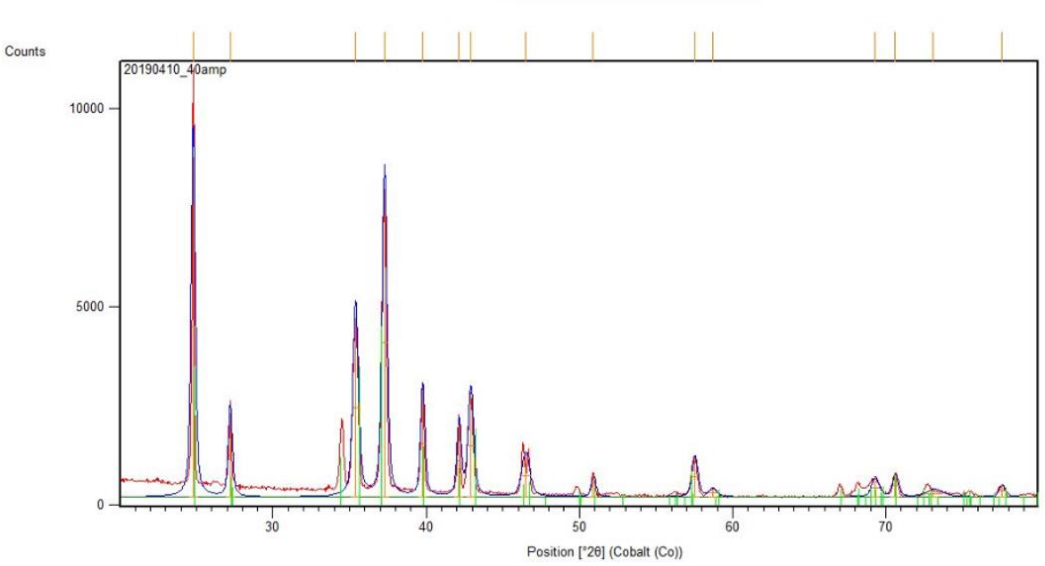

Figure 79. XRD analysis of sample obtained by homogeneous reactive crystallization (Temperature of 50^{o}C, Na_2CO_3 pump flow rate of 4.42 mL/min, ageing of 30min and impeller agitation of 500 rpm).

12.4 Impurities

The sample by heterogeneous reactive crystallization and impurities obtained after filtering the lithium sulfate solution were analyzed with (EDS), which is shown in Figure 80, Figure 81 and Figure 82.

The impurities obtained on filter paper after filtration of impure lithium sulfate solution was dried under room temperature and analyzed by the EDS technique. It can be seen that amount of oxygen, sulfur, carbon, aluminum and iron were present on the surface, which is shown in Figure 81. The impurities attached with the magnetic stirrer were also analyzed. It can be seen that amount of oxygen, iron, sulfur, chromium and some traces of aluminum were seen, which is shown in Figure 80.

From Figure 82, it can be seen that slight amount of sodium, chromium and aluminum were present on the surface of crystals.

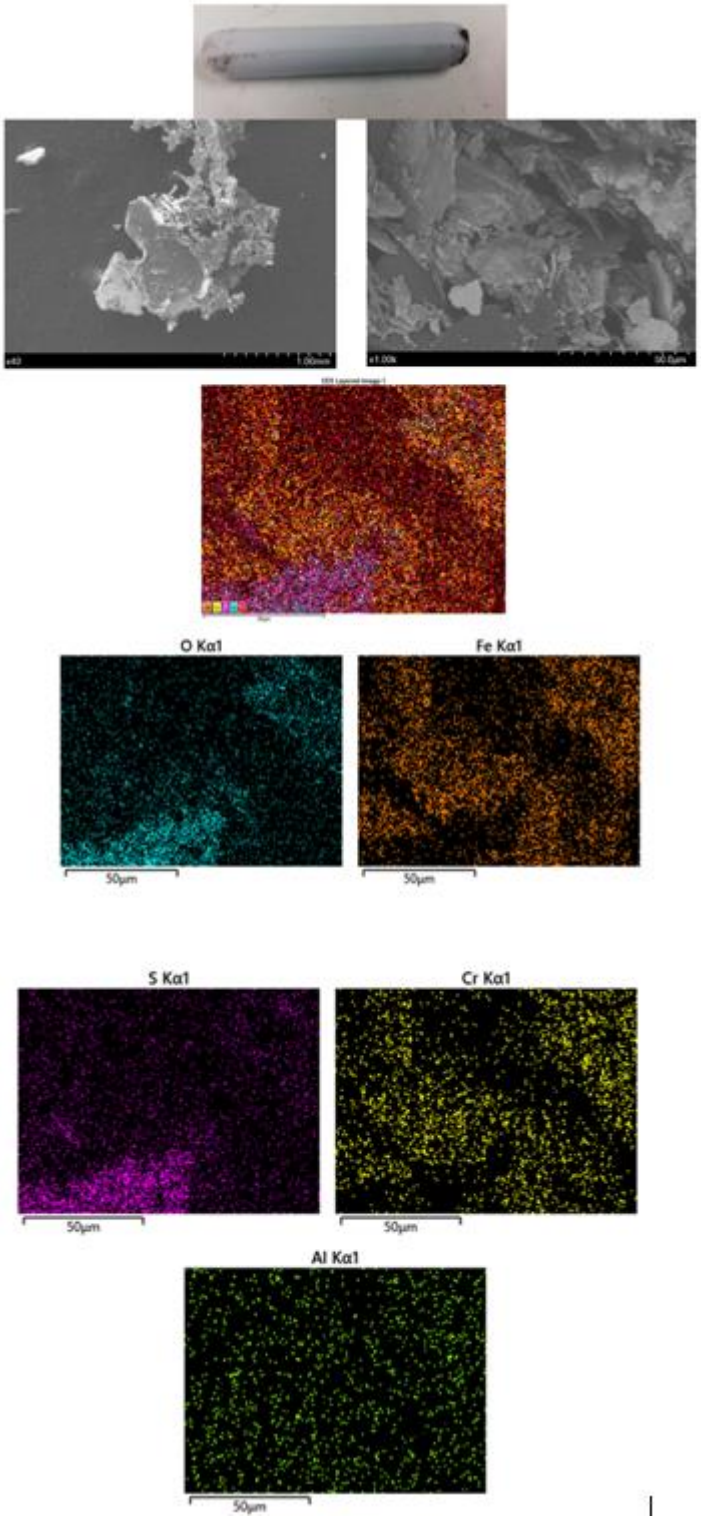

Figure 80. Analyzes through EDS technique of impurities obtained on the magnetic stirrer.

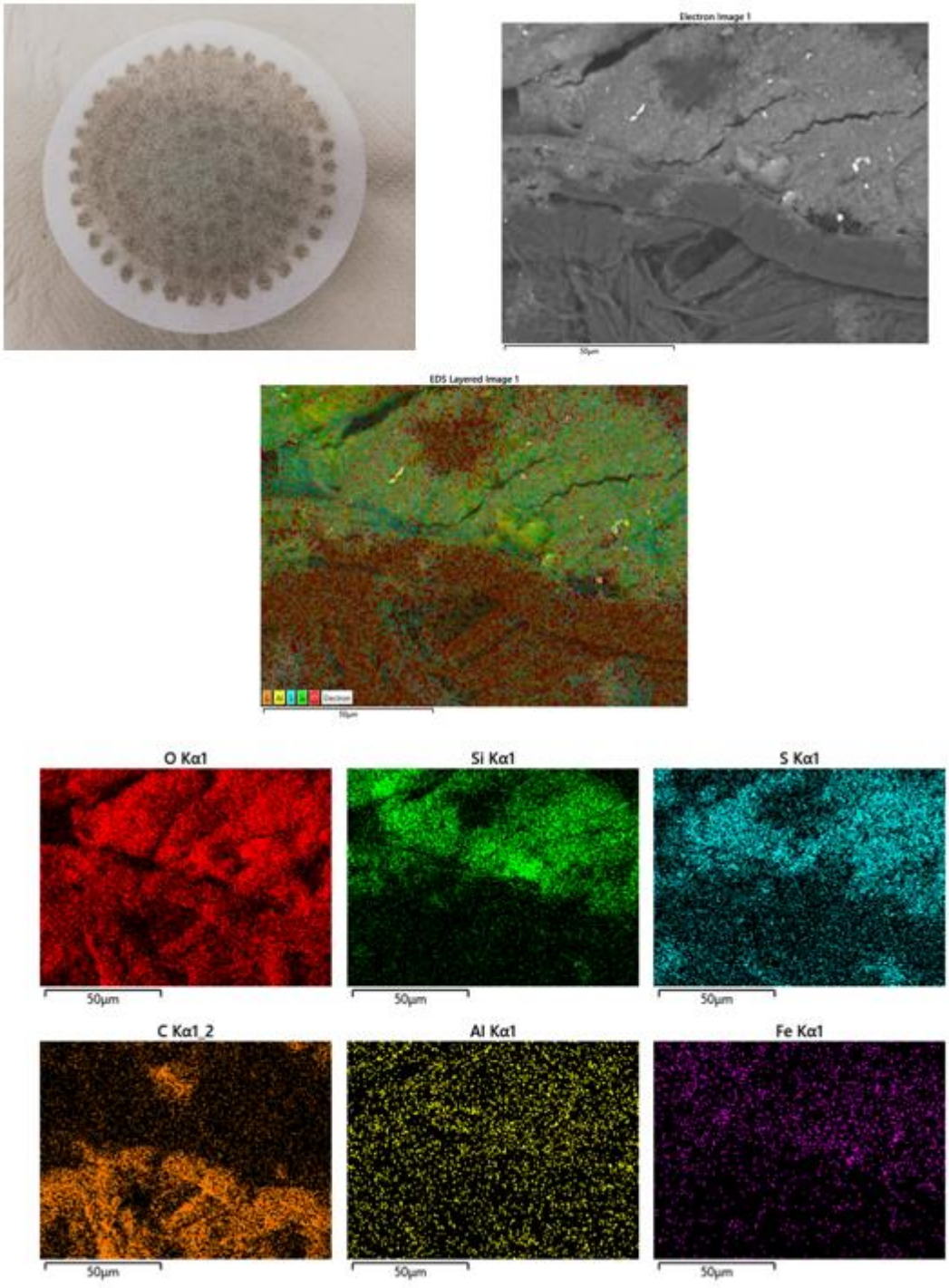

Figure 81. Analyzes by EDS technique of impurities obtained by filter paper from the lithium sulfate solution.

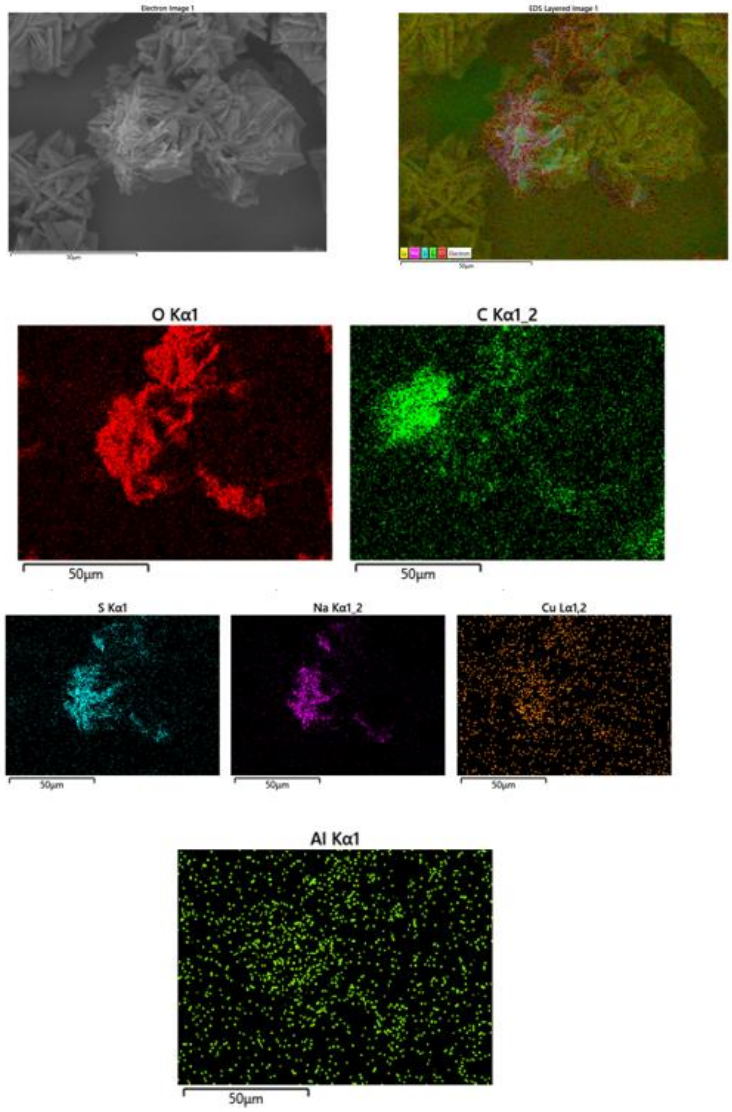

Figure 82. EDS analyzes of the sample obtained from heterogeneous reactive crystallization at 25°C temperature, 0.3 L/min gas flow rate, 600 rpm impeller stirring rate and 30 min ageing.

12.5 A comparison of heterogeneous and homogenous reactive crystallization of lithium carbonate

The homogeneous reactive crystallization of lithium carbonate conducted at 5.56 mL/min sodium carbonate pumping rate, impeller stirring rate of 500 rpm, and heterogeneous reactive crystallization was conducted at 0.5 L/min gas flow rate and, impeller speed of 600 rpm at 50°C. The residence time of both the experiments was between 16 to 18 minutes. That is why they were chosen to compare precipitation kinetics, specific cake resistance, compressibility, crystal shape purity,

and product yield. The concentration of lithium in the lithium sulfate solution was 20g/L which was same for both of the system. pH was adjusted to 9.35 with the 5M NaOH in heterogeneous system because pH needs to be high enough for carbonation precipitation. For homogeneous system there was no need of NaOH. pH curves can be seen in Figure 84 and Figure 86 for both processes.

From Table 18, it can be seen that the crystal yield is almost same for homogeneous and heterogeneous precipitation processes.

Figure 83 and Figure 85 reveal that the nucleation starts more quickly in homogeneous reactive crystallization as compared to heterogeneous reactive crystallization. This is because a saturated solution of Na_2CO_3 can provide a high amount of carbonate ions. Thus the process is faster than the heterogeneous reaction that including gas-liquid mass transfer step.

The XRD patterns is shown in Figure 93. Particle size distribution of final product shown is in Figure 90. SEM analysis revealed that crystals obtained from both experiments were flower shaped crystals, which is shown in Figure 87.

Table 18. Product yield of precipitated lithium carbonate obtained from homogeneous and heterogeneous reactive crystallization with different parameters at 50°C.

System	Impeller speed, rpm	Pump flow rate, mL/min	Gas Flow Rate, L/min	Residence time, min	pH initial	pH final	Product Yield %
Heterogeneous	500	5.56	-	18	9.01	9.71	74
Homogeneous	600	-	0.5	16	9.35	8.01	73

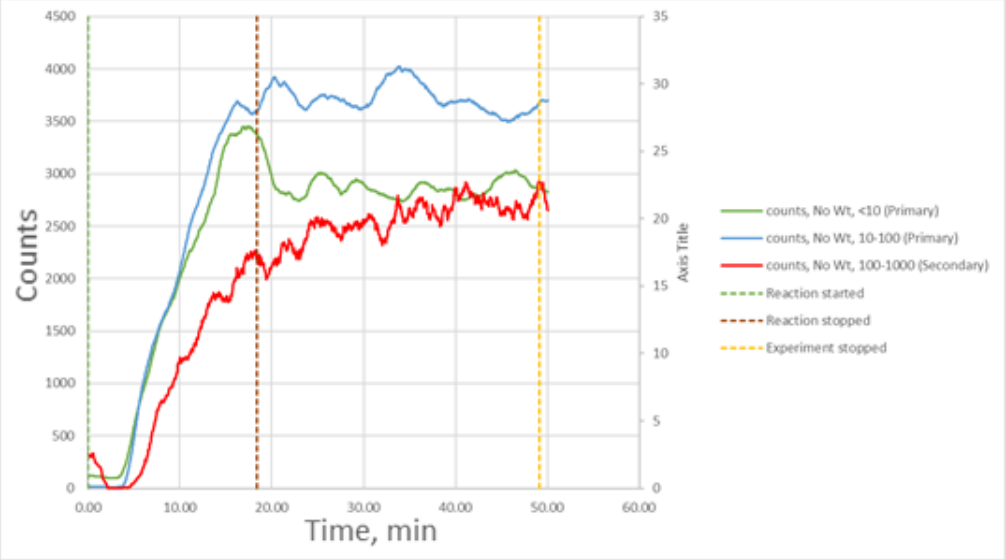

Figure 83. particles count rate obtained by homogeneous reactive crystallization of lithium carbonate at temperature of 50°C, stirring rate of 500 rpm, Na_2CO_3 pump flow rate of 5.65 (18.4 min residence time), 30min ageing. The experiment was stopped at pH 8.

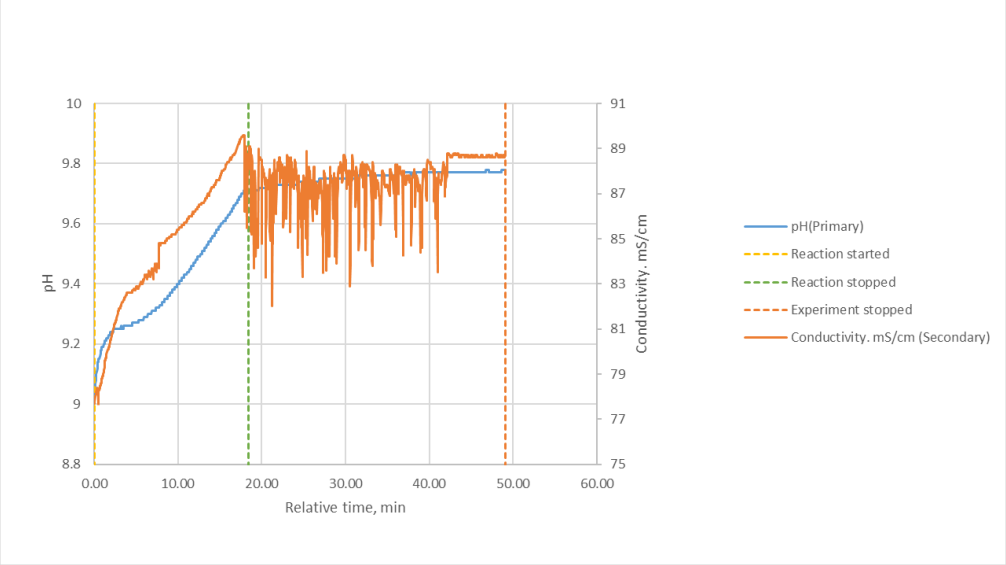

Figure 84. pH and conductivity curves obtained from homogeneous reactive crystallization of lithium carbonate at temperature of 50°C, impeller speed of 500 rpm), Na_2CO_3 pump flow rate of 5.65 mL/min (residence time of 18.4 min and ageing of 30 min.

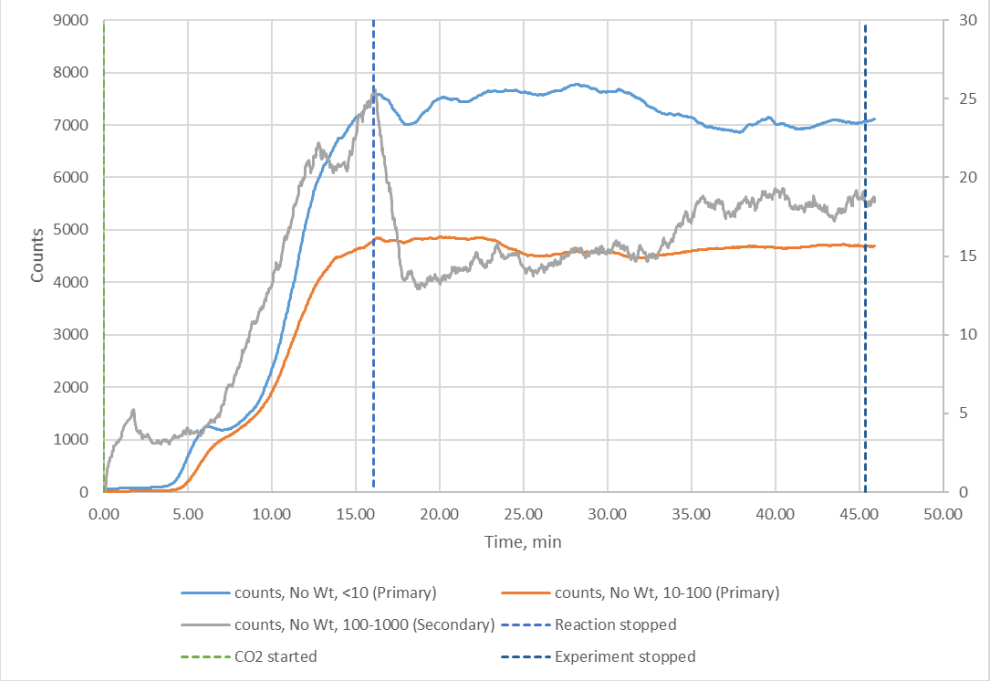

Figure 85. particles count rate obtained by heterogeneous reactive crystallization of lithium carbonate at temperature of 50ºC, stirring rate of 600 rpm, gas flow rate of 0.5 L/min (16.1 min residence time) and ageing of 30 min. The experiment was stopped at pH 8.

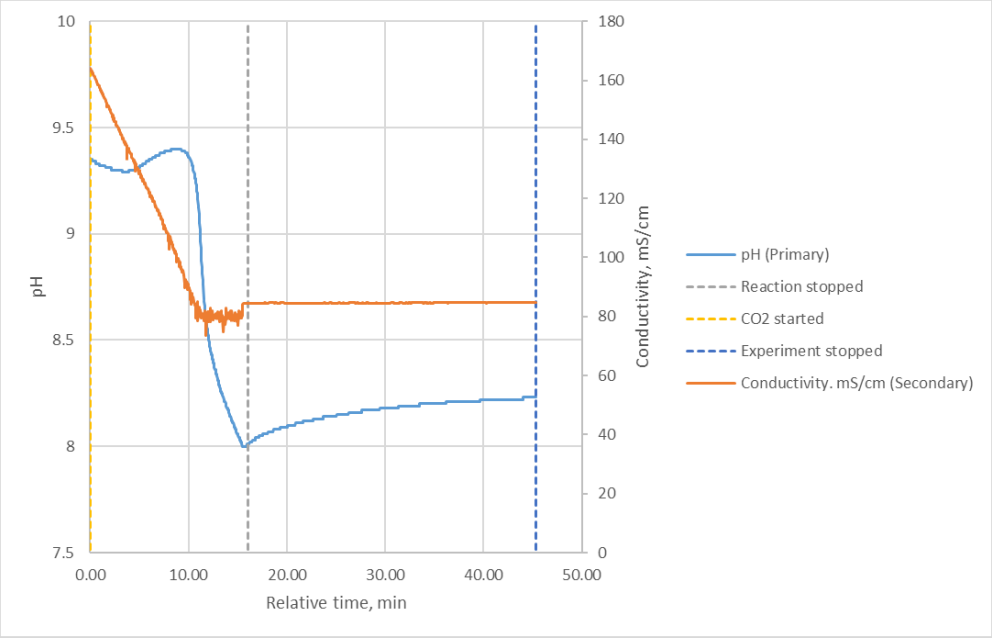

Figure 86. pH and conductivity curves obtained from heterogeneous reactive crystallization of lithium carbonate at temperature of 50ºC, impeller speed of 600 rpm, gas flow rate of 0.5 L/min (residence time of 16.1 min) and ageing of 30 min.

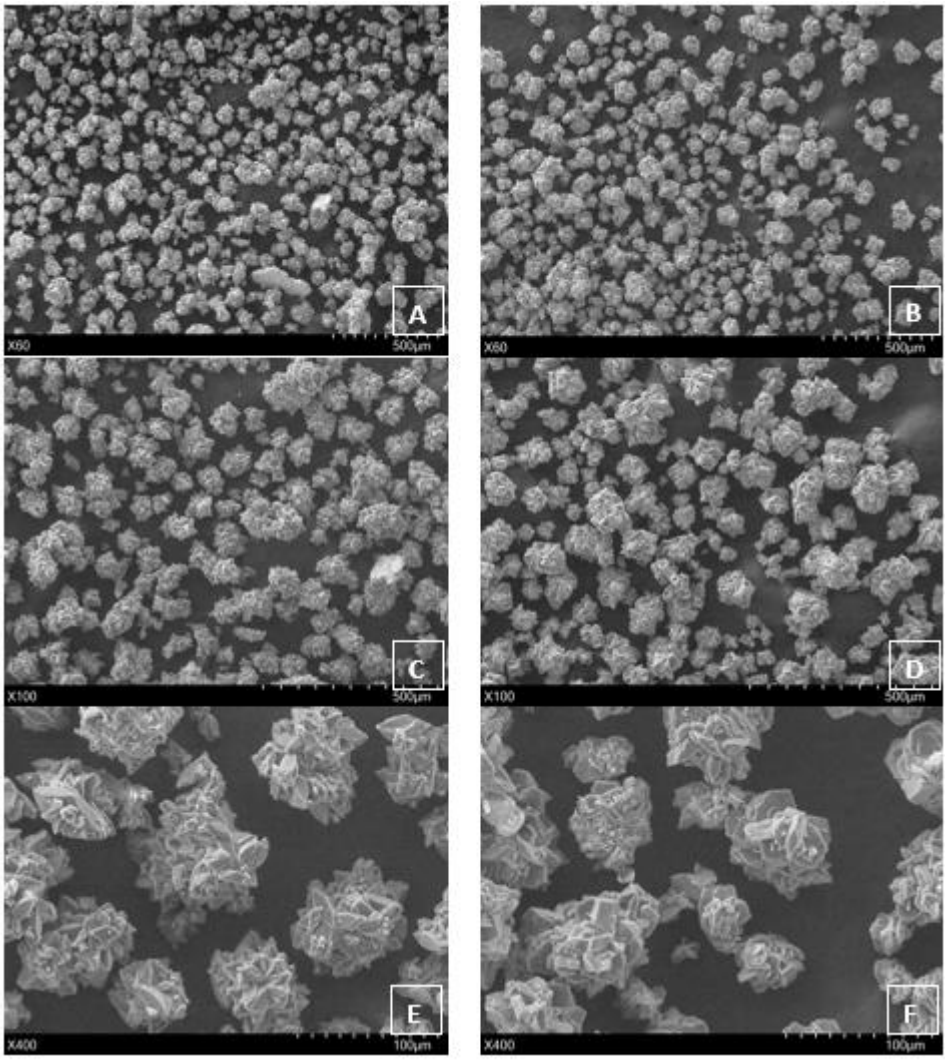

Figure 87. SEM images of samples obtained from heterogeneous reactive crystallization at temperature of 50°C, impeller speed of 600 rpm, gas flow rate of 0.5 L/min (residence time of 18.4min) and ageing of 30 min (A, C and E) and SEM images of samples obtained from homogeneous reactive crystallization at temperature of 50°C, impeller speed of 500 rpm, Na_2CO_3 pump flow rate of 5.56 mL/min (residence time of 18 min) and ageing of 30 min (B, D and F).

12.5.1 Filterability and compressibility

The filtration characteristics of solid liquid suspension obtained through heterogeneous and homogeneous reactive crystallization was described by means of filter cake resistance and compressibility. Specific cake resistance of the suspension obtained through heterogeneous and homogeneous reactive crystallization are shown in Table 19 and Table 20, respectively. The most important factors influencing the filtration characteristics are particle size, particle

shape and viscosity of the suspension. By increasing the pressure, the filtration rate observed was increased sequentially.

Collected filtration data for suspension obtained by heterogeneous and homogeneous reactive crystallization is presented in Figure 88 and Figure 89, respectively. The figures presents the cumulative filtrate curves with three different pressure. Particle shape is shown in Figure 87 and particle size distribution of the lithium carbonate crystals used in the filtration is shown in Figure 90.

In Figure 88 and Figure 89, mass of filtrate over time was not smooth. This could be because the cracks produced in the filter cake during the filtration under vacuum pressure.

Comparison between the compressibility from different suspension and average specific cake resistances reveals that the difference may due to the difference of solution viscosity. More solids were obtained in homogeneous reactive crystallization from same lithium sulfate solution which results in difference in viscosity of the mother liquor with the comparison of the solution obtained from heterogeneous reactive crystallization.

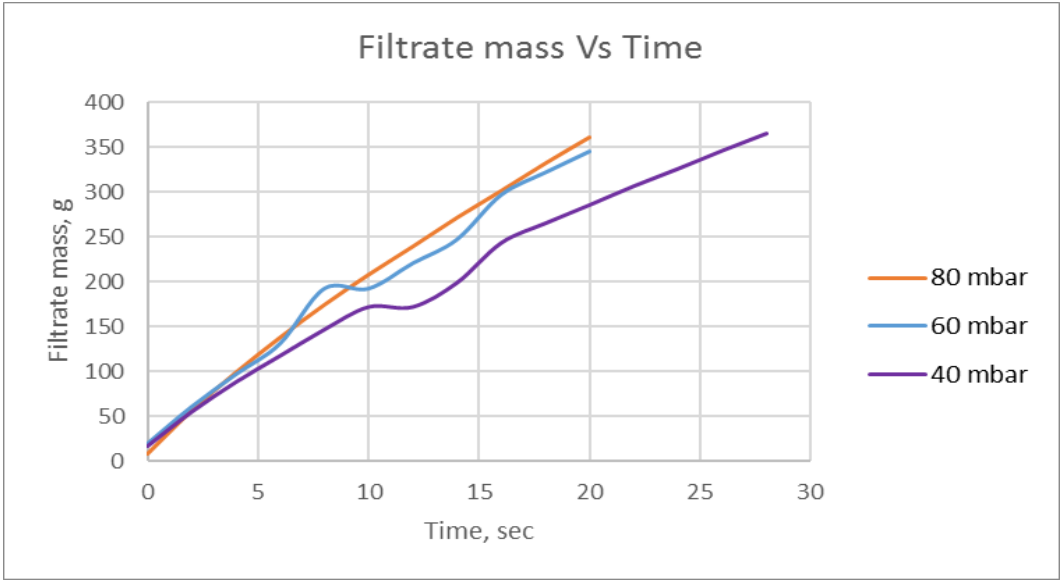

Figure 88. Filtrate mass as a function of time during filtration for the sample obtained from heterogeneous reactive crystallization at stirring rate of 600 rpm, gas flow rate of 0.5 L/min (residence time of 18.4 min) and ageing of 30 min.

Table 19. Specific cake resistance at 80, 60 and 40 mbar pressure of sample obtained by precipitation in heterogeneous system at stirring rate of 600 rpm, gas flow rate of 0.5 L/min (residence time of 18.4 min) and ageing of 30 min.

filtration vacuum (mbar)	Specific cake resistant (alpha), m/kg
80	79477
60	93390
40	115624

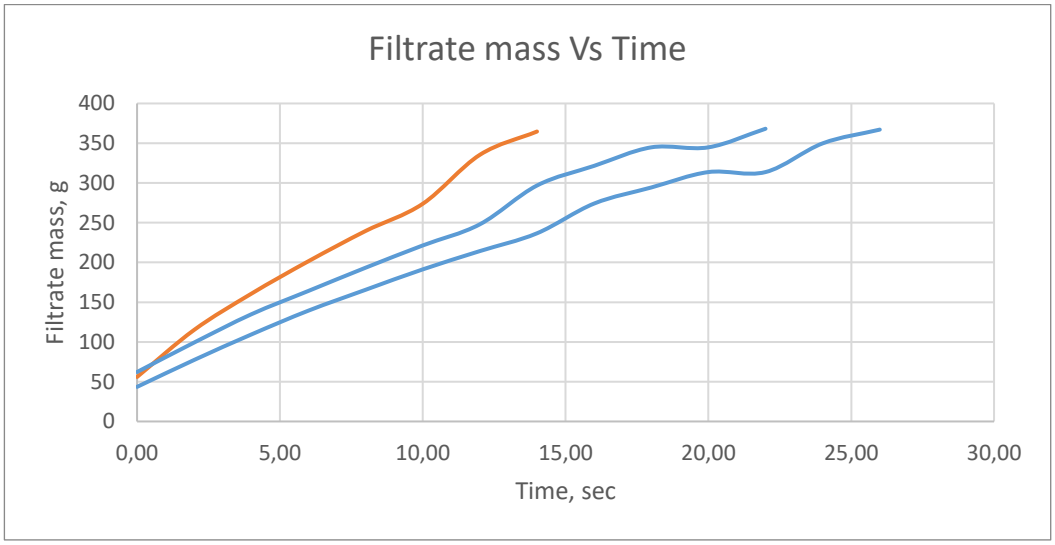

Figure 89. Filtrate mass as a function of time during filtration for the sample obtained from homogeneous reactive crystallization at stirring rate of 500 rpm, Na_2CO_3 pump flow rate of 5.56 mL/min (residence time of 18 min) and ageing of 30 min.

Table 20. Specific cake resistance at 80, 60 and 40 mbar pressure of sample obtained by homogeneous reactive crystallization at stirring rate of 500 rpm, Na_2CO_3 pump rate of 5.56 mL/min (residence time of 18 min) and ageing of 30 min.

filtration vacuum (mbar)	Specific cake resistant (alpha), m/kg
80	82574
60	115990
40	136176

Table 21. Compressibility of the product obtained by homogeneous and heterogeneous reactive crystallization.

Precipitation system	Residence time, min	Compressibility
Heterogeneous	18.4	0.113
Homogeneous	18	0.082

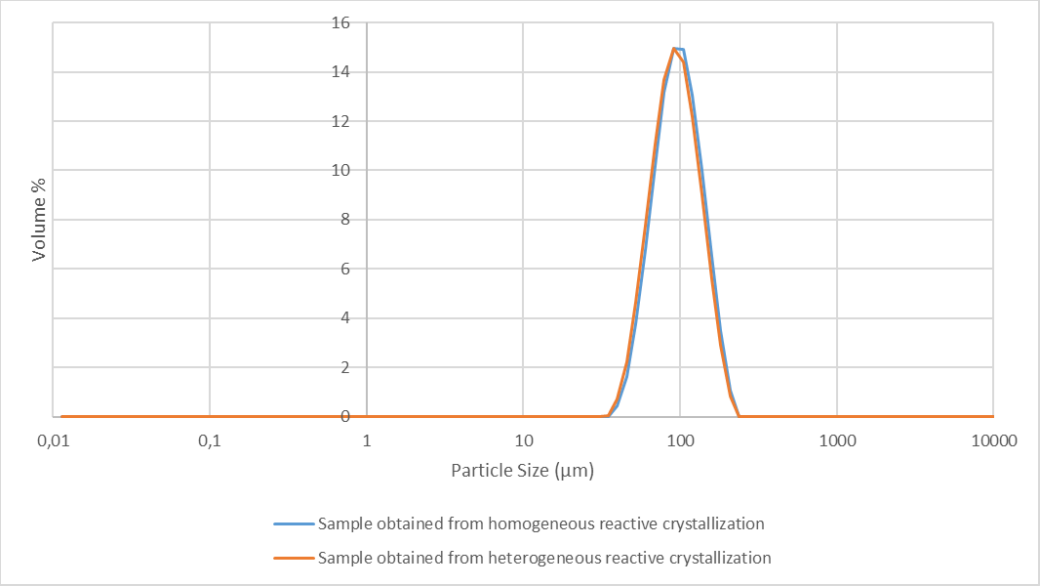

Figure 90. Particle size distribution of sample obtained by heterogeneous reactive crystallization at temperature of 50oC, impeller speed of 600 rpm, gas flow rate of 0.5 L/min (residence time of 18.4 min) and ageing of 30 min and Particle size distribution of sample obtained by homogeneous reactive crystallization at impeller speed of 500 rpm, Na_2CO_3 pump rate of 5.56 mL/min (residence time of 18 min) and ageing of 30 min.

Match software was used for XRD analysis report for each crystal sample. All the peaks were visually examined and compared with the reference data to determine the final composition of the crystal phase. Both the samples correlate with reference data (ICSD 98-010-0324), which indicates that Li_2CO_3 mainly crystallizes from the solutions.

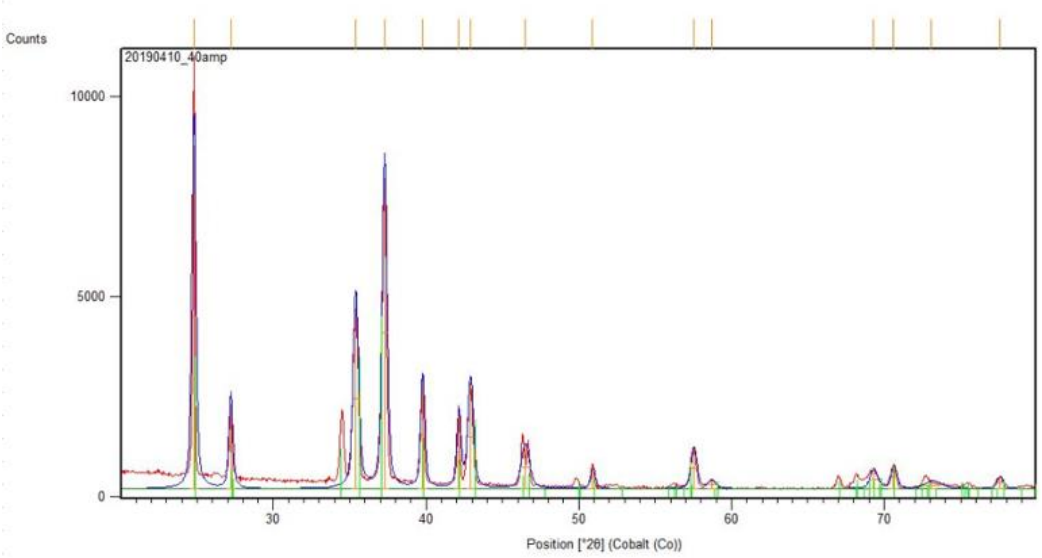

Figure 91. XRD analysis of the sample obtained by homogeneous reactive crystallization at temperature of 50°C, impeller speed of 500 rpm, Na_2CO_3 pump flow rate 4.42mL/min (Residence time of 23.7 min) and ageing of 30 min.

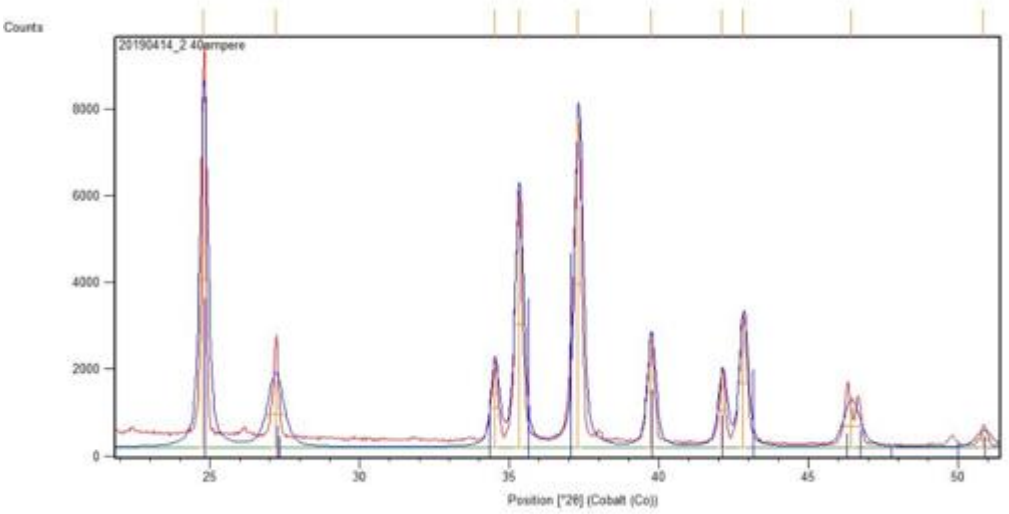

Figure 92. XRD analysis of the sample obtained by heterogeneous reactive crystallization at temperature of 50°C, impeller speed of 600 rpm, gas flow rate of 0.5 L/min and ageing of 30 min.

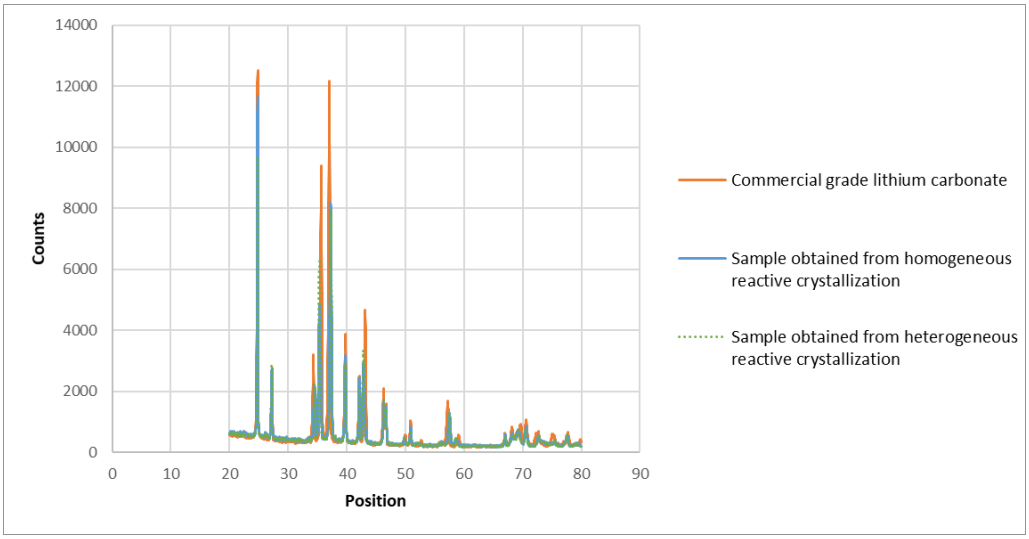

Figure 93. XRD analysis of sample Li_2CO_3 commercial grade and sample obtained from homogeneous reactive crystallization at temperature 50°C, impeller speed of 600 rpm, gas flow rate of 0.5 L/min (Residence time of 18.4 min) and ageing of 30 min and sample obtained by homogeneous reactive crystallization at temperature of 50°C, impeller speed of 500 rpm, Na_2CO_3 pump rate of 4.42 mL/min.

Conclusion

In this work, Pitzer thermodynamic model was studied to predict the Li_2CO_3 solubility in the Li_2CO_3-Li_2SO_4-H_2O ternary system. It can be concluded that the predicted activity coefficient of lithium carbonate was not consistent with literature data, which may be because the Pitzer parameters are lacking from the literature.

The aim of this study was to use carbon dioxide as a reactant for carbonation process which can help in decreasing the greenhouse gas emission and produce high quality lithium carbonate. The effects of temperature, gas flow rate, stirring rate and ageing on carbonation rate and particle size distribution was investigated. The Match program was used to obtain XRD analysis report for each sample, and most of the characteristic peaks were compared with the reference data to determine the final crystal phase composition. It can be observed from Figure 93 that peaks related to the final product in XRD analysis were identical for both product obtained by crystallization in homogeneous and heterogeneous system, which was identified as Li_2CO_3 with some impurities.

The maximum lithium carbonate yield obtained from homogeneous and heterogeneous reactive crystallization reaches approximately 74% at temperature of 50°C. The yield of lithium carbonate obtained from heterogeneous reactive

crystallization was approximately 40% at temperature of 25°C. It is concluded that carbonation process is a favorable technique for both utilization of CO_2 in strong alkaline solutions and by using saturated Na_2CO_3 solution in production of lithium carbonate.

There is not any big difference of particle size and shape for both studied temperature. Time to achieve equilibrium was less at temperature of 50°C compared to 25°C. It was noticed that the initial pH of solution in heterogeneous reactive crystallization was important for the absorption of CO_2 to get maximum yield of lithium carbonate. It should be noticed that pH was sensitive to temperature.

The results from heterogeneous reactive crystallization show that, more crystals was obtained at lower gas flow rate. Time to achieve the desired pH increases as the decrease of gas flow rate. There is not any significant difference of particle size distribution at different gas flow rates (0.3 and 0.5 L/min) for both the impeller speeds (500 and 600 rpm). Reduction in particle size of the crystals was seen at higher stirring speed. It was noted that ageing does not have significant effect in the process.

The crystallization of lithium carbonate was carried out with Na_2CO_3 pump flow rates of 2.54, 4.42 and 5.65 with residence time of 40, 23, and 18 minutes, respectively and impeller speed of 500 and 600 rpm. The results obtained from homogeneous reactive crystallization conclude that increase in pump flow rate results in acceleration of the reaction, and thus more crystals was produced. XRD analysis and SEM images showed that the precipitated lithium carbonate were flower shape crystals and the size were between 50-100 µm.

The last chapter of this thesis is to investigate and compare the particle shape, particle size distribution, purity of solids, filterability and compressibility of the crystals obtained by heterogeneous and homogeneous system. It is observed that the crystals obtained from both the cases have same particle shape and particle size distribution. It is noted that vacuum filtration is a promising technique in spatting all the crystal samples from the mother liquor. As the pressure is increased, the filtration rate increases. It is observed that the filtration characteristics is different

for different suspensions. Compressibility is affected by the shape of particles, particle size distribution and viscosity of the filtrate. It is observed from the particle size distribution that the crystals obtained from homogenous and heterogeneous reactive crystallization was same and from SEM images that the particles have same shape but the viscosity of the filtrate obtained in both cases differs because of more crystals obtained in homogeneous reactive crystallization which affected the compressibility.

Overall, the study clearly shows that using CO_2 gas in heterogeneous reactive crystallization and using Na_2CO_3 in homogeneous reactive crystallization can be used as a feasible way to recover lithium carbonate from lithium sulfate solution. Nevertheless, to crystalize the lithium carbonate of battery grade requires more research. To improve the crystal purity and to obtain battery grade lithium carbonate some suggestions are explained. First, lithium sulfate can be used with less impurities for crystallization. Second, ethanol washing is needed to remove mother liquor residue from the crystals. Finally, higher temperature than 50^{o}C can reduce the impurity. In the future, it is needed to perform more experiments to find the method to control the initial pH of the solution. These would provide some extra information which will help in understanding to control the initial pH and operating parameters for better control the crystallization process which result in crystallization of battery grade lithium carbonate with less impurities.

REFERENCES

An, J.W.; Kang, D.J.; Tran, K.T.; Kim, M.J.; Lim, T.; Tran, T. Recovery of lithium from Uyuni salar brine. Hydrometallurgy 2012, 117, 64–70. https://doi.org/10.1016/j.hydromet.2012.02.008

Bi Y, Wang T, Liu M, Du R, Yang W, Liu Z, et al. Stability of Li_2CO_3 in cathode of lithium ion battery and its influence on electrochemical performance. RSC Advances [Internet]. Royal Society of Chemistry (RSC); 2016;6(23):19233–7. https://doi.org/10.1039/c6ra00648e

Beckmann W. Seeding the Desired Polymorph: Background, Possibilities, Limitations, and Case Studies. Organic Process Research & Development [Internet]. American Chemical Society (ACS) 2000. 5, 372–83. http://dx.doi.org/10.1021/op0000778

Black S, Dang L, Liu C, Wei H. On the Measurement of Solubility. Organic Process Research & Development [Internet]. American Chemical Society (ACS); 2013 Feb 19;17(3):486–92. https://doi.org/10.1021/op300336n

Bourcier D, Féraud JP, Colson D, Mandrick K, Ode D, Brackx E, et al. Influence of particle size and shape properties on cake resistance and compressibility during pressure filtration. Chemical Engineering Science [Internet]. Elsevier BV; 2016 Apr;144:176–87. https://doi.org/10.1016/j.ces.2016.01.023

Casillas, Adrian. and Marcial, Nava. (2018). U.S. Lithium and cobalt: Same purpose, different paths." BBVA Research. accessed April 29, 2019 < https://www.bbvaresearch.com/wp-content/uploads/2018/07/180726_LithiumCobalt.pdf >

Chernov AA (1961) The spiral growth of crystals. Sov Phys Uspekhi 4:116-148

CAI Q, DAI G. Flooding Characteristics of Hydrofoil Impeller in a Two- and Three-phase Stirred Tank. Chinese Journal of Chemical Engineering [Internet]. Elsevier BV; 2010 Jan;18(3):355–61. https://doi.org/10.1016/s1004-9541(10)60231-5

Deutsche Bank (2016). Market research Lithium 101, accessed 29 April 2019 <http://www.metalstech.net/wp-content/uploads/2016/07/17052016-Lithium-research-Deutsche-Bank.compressed.pdf>

Doran PM. Mixing. Bioprocess Engineering Principles. Elsevier; 2013;201–254. https://doi.org/10.1016/b978-0-12-220851-5.00007-1

Doran PM. Mixing. Bioprocess Engineering Principles. Elsevier; 2013;255–332. https://doi.org/10.1016/b978-0-12-220851-5.00008-3

Deng T-L, Yin H-A, Tang M-L. Experimental and Predictive Phase Equilibrium of the Li+, Na+/Cl-, CO32-−H2O System at 298.15 K. Journal of Chemical & Engineering Data [Internet]. American

Chemical Society (ACS); 2002 Jan;47(1):26–9. https://doi.org/10.1021/je000368b

Dave K, Luner PE, Forness C, Baker D, Jankovsky C, Chen S. Feasibility of Focused Beam Reflectance Measurement (FBRM) for Analysis of Pharmaceutical Suspensions in Preclinical Development. AAPS PharmSciTech [Internet]. Springer Nature; 2017 Jun 21;19(1):155–65. https://doi.org/10.1208/s12249-017-0819-9

Filippov VK, Barkov DS, Fedorov YA. Applcation of the Pitzer equations to the solubility of ternary aqueous nitrate solutions at 25°C. Journal of Solution Chemistry [Internet]. Springer Nature; 1986 Jul;15(7):611–9. https://doi.org/10.1007/bf00645814

Han B, Porvali A, Lundström M, Louhi-Kultanen M. Lithium Recovery by Precipitation from Impure Solutions - Lithium Ion Battery Waste. Chemical Engineering & Technology [Internet]. Wiley; 2018 May 3;41(6):1205–10 http://dx.doi.org/10.1002/ceat.201700667

Jandova, Jitka,; Dvorak, petr,; Kondas, jan and Havlak, Lubomir. RECOVERY OF LITHIUM FROM WASTE MATERIALS. Ceramics – Silikáty 2012. 56 (1) 50-54.

Kobe, K.A., 1958. Plant Design and Economics for Chemical Engineers (Peters, Max S.) Fourth edition.

Kavanagh L, Keohane J, Garcia Cabellos G, Lloyd A, Cleary J. Global Lithium Sources—Industrial Use and Future in the Electric Vehicle Industry: A Review. Resources [Internet]. MDPI AG; 2018 Sep 17;7(3):57. https://doi.org/10.3390/resources7030057

Kelkar, V.V. & Ng, K.M. Design of reactive crystallization systems incorporating kinetics and mass-transfer effects. AIChE Journal 1999, 45(1), pp.69–81.https://doi.org/10.1002/aic.690450107

Lin, Nan-hung,; Hsieh, Yung-hsu,; Chuang, Shun-Hsing,; Wu, Chun-Hao and Huang, Yao-hui. A comparison of heterogeneous/homogeneous crystallization for phosphate recovery from biosolids. Water environment research 2018. https://doi.org/10.2175/106143017x15131012152889

Liu J, Svärd M, Rasmuson ÅC. Influence of Agitation on Primary Nucleation in Stirred Tank Crystallizers. Crystal Growth & Design [Internet]. American Chemical Society (ACS); 2015, 15(9):4177–84. https://doi.org/10.1021/cg501791q

Mohr SH, Mudd GM, Giurco D. Lithium Resources and Production: Critical Assessment and Global Projections. Minerals [Internet]. MDPI AG; 2012 Mar 19;2(1):65–84. https://doi.org/10.3390/min2010065

Meshram, P.; Pandey, B.D.; Mankhand, T.R. Extraction of lithium from primary and secondary sources by pre-treatment, leaching and separation: A comprehensive review. Hydrometallurgy 2014, 150, 192–208.https://doi.org/10.1016/j.hydromet.2014.10.012

Martin, G,; Schneider,A,; Voigt, W,; Bertau, M. Lithium extraction from the mineral zinnwaldite: Part II: Lithium carbonate recovery by direct carbonation of sintered zinnwaldite concentrate. Minerals Engineering 2017, 110, 75 to 81. https://doi.org/10.1016/j.mineng.2017.04.009

Mullin, J. W., Crystallization, Fourth edition, Reed educational and professional publishing Ltd 2001, 181-224 p.

McLeod JS, Paterson AHJ, Bronlund JE, Jones JR. The effect of agitation on the nucleation of α-lactose monohydrate. International Dairy Journal . Elsevier BV; 2016, 61:114–9.https://doi.org/10.1016/j.idairyj.2016.04.007

Myerson AS. Preface to the Second Edition. Handbook of Industrial Crystallization

Mikami T, Koseki T. Reactive Crystallization of Lithium Carbonate in the Presence of Magnesium Impurity. JOURNAL OF CHEMICAL ENGINEERING OF JAPAN [Internet]. Society of Chemical Engineers, Japan; 2017;50(4):309–14 https://doi.org/10.1252/jcej.16we150

Nguyen, Thi Hong,; Lee, Man Seung. A review on the separation of lithium ion from leach liquors of primary and secondary resources by solvent extraction with commercial extractants. Processes 2018, 6, 55. https://doi.org/10.3390/pr6050055

Nandi, Amiya Kumar,; Shirsgar, Arun sidram,; Thanigaivelan, Umapathi,; Bhattacharyya, Sibes Chandra,; Mandal, Alok kumar,; Pandey, Raj Kishore and Bhattacharya, bikash. Process Optimization for the Gas-Liquid Heterogeneous Reactive Crystallization Process Involved in the Preparation of the Insensitive High Explosive TATB. Central European journal of energetic materails 2014, 11(1), 31-57.

Ordoñez, J.; Gago, E.J.; Girardm, A. Processes and technologies for the recycling and recovery of spent lithium-ion batteries. Renew. Sustain. Energy Rev. 2016, 60, 195–205. https://doi.org/10.1016/j.rser.2015.12.363

Poe, Janita. (2018). Keliber applies for environmental permit to mine lithium in Finland, Metropolitan, Available at: https://metropolitan.fi/entry/keliber-applies-for-environmental-permit-to-mine-lithium-in-finland [Accessed 19 Oct.2018].

PAUL, E. L., ATIEMO-OBENG, V. A., & KRESTA, S. M. (2004). Handbook of industrial mixing: science and practice. Hoboken, N.J., Wiley-Interscience.

Pöllänen, K. et al., 2005. Batch cooling crystallization and pressure filtration of sulphathiazole: the influence of solvent composition. Biotechnology and Applied Biochemistry, 41(1), p.17. https://doi.org/10.1042/ba20040044

Pitzer Model Parameters, accessed June 17, 2019, <http://www.aim.env.uea.ac.uk/aim/accent4/parameters.html>

Peng C, Liu F, Wang Z, Wilson BP, Lundström M. Selective extraction of lithium (Li) and preparation of battery grade lithium carbonate (Li2CO3) from spent Li-ion batteries in nitrate system. Journal of Power Sources [Internet]. Elsevier BV; 2019 Mar;415:179–88. https://doi.org/10.1016/j.jpowsour.2019.01.072

Robert E. Brodkey and Harry C. Hershey, McGraw Hill. Transport phenomena, a unified approach, McGraw-Hill, New York (1988), P348.

Stephen H, Stephen T (1964) Solubilities of inorganic and organic com-

pounds, Vol. 2, New York, p. 668.

SHIRATO M, ARAGAKI T, ICHIMURA K, OOTSUJI N. POROSITY VARIATION IN FILTER CAKE UNDER CONSTANT-PRESSURE FILTRATION. Journal of Chemical Engineering of Japan [Internet]. Society of Chemical Engineers, Japan; 1971;4(2):172–7. https://doi.org/10.1252/jcej.4.172

Sun Y, Song X, Wang J, Yu J. Preparation of Li2CO3 by gas-liquid reactive crystallization of LiOH and CO_2. Crystal Research and Technology [Internet]. Wiley; 2012 Jan 31;47(4):437–42. https://doi.org/10.1002/crat.201100571

Sonoc A, Jeswiet J, Soo VK. Opportunities to Improve Recycling of Automotive Lithium Ion Batteries. Procedia CIRP [Internet]. Elsevier BV; 2015;29:752–7. https://doi.org/10.1016/j.procir.2015.02.039

Swain B. Recovery and recycling of lithium: A review. Separation and Purification Technology [Internet]. Elsevier BV; 2017 Jan;172:388–403. https://doi.org/10.1016/j.seppur.2016.08.031

Torotwa I, Ji C. A Study of the Mixing Performance of Different Impeller Designs in Stirred Vessels Using Computational Fluid Dynamics. Designs. MDPI AG; 2018 Mar 8;2(1):10. https://doi.org/10.3390/designs2010010

Van’t Riet K. Basic Bioreactor Design. CRC Press; 1991 Jan 7.

Widenski DJ, Abbas A, Romagnoli JA. Comparison of different solubility equations for modeling in cooling crystallization. Chemical Engineering and Processing: Process Intensification [Internet]. Elsevier BV; 2010 Dec;49(12):1284–97. https://doi.org/10.1016/j.cep.2010.09.018

Works, D.S. Extraction of lithium from the Dead Sea. Hydrometallurgy 1981, 6, 269–275.

Xu Z, Zhang H, Wang R, Gui W, Liu G, Yang Y. Systemic and Direct Production of Battery-Grade Lithium Carbonate from a Saline Lake. Industrial & Engineering Chemistry Research [Internet]. American

Chemical Society (ACS); 2014 Oct 10;53(42):16502–7. https://doi.org/10.1021/ie502749n

Yoo, M., Han, S.-J. & Wee, J.-H. Carbon dioxide capture capacity of sodium hydroxide aqueous solution. Journal of Environmental Management 2013, 114, pp.512–519.https://doi.org/10.1016/j.jenvman.2012.10.061 .

Zhang P, Yokoyama T, Itabashi O, Suzuki TM, Inoue K. Hydrometallurgical process for recovery of metal values from spent lithium-ion secondary batteries. Hydrometallurgy 1998, 47(2-3), 259–271. http://dx.doi.org/10.1016/s0304-386x(97)00050-9.

APPENDICES

Appendix I, 1.

XRD analysis of different samples obtained by heterogeneous reactive crystallization.

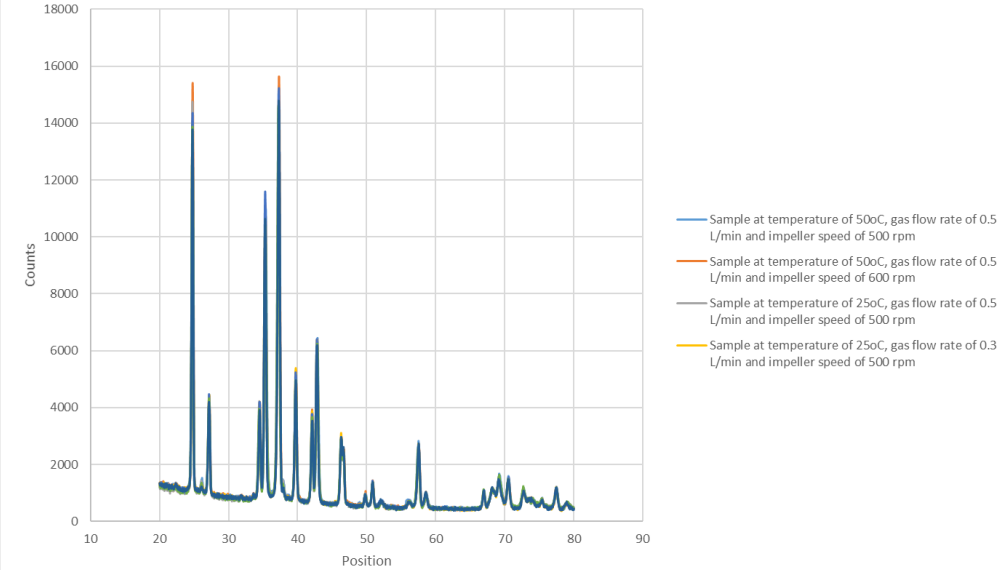

Appendix II, 1.

Chord length distribution and rate of change of counts during the solubility check of 0.8 g of lithium carbonate, 2.17 g of lithium sulfate and 97.02 g of water.

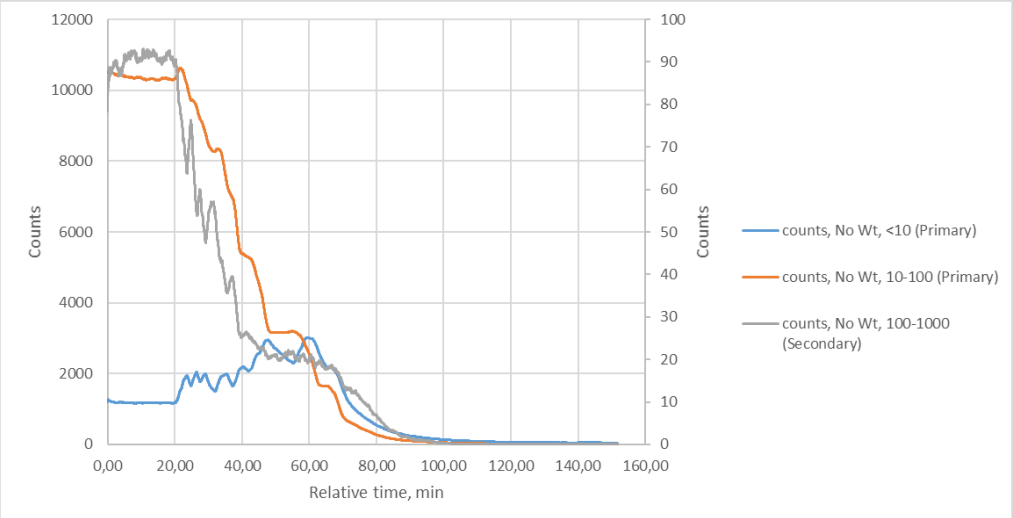

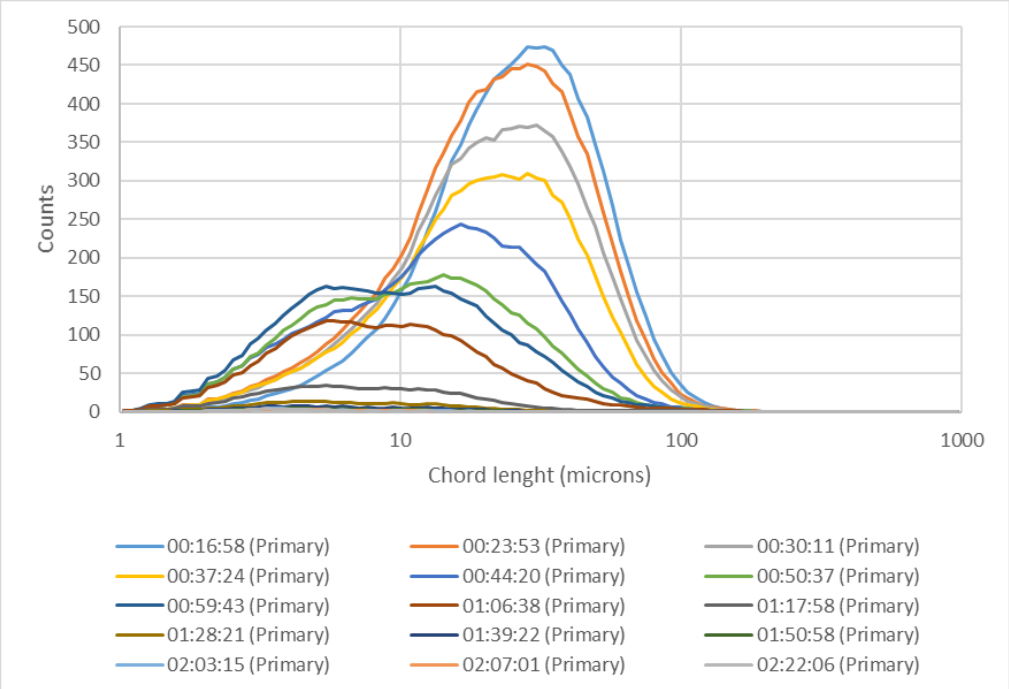

Appendix II, 2.

Chord length distribution and rate of change of counts during the solubility check of 0.4 g of lithium carbonate, 9.24 g of lithium sulfate and 90.41 g of water.

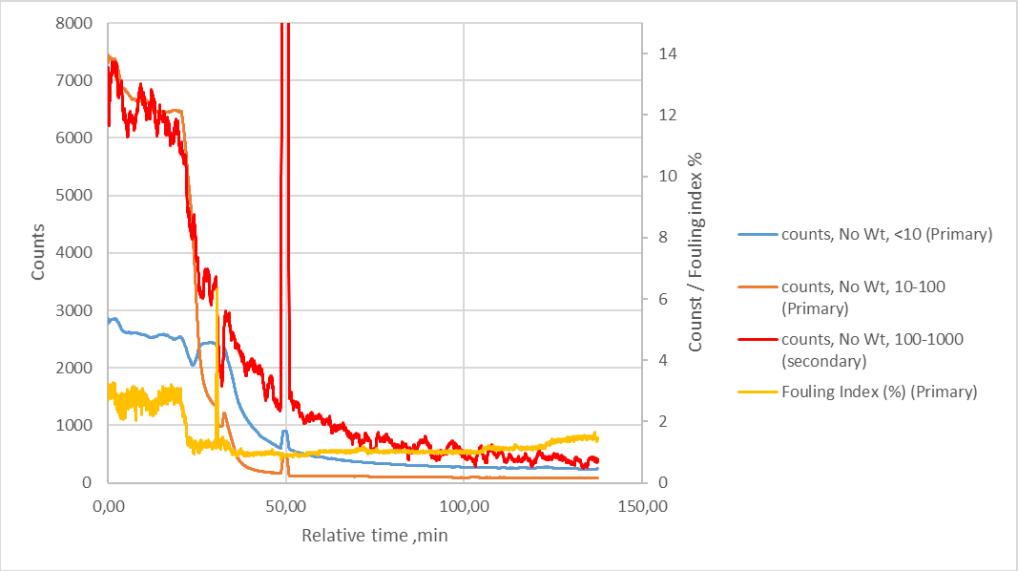

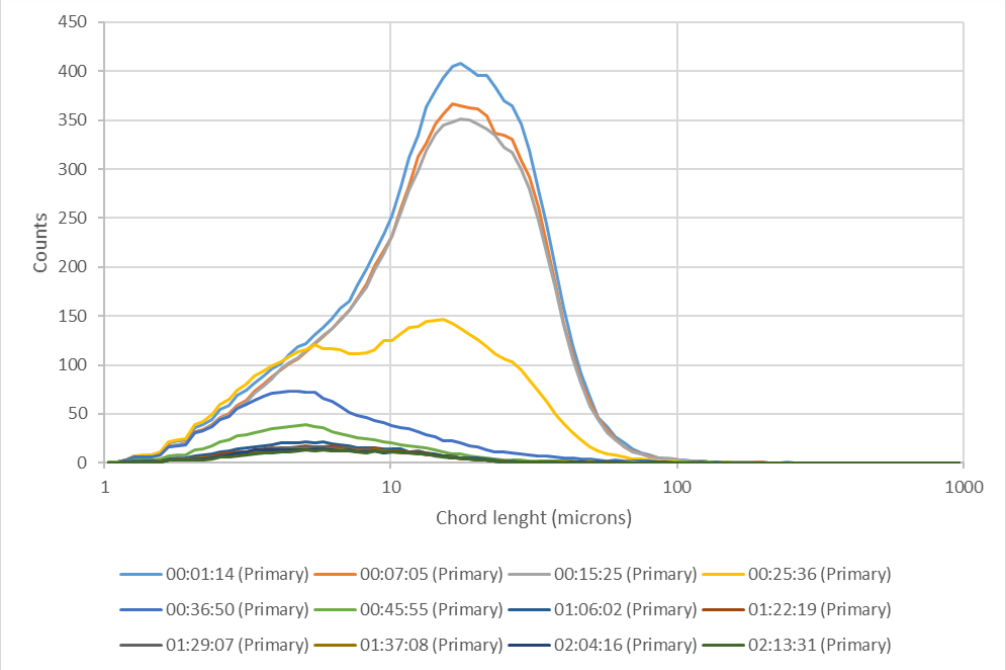

Appendix II, 3.

Chord length distribution and rate of change of counts during the solubility check of 0.2 g of lithium carbonate, 23.34 g of lithium sulfate and 76.50 g of water.